Smart neural bridge:

Algorithms to drive a brain machine interface for control of the paralyzed limb

Gareth James Richard York

Submitted in accordance with the requirements for the degree of

Doctor of Philosophy

The University of Leeds

School of Biology

April 2020

The candidate confirms that the work submitted is his/her/their own, except where work which has formed part of jointly authored publications has been included. The contribution of the candidate and the other authors to this work has been explicitly indicated below. The candidate confirms that appropriate credit has been given within the thesis where reference has been made to the work of others.

The work in Chapter 3 of the thesis has appeared in publication as follows:

"Muscles Recruited During an Isometric Knee Extension Task is Defined by Proprioceptive Feedback", 2019 *BioRxiv*, York, G., Osborne, H., Sriya, P., Astill, S., de Kamps, M. and Chakrabarty, S. I was responsible for the comparison of onset detection algorithms, comparison of synergy extraction algorithms, analysis of synergies during the isometric task. The contribution of the other authors was dataset collection, the MIIND model framework and the specific MIIND architecture.

The work in Chapter 5 of the thesis has appeared in publication as follows:

"Muscles Recruited During an Isometric Knee Extension Task is Defined by Proprioceptive Feedback", 2019 *BioRxiv*, York, G., Osborne, H., Sriya, P., Astill, S., de Kamps, M. and Chakrabarty, S. I was responsible for altering the MIIND framework to model injuries, designing and implementing the NMF reconstruction algorithm and analysis of the findings. The contribution of the other authors was the MIIND model framework and the healthy MIIND architecture.

This copy has been supplied on the understanding that it is copyright material and that no quotation from the thesis may be published without proper acknowledgement.

Assertion of moral rights:

The right of Gareth James Richard York to be identified as the author of this work has been asserted by Gareth James Richard York in accordance with the Copyright, Designs and Patents act 1988.

© 2020 The University of Leeds and Gareth James Richard York

i. Acknowledgments

I would like to thank my supervisors, Dr Samit Chakrabarty, Dr Paul Steenson and Dr Jongrae Kim for their support, guidance and wise words throughout my PhD. To Dr Chakrabarty I would like to say thank you for helping me to see the bigger picture through the mists and for always having blue-skies thinking. Thank you to Dr Steenson for engineering advice, especially building the PulsePal device, teaching me to always order 3 spares. Thank you to Dr Kim for coding advice and for always having an open door for me.

Thank you to my colleagues who have helped or collaborated with my work, including Dr Roger Kissane (electrophysiology, surgery and existential advice), Dr Piyanee Sriya (EMG recording, anatomy), Hugh Osborne (MIIND, synergy analysis and showing me what a real coder looks like), Dr Tom Richards (EMG analysis and the benefits of anarcho-syndicalism) and Dr Marc de Kamps (MIIND). This work owes a debt to all of you and it has been a pleasure working with every one of you.

Without my friends and family none of this would be possible, I would never have survived. Thank you to my mum, Sarah York, who has supported me through the worst times in my life and has made the best times possible. Thank you to Luke Souter, Stuart Dickens, Ashleigh Goodenough, Brad Balmer and Chris Bennigsen for letting me escape to a world darker than ours but filled with the best friends a Dungeon Master could ask for. Thank you to Laura Rice, Chris Partington, Dr Alice Webb and anyone else who has succeeded in the herculean task of putting up with me this long.

I would like to thank Dr Kathryn Hutchinson, my darling Katie, for loving me with all of your tubes, for being my rock and for sharing your life with me. You are my inspiration for who I want to be, and I will love you forever, even when we're ghosts.

I dedicate this work to my father Dr James York. I made my dad a promise when he died that I would become a doctor. This wasn't quite what we had in mind, but I think he'd still be proud. I love you dad and I will always strive to be the man you were.

"*It's still magic even if you know how it's done.*" *– Terry Pratchett*

ii. Abstract

Treating damage to the nervous system is limited to targeting natural recovery, with limited recourse if these mechanisms fail. The level of disruption between descending systems and motor effectors is the major factor determining recovery in SCI. Attempts have been made to reconnect descending motor signals with the correct muscles but have struggled to restore motor control to pre-injury states. This thesis has tried to address limitations in current devices by designing algorithms to control a brain machine interface at the level of the spinal cord that provides functional electrical stimulation in a closed loop manner incorporating synergy information extracted from muscle activity.

Synergy information is identified using dimensionality reduction algorithms. To determine which method was suitable for online analysis the accuracy of commonly used algorithms for synergy extraction and activity onset detection were compared. Findings from this comparison challenge assumptions regarding the utility of various methods. The most accurate algorithm, non-negative matrix factorization, was implemented online and applied to isometric knee extensions at different angles. It was shown that in contrast to the accepted view, proprioceptive feedback plays a significant role in synergy recruitment. Using an interneuron population model, the experimentally observed synergies were reproduced using only changes in afferent feedback. Using muscle synergies as a target for motor control requires a method for generating specific electromyography waveforms. An artificial neural network successfully learned the relationship between stimulation parameters and electromyography for stimulation of the rat hind limb. These algorithms were combined in a simulated injury environment using the same interneuron model described previously with connections removed or reduced. The combined algorithms were able to successfully restore muscle synergies to normal levels in some injury conditions. These algorithms represent a system that uses closed loop control of muscle synergy recruitment that could be implemented in a variety of devices.

iii. Contents

CHAPTER 1: INTRODUCTION 13

1.1 General introduction 13
1.2 Theories of motor control 14
1.2.1 The "degrees of freedom" problem 14
1.2.2 The muscle synergy hypothesis 15
1.2.3 Agonists, antagonists and synergists 17
1.3 Systems of motor control 17
1.3.1 Base components 17
1.3.2 Descending efferent signals 18
1.3.3 Central pattern generators 18
1.4 Afferent feedback 19
1.4.1 Muscle spindles 19
1.4.2 Golgi tendon organ 19
1.4.3 Nociceptors and cutaneous fibres 20
1.5 Brain machine interfaces for the purposes of motor control 20
1.6 Machine learning 22

CHAPTER 2: GENERAL METHODS 27

2.1 General Rationale 27
2.1.1 Rationale for an algorithm-based approach 28
2.2.1 Subjects and Ethical approval 28
2.2.2 Dataset size 29
2.3 Coding 30
2.4 Synergy Analysis 30
2.4.1 Data Collection 31
2.4.2 Movement Protocol 31
2.4.3 Data Pre-processing 32
2.4.4 Onset/offset-detection 32
2.4.5 Synthetic muscle synergy generation 34
2.4.6 Cosine similarity analysis 35
2.4.7 Synergy extraction algorithms 36
2.4.8 Principal component analysis 36
2.4.9 Factor analysis 37
2.4.10 Independent component analysis 38
2.4.11 Non-negative matrix factorization 39
2.4.12 Selection of rank factor 40
2.6 Neuronal Models 41
2.6.1 Population Density Techniques 41
2.6.2 MIIND 41
2.6.3 The Spinal Circuit Model 42
2.7 Machine learning models "fuzzy" non-linear relationships 46
2.7.1 Surgical Procedure 47
2.7.2 Data collection 49
2.7.3 Stimulation Protocol: 49
2.7.4 Data pre-processing and artificial neural network design 50
2.8 Closed loop control and MIIND injury modelling 52
2.8.2 Network injury models 52
2.8.3 Reconstruction of healthy synergies using an ANN 54

CHAPTER 3: ONLINE REAL TIME SYNERGY ANALYSIS – PROPRIOCEPTIVE FEEDBACK AND ISOMETRIC KNEE EXTENSION 55

3.1 ABSTRACT 55
3.2 INTRODUCTION 55
3.2.1 Current understanding of synergy recruitment does not adequately explain the role of afferent feedback 56
3.2.2 MIIND is a model of spiking neurons that efficiently models populations 57
3.2.3 Experimental rationale 58
3.3 RESULTS 59
3.3.1 A moving average window accounts for aberrant spiking activity 59
3.3.2 NMF performs best among common synergy extraction methods 65
3.3.3 Application of NMF to isometric knee extension task 71
3.3.4 NMF identifies two muscle synergies from the EMG activity 71
3.3.5 Synergy 1: Coordinated, balanced recruitment of all muscles is a canonical recruitment pattern in anisometric task 75
3.3.6 Synergy 2: The degree of muscle stretch regulates a balance between the activity of agonist and antagonist muscles 75
3.3.7 Synergy 2: At the limit of extension, afferent signals strongly affect synergy patterns in both positions 76
3.3.8 Synergy 2: Across many angles and positions, there is a stronger bias towards the bifunctional muscles 76
3.3.9 The model reproduces synergies observed experimentally 76
3.3.10 Changing afferent inputs A or B creates a bias in synergy 2 between agonist and antagonist motor neuron populations 81
3.3.11 The additional connection strength to MN-RF and MN-ST produces a bias for those two populations in synergy 2 81
3.3.12 Afferent input C provides a strong bias in synergy 2 for the antagonist muscles during maximum extension 82
3.3.13 The model does not account for variation in afferent signals from trial to trial 82
3.4 DISCUSSION 83
3.4.1 Evaluation of muscle activity analysis algorithms is data dependent 84
3.4.2 Muscle synergies extracted from isometric extension of the knee are altered in relation to internal angle of the knee 85
3.4.3 Interneuron modelling of the CPG demonstrates changes in levels of afferent feedback are sufficient to alter synergy recruitment 86
3.5 CONCLUSION 87

CHAPTER 4: CONTROL OF STIMULATION PARADIGMS USING ARTIFICIAL NEURAL NETWORKS TO GENERATE EMG WAVEFORMS IN THE RAT HIND LIMB 89

4.1 ABSTRACT 89
4.2 INTRODUCTION 90
4.2.1 Current methods of tuning stimulation parameters lack specificity and are difficult to automate 91
4.2.2 Machine learning algorithms are ideally suited to solving nonlinear problems with incomplete knowledge 91
4.2.3 Experimental rationale 92
4.3 RESULTS 95
4.3.1 Calibration for muscle length and changes across the stimulation paradigm 95
4.3.2 EMG parameters response to stimulation is a complex non-linear relationship 96

4.3.2 Network training successfully predicted EMG parameters in known and unknown conditions ... 101
4.4 DISCUSSION ... 106
4.4.1 EMG parameters demonstrate non-linearity across muscles ... 107
4.4.2 An ANN learnt a generalized transfer function for electrical stimulus in the peripheral nervous system and resultant EMG activity ... 108
4.5 CONCLUSION ... 109

CHAPTER 5: CLOSED-LOOP RECONSTRUCTION OF HEALTHY MUSCLE SYNERGIES USING A POPULATION MODEL OF CORTICAL AND PERIPHERAL INJURIES ... 110

5.1 ABSTRACT ... 110
5.2 INTRODUCTION ... 110
5.2.1 Synergy recruitment changes in set ways following injury ... 111
5.2.2 True closed loop control requires integrating analysis of motor output with the provided stimulation ... 112
5.3 RESULTS ... 113
5.3.1 The injury model recreates changes to synergy recruitment in the same way as observed in humans ... 113
5.3.2 An ANN trained in the rat peripheral nervous system was able to learn a transfer function for an in silico model of a complex interneuron network ... 118
5.3.3 NMF reconstruction of healthy synergy recruitment was successful in a subset of injury types ... 118
5.4 DISCUSSION ... 121
5.4.1 The MIIND neuronal model can accurately simulate the effects of nervous system injury ... 121
5.4.2 The ANN learns a general transfer function that is transferable from animal data to human data ... 122
5.4.3 Closed loop BMI control can restore healthy muscle synergies in some injury states ... 122
5.4.4 Model limitations ... 123
5.5 CONCLUSION ... 123

CHAPTER 6: DISCUSSION ... 125

6.1 SUMMARY OF KEY FINDINGS ... 125
6.2 DISCUSSION OF KEY FINDINGS ... 126
6.2.1 Methodological assumptions affecting muscle synergy extraction ... 126
6.2.2 Proprioceptive feedback into the recruiting interneuron network is vital for healthy synergy output ... 127
6.2.3 ANNs are capable of learning generalized transfer functions in the nervous system ... 128
6.2.4 The MIIND network is capable of modelling damage to the nervous system ... 129
6.2.5 Restoration of healthy muscle synergies by an in silico BMI ... 129
6.3 UTILITY TO THE FIELD ... 130
6.3.1 Synergy detection algorithms, comparison and online implementation ... 130
6.3.2 Algorithms for automated stimulus control ... 130
6.3.3 Simulation of neural networks ... 130
6.4 CLINICAL SIGNIFICANCE ... 131
6.4.1 Muscle synergies analysis for assessing physiotherapy in the elderly ... 131
6.4.2 BMI for treatment of foot drop ... 131
6.5 FUTURE DIRECTIONS ... 132
6.5.1 ICA-PCA and autoencoders for synergy extraction ... 132
6.5.2 Expanded stimulus/response experiments at greater degrees of separation ... 133
6.5.3 Isolating the role of afferent feedback for synergy recruitment in dynamic tasks ... 134
6.5.4 Locomotion synergies and the CPG within the MIIND framework ... 134

6.6 CONCLUDING REMARKS 135
APPENDICES 137

REFERENCES 145

List of Tables

Table	Title	Page Number
	Chapter 2	
2-A	**Parameters relevant to each connection between populations and from inputs in the model**	**45**
2-B	**Summary of results measured per animal**	**51**
	Chapter 3	
3-A	**Synergy rows and columns (as defined in Section 2.4.10) were compared across all pairs of participants using cosine similarity analysis following synergy extraction using NMF**	**74**

List of Figures

Figure	Title	Page Number
	Chapter 1	
1-A	Concepts in machine learning	25
	Chapter 2	
2-A	Schematic of connections between simulated spinal populations	44
2-B	Surgical preparation for stimulation of the sciatic and tibial nerves.	48
2-C	Removed or reduced connections between simulated interneuron populations to recreate different injuries to the nervous system	53
	Chapter 3	
3-A	Comparison of accuracy and calculation speed of three algorithms for detection of onset of muscle activity	61
3-B	Accuracy comparison between three algorithms for detection of onset of muscle activity with increasing levels of aberrant spiking	62
3-C	Accuracy comparison between three algorithms for detection of onset of muscle activity with aberrant spiking activity and increasing levels of noise	63
3-D	Effect of standard filtering methods on accuracy comparison between three algorithms for detection of onset of muscle activity with aberrant spiking activity and increasing levels of noise	64
3-E	Example of simulated synergy coefficients and vectors and resulting synthetic muscle activity	67
3-F	Accuracy of four commonly used muscle synergy extraction methods on a representative example of synthetic synergies	68
3-G	Average cosine similarity between synthetic synergies and synergies extracted by four commonly used muscle synergy extraction methods	69

3-H	**Effect of three different onset detection algorithms on synergy detection accuracy of four commonly used muscle synergy extraction methods**	**70**
3-I	**Average variance accounted for (VAF) scree plot for rank one to four NMF dimensionality reduction across all angles and both positions of the isometric knee extension task**	**73**
3-J	**Muscle synergies extracted using rank two NMF from an isometric knee extension task at four internal angles of the knee (0°, 20°, 60°, and 90°).**	**77**
3-K	**Muscle synergy features extracted using rank 2 NMF applied to the average firing rates of five motorneuron populations for different levels of input from Afferent Input A (1)**	**79**
3-L	**Comparison of simulation results to experimental findings following synergy extraction**	**80**
	Chapter 4	
4-A	**Representative examples of sub threshold, threshold and supra-threshold signals**	**97**
4-B	**Change in response to test pulses for each muscle across the stimulation paradigm**	**98**
4-C	**Calibration curve for changes in output due to muscle length**	**99**
4-D	**Mean values for the four values used for artificial neural network training**	**100**
4-E	**Artificial neural network performance across training epochs on a complete dataset**	**102**
4-F	**Artificial neural network performance across training epochs on an incomplete dataset**	**103**
4-G	**Network prediction of pulse parameters on training dataset (n=8, variable contribution for each muscle)**	**104**
4-H	**Network prediction of pulse parameters on unseen dataset of one animal (training n=7, variable contribution for each muscle, prediction n=1)**	**105**

	Chapter 5	
5-A	**Muscle synergies extracted from MIIND network modelling different injuries affecting extensor interneurons**	**115**
5-B	**Muscle synergies extracted from MIIND network modelling different injuries affecting flexor interneurons**	**116**
5-C	**Muscle synergies extracted from MIIND network with modelling a bilateral injury.**	**117**
5-D	**Synergy extraction following NMF reconstruction of healthy synergies in a model of unilateral injury to control of extensor muscles**	**119**
5-E	**Synergy extraction following NMF reconstruction of healthy synergies in a model of a bilateral injury affecting extensor interneurons**	**120**
	Appendices	
1-A	**Experimental setup**	**137**
1-B	**Pair wise comparisons following two-way ANOVA for mean cosine similarity values for synergy activation coefficients between synthetic synergies and extracted synergies for different synergy extraction algorithms and onset detection algorithms**	**139**
1-C	**Pair wise comparisons following two-way ANOVA for mean cosine similarity values for synergy vectors between synthetic synergies and extracted synergies for different synergy extraction algorithms and onset detection algorithms**	**141**
1-D	**Examples of recorded EMG signals from 4 muscles of the rat hindlimb and ergometer recording attached to tendon at endpoint of limb during test-pulse stimulation**	**142**
1-E	**Subthreshold, threshold and supra-threshold stimulation of the rat peripheral nerve at two sites**	**143**
1-F	**Comparison of stimulus at threshold value for different stimulating cuffs**	**144**

List of Abbreviations

ANN	Artificial neural network
ANOVA	Analysis of variance
BF	Biceps femoris
BMI	Brain machine interface
CNS	Central nervous system
CPG	Central pattern generator
DOF	Degrees of freedom
EDL	Extensor digitorum longus
EEG	Electroencephalogram
EHP	Extensor hallucis proprius
EIF	Exponential integrate-and-fire
EMG	Electromyography
FA	Factor analysis
FES	Functional electrical stimulation
ICA	Independent component analysis
LFP	Local field potential
LG	Lateral gastrocnemius
MG	Medial gastrocnemius
MIIND	Multiple instantiations of interacting neural dynamics
NMF	Non-negative matrix factorization
PCA	Principal component analysis
PDF	Probability density function
PDT	Population density techniques
ReLu	Rectified linear units
RF	Rectus femoris
RMS	Root mean square
SampEn	Sample entropy
SNR	Signal to noise ratio
ST	Semitendinosus
TA	Tibialis anterior
VAF	Variance accounted for
VL	Vastus lateralis
VM	Vastus medialis

Chapter 1: Introduction

1.1 General introduction

Traumatic injury resulting in partial or total loss of axons of descending spinal neurons causes varying degrees of paralysis due to loss of communication between descending motor control pathways and motor neurons (Nas et al., 2015). A brain machine interface (BMI) is a device that uses measured neural activity to interact with another device (Vidal, 1973; Jackson and Fetz, 2011). One possible output device is an electrical stimulator placed within or near the spinal cord (Zimmermann et al., 2011; Nishimura et al., 2013; Grahn et al., 2014; Shanechi et al., 2014; Capogrosso et al., 2016). In theory a BMI could bypass the injury site and link caudal neural activity with rostral motor neuron effectors, restoring a level of control to the paralyzed area (Alam et al., 2016). The potential for curative treatment for spinal cord injury has driven the development of a diverse array of devices. These devices use different measures of neural activity and interpret this activity in different ways. Most implementations then pair this activity with functional electrical stimulation (FES) delivered at the level of the spinal cord, peripheral nerve or directly to muscle fibres. These methods have succeeded in controlling simple movements such as wrist flexion or primitive locomotion in animal models (Nishimura et al., 2013; Bouton et al., 2016).

The initial potential of these devices is held back by limitations such as increased muscle fatigue, difficulty adapting to new environments or new subjects and most devices require extensive training periods (Thomas et al., 2003; Krauledat et al., 2008; Kindermans et al., 2014). These limitations are indicative of the inability to effectively recruit spared neural circuits. For instance FES results in reversal of the normal recruitment of motor neurons, recruiting the largest most fatigable neurons first (Blair and Erlanger, 1933; Laforet et al., 2009). This, among other factors, accounts for the increased fatigability observed in paralyzed muscles (Jones et al., 1979; Rabischong and Ohanna, 1992; Estigoni et al., 2014; Vromans and Faghri, 2018).

Limitations in current devices are reflective of their design philosophy, as most place heavy emphasis on achieving a target movement, which not only limits the range of movement produced but also takes focus away from network behaviour in a more general sense. Moving away from movement orientated design goals may allow devices

to create a wider range of more natural movements by better accessing spared spinal circuitry.

The introduction to this thesis will provide background on the current understanding of both the fundamental and higher order systems of motor control, providing insight into how BMI performance may be improved. It will also cover key concepts in machine learning that that will be used later in this thesis for flexible control of stimulation in a variety of settings. Together this should explain the current gaps in device design and how novel algorithms integrated into a BMI may allow for true closed loop control of the paralyzed limb.

1.2 Theories of motor control

1.2.1 The “degrees of freedom” problem

Within the physical constraints of the musculoskeletal system there are a redundant and significantly large number of ways to achieve a task, across the range of trajectories and muscle activation patterns. Selection of a specific strategy for a given task involves selection from a huge array of possible combinations requiring significant computational effort. The difficulty of this task appears at odds with the efficient and reliable way in which movements are performed (Frère and Hug, 2012). Two theories have been proposed to solve this “degrees of freedom” (DOF) problem. The first is the optimal control hypothesis, wherein the overall strategy for a task is primarily determined via afferent feedback. This feedback modifies descending drive such that the movement is optimized to maximize efficiency (Tresch et al., 2002; Corey B Hart and Giszter, 2010; Bizzi and Cheung, 2013; Hirashima and Oya, 2016) The other theory is the muscle synergy hypothesis’ wherein it is suggested that complex coordination of muscle activity is generated by combining modules or patterns of control together (Bernstein, 1968). The complexity is reduced from choosing many different muscle activations to instead choosing from a smaller range of motor modules. The ‘optimal control hypothesis’ has largely fallen out of favour in the field primarily due to the difficulty in determining what precisely the nervous system defines as “optimal”. The ‘optimal control hypothesis therefore falls outside the remit of this thesis; however, it is mentioned here as much remains unclear regarding recruitment and the neural origin of muscle synergies.

1.2.2 The muscle synergy hypothesis

Muscle synergies are repeatable patterns of muscle activity over time, whereby certain muscles are organized to contract together and others may be kept inactive (Bizzi and Cheung, 2013). These patterns link the activity of multiple muscles thereby reducing the DOF to recruitment of a limited set of synergies. Encoding of muscle synergies is suggested to occur at the level of the spinal cord, however the precise details of this encoding are still a hotly debated issue. It has been demonstrated that similar muscle synergies can be extracted during locomotion from species with differently sized cerebral cortex (Dominici et al., 2011). The similarity of these synergies, despite the difference in cortical complexity, indicates that the neural candidate is likely at the level of the brainstem or spinal cord (Dominici et al., 2011). This is supported by studies in stroke patients with damage to the motor cortex where patients demonstrated merging of muscle synergies in the affected arm compared to the healthy arm (Cheung et al., 2012; Pan et al., 2018). Merging of synergies suggests that changes in motor control are made because the cortex is unable to fully recruit intact networks located at a lower level. Work has been done in frogs, mice and primates has shown that stimulation of interneurons in the spinal cord can recruit patterns of co-ordinated muscle activity (Corey B. Hart and Giszter, 2010; Levine et al., 2014; Takei et al., 2017). Despite these findings it is still unclear what the direct neural encoding is and therefore they must be observed indirectly through their effect on motor output in the form of patterns extracted from electromyography (EMG) recordings (Corey B Hart and Giszter, 2010; Bizzi and Cheung, 2013).

To understand how muscle synergies are extracted from EMG signals the concept of data dimensionality must be understood. Data dimensions refers to the number of variables used to describe the data. A dataset describing a group of people may include variables such as their height, weight, sex, etc. These variables may be related to each other, such as height and weight and patterns can emerge under close inspection. It may be that the pattern relating height and weight describe a similar amount of variance as either variable on their own. These patterns can be more useful than the individual measures in the same way that the body mass index may be more useful for some purposes than either height or weight on their own. Dimensionality reduction algorithms seek to identify these patterns and describe the dataset using a smaller number of patterns. Synergy extraction algorithms attempt to reduce the dimensionality of a dataset of EMGs to a smaller set of patterns of muscle activations that are easier to understand

and analyse (Tresch and Cheung, 2006; Lacquaniti et al., 2012). In the case of the muscle synergy hypothesis this reduction in complexity is assumed to be the reason the body does this, and therefore a real neural encoding is being observed. It has been instead suggested that the synergies extracted are no more real than the hypothetical height/weight pattern mentioned, and that synergies emerge from EMG data because of the biomechanical constraints of the task (Valero-Cuevas et al., 2009; Kutch and Valero-Cuevas, 2012; Groote et al., 2014). The majority of evidence has fallen in favour of synergies being reflective of the activity of networks of interneurons in the spinal cord, but until this has been demonstrated conclusively the alternative must be kept in mind when considering muscle synergy analysis (Corey B. Hart and Giszter, 2010; Levine et al., 2014; Takei et al., 2017).

For use within a BMI device, muscle synergies appear to be a useful measure of network output during efficient motor control. Linear combination of muscle synergies have been shown to more efficiently describe muscle activity across a wide range of movements in humans, including reaching tasks, trunk stability and walking in comparison to models based on the activity of individual muscles alone (Takei and Seki, 2010; Lacquaniti et al., 2012; Roh et al., 2012; Wojtara et al., 2014). The impairment of motor control in those with altered synergy recruitment is also reflective of their role in efficient control. Synergy analysis was performed on the impaired and unimpaired limb in stroke patients during movement (Safavynia et al., 2011; Cheung et al., 2012; Pascual-Leone, 2013; Israely et al., 2018). The synergies identified in the impaired limb resembled that of the unimpaired limb, however some synergies were altered. Some synergies were merged together, whilst some synergies were fractionated into new smaller patterns. Critically, the degree of merging and fractionation was found to be related to both the severity of impairment and the time since the initial injury, with merging being greatest in the most severely impaired, and fractionation increasing as time passed. This suggests that cortical damage results in disorganization of the modular synergy system with a resulting impairment of motor control. Muscle synergies have also been shown to more efficiently control a virtual arm than when controlled using individual EMG features (Antuvan et al., 2016; Valk et al., 2019). This evidence supports the hypothesis that synergy information is present during efficient control of the musculoskeletal system. Muscle synergies not only solve the redundancy problem of selecting an efficient muscle activation pattern, but may also account for much of the nonlinearity present in producing those patterns (Brezina et al., 2000; Bizzi and Cheung, 2013). Muscle synergies therefore present a

natural improvement as a control mechanism for a BMI device compared to movement orientated devices.

1.2.3 Agonists, antagonists and synergists

One of the major complexities in the DOF problem is the number of muscles that directly oppose each other. In the upper leg the contraction of the hamstrings and the contraction of the quadriceps are diametrically opposed to each other and are referred to as an antagonist pair. The definition of which muscle is the agonist, and which is the antagonist is determined in a task dependent manner. The quadriceps are made up of four muscles; the rectus femoris, vastus lateralis, vastus medialis and vastus intermedius that all work together to extend the knee and are termed agonists when this is the desired movement. This in turn makes the hamstrings; semitendinosus, biceps femoris and semimembranosus, antagonists, as they work in opposition to the movement of the knee, as flexors instead. Muscles are further defined as synergistic when they are active at the same time during a task, but this does not indicate that they are working together or indeed for the same purpose. As mentioned, many synergistic muscles may actively impede efficiently carrying out a task, but this may still form an important role in motor control. This naming convention is useful in certain contexts, however, as is so often the case, this is a simplification of what really occurs. Very few muscles are entirely antagonistic to each other, and their function is determined in a task dependent manner. Further complicating the issue are multi joint muscles, or biarticular muscles, where the function of a muscle can be dependent on a variety of factors such as joint position or coactivation of contralateral muscles (Eccles et al., 1957; Buchanan et al., 1986; Knikou and Rymer, 2002). Ultimately the network recruiting these muscles must receive input from a wide variety of sources, including descending control and afferent feedback.

1.3 Systems of motor control

1.3.1 Base components

The fundamental unit of motor control is the motor unit which consists of a motor neuron innervating a number of muscle fibres. The cell bodies for motor neurons are found within the spinal cord in the ventral horn, but their axons extend out of the central nervous system (CNS) into the periphery where they are bundled together in nerves surrounded by fascia. Stimulation of these motor neurons, either at their cell body or their axons, results in contraction of the muscle fibre which ultimately produces motor output. Motor

neurons are recruited in a graded fashion depending on their size, from smallest to largest (Henneman et al., 1965).

1.3.2 Descending efferent signals

Higher centres of motor control are in frequent communication with motor neurons in the spinal cord, and each other. The major descending pathways for motor control are the corticospinal, corticobulbar, reticulospinal, bulbospinal, rubrospinal and pontospinal tracts (Kuypers, 1981; Lemon, 2008). It is the damage to these descending tracts that causes the loss of volitional control in spinal cord injury. How “top-down” control co-ordinates with lower centres of motor control is still an open question, however it is likely to be handled by cortical centres, such as the motor and premotor cortex, and networks of interneurons at the level of the spinal cord working together (Tresch et al., 2002; Corey B Hart and Giszter, 2010; Bizzi and Cheung, 2013).

1.3.3 Central pattern generators

One of the more important interneuron networks are central pattern generators (CPG). These circuits are crucially important for rhythmic tasks such as locomotion as they produce cyclical output patterns without descending control (Grillner, 2011; Guertin, 2013). The independence of these centres has been demonstrated dramatically in the mesencephalic cat, an animal model wherein a transection is made between the superior colliculi and the thalamus. Via stimulation of the reticular formation these animals could be made to walk and even keep pace with changes in treadmill speed (Shik and Orlovsky, 1976; Mori et al., 1978). Although these centres can function without descending input, afferent signals play an important role in modulating patterns in response to perturbations (McCrea and Rybak, 2008).

The cyclical activity of CPGs is due to what are known as half-centre oscillators. The rhythmic output of cells is not due to an intrinsic property of the neuron, but its reciprocal excitation/inhibition with another neuron. As the activity of the cell rises, it causes its own inhibition via excitation of another neuron which has mirrored connections. Whilst this cyclical activity is an important output of CPGs, there is evidence to suggest that these networks can be used flexibly to control motor output in a variety of conditions, not all of which require or utilize rhythmic activation (York et al., 2019).

1.4 Afferent feedback

Afferent fibres make up the majority of axons within nerve, outnumbering, motor axons 9:1 and play a significant role in healthy motor control (Gesslbauer et al., 2017). Control of movement is possible in the absence of sensory feedback but swiftly becomes more inaccurate as time increases or as obstacles are encountered (Gandevia et al., 1990; Nielsen and Sinkjaer, 2002). This is especially true for the nervous system where afferent fibres directly synapse onto motor neurons providing immediate access to error signals during movement. Removal of these fibres in various conditions causes distinct motor deficits that increase as a task continues in the absence of other sources of feedback. Muscle afferents are classified into groups I-IV according to their diameter and they respond to specific sensory inputs (Lloyd, 1943; Macefield et al., 1989) These fibres are the primary source of our inherent sense of muscle velocity and the position of the limb in space, which is termed proprioception.

1.4.1 Muscle spindles

The major sensory organ responsible for proprioception is the muscle spindle. Muscle stretch is detected by the muscle spindle and relayed to the central nervous system by the afferents primarily via the muscle spindle primary (group Ia) and muscle spindle secondaries (group II). These fibres convey different information regarding stretch. Ia fibres are primarily related to changes in the length of the muscle and are highly adaptive, in that they rapidly cease firing when muscle length ceases to change. This is in contrast to group II fibres which do not significantly respond to changes in muscle length (Darby and Frysztak, 2013). The role of group II fibres can be intuitively understood as a more passive understanding of the muscles position in space versus reporting on movement. In terms of reflexes Ia afferents are responsible for the stretch reflex and the characteristic H-reflex where Ia fibres monosynaptically excite their homonymous motor neurons in response to stimulation (Eccles et al., 1957). Ia fibres also control firing of the synergistic antagonist muscles via polysynaptic inhibitory innervation of their motor neurons. This facilitates the response known as reciprocal inhibition wherein antagonist muscles are inhibited during activation of the agonist.

1.4.2 Golgi tendon organ

The other sensory organ responsible for proprioception is the Golgi tendon organ. In contrast to the muscle spindle, this organ signals for changes in muscle tension due to

contraction. This is present even in the absence of muscle length change and is therefore more representative of muscle force generation. Golgi tendon organs are innervated solely by Ib fibres which go on to project to both homonymously and heteronymous motor neurons making polysynaptic inhibitory and excitatory connections with them. This results in autogenic inhibition which regulates muscle contraction to avoid fibres damaging themselves. They excite antagonist muscles as part of the autogenic reflex.

1.4.3 Nociceptors and cutaneous fibres

The remaining muscle afferent fibre groups, III and IV are more widely dispersed along with Aβ and C fibres with sensory endings terminating in the skin and act as nociceptors throughout (von Düring and Andres, 1990; Dubin and Patapoutian, 2010; Jankowski et al., 2013). Some group II fibres also act as cutaneous sensors and nociceptors (Nagi et al., 2019).

1.5 Brain machine interfaces for the purposes of motor control

The term BMI was first used by Jaques Vidal who was inspired by the work of Hans Berger in 1924 when he first described electroencephalogram (EEG) activity in the brain (Vidal, 1973; Vidal, 1977). Vidal used visually evoked potentials in the visual cortex to guide a digital cursor through a simple maze. This provided proof of concept that neural activity could be used as a control mechanism. The umbrella term of BMI now refers to a variety of devices including both invasive and non-invasive alternatives. Non-invasive BMI's attempt to measure neural activity without directly interfacing with nervous tissue, most commonly using EEG signals recorded from the scalp (Asghari Oskoei and Hu, 2007; Atzori et al., 2014; Bouton et al., 2016). Invasive BMIs instead use neuronal firing rates measured using electrodes placed either in close proximity or directly within nervous tissue (Brus-Ramer et al., 2007; Campos et al., 2008; Zimmermann et al., 2011; Dorn et al., 2012; Nishimura et al., 2013; Giagka et al., 2013; Raspopovic et al., 2014; Grahn et al., 2014; Pani et al., 2016; Alam et al., 2016; Dura-Bernal et al., 2016).

The concept that links BMIs is that neural activity in some form is recorded and used to drive the activity of another machine. These machines can range from a digital cursor, to a neural prosthetic hand, or, as is the goal of this thesis, simulating electrodes within the nervous system. The variety of developed devices and the diversity of solutions to a common problem could indicate an underlying flaw to the way in which the problem is approached (Baranauskas, 2014). Advancement within the field is often supposed to be

due to an increase in neural “resolution”, with increased sizes of recording or stimulating arrays (Nordhausen et al., 1994; Maynard et al., 1997; Branner and Normann, 2000; Davis et al., 2016). In the case of invasive BMIs, it is supposed that given a large enough array of electrodes, that could record from every neuron related to a given activity, performance could become indistinguishable from natural activity. However, oftentimes large leaps in performance can be achieved with novel interpretation of neural activity (Baranauskas, 2014). A shift away from decoding with respect to the observer, to decoding with respect to the target goal achieved markedly better results than more technological capable devices (Gilja et al., 2012). This result suggests that improvements may be possible without technological leaps, but by using devices available today in better ways.

There is currently no consensus on how to compare the performance of BMIs (Asghari Oskoei and Hu, 2007; Eftekhar et al., 2010; Baranauskas, 2014; Mehryar, 2014). Comparison is difficult as devices often target different injury states, movements, neural activity and species. The information transfer rate of the device has been proposed as a universal measure but this has only been reviewed with respect to devices applied to a centre-out reaching task (Baranauskas, 2014). Information transfer rate is difficult to calculate appropriately when the task differs from a centre-out reaching task, and even more so when applied to devices with the aim to restore motor control. Despite this difficulty, it is demonstrative that of the devices reviewed by Baranauskas, the best performing devices had the highest information transfer rate. Even during simple movements the estimated information transfer rate of the human nervous system is in the region of ~10 bits/s, a large jump from the rate current invasive BMIs achieve of ~2 bits/s, especially as bit rate is measured on a logarithmic scale (Fitts, 1954). Whilst the task of controlling a prosthetic and re-innervating a paralyzed limb require different approaches, the overall goal is the same; to produce a movement that matches the intention of the user. Rather than precise control over motors the output device is instead imprecise control over muscle activity (measured as EMG waveforms). There are layers of abstraction and non-linearity between neural decoding and the desired output; however, the core task remains the same and therefore maximising information transfer is likely to have a large effect on device performance. The best information transfer was achieved by examining how neural activity encodes for a given task or activity, and what that activity represents. Neural activity likely relates to a whole range of parameters, rather than any single variable of movement (Panzeri et al., 2015). Therefore, interpretation of neural activity must account for complex non-linear relationships such

as between motor neuron firing rates and contraction, and the most important information must be accounted for. Muscle synergies are an attractive target for accounting for these non-linear relationships in motor control.

Identifying muscle synergies and tailoring stimulation paradigms to correspond with one another could result in a greater complexity of activations and inhibitions that mimic natural movements. Experimental data shows that interneuron firing rates in the frog spinal cord reflect the same synergy information as obtained from analysis of muscle activity (Corey B Hart and Giszter, 2010). A pairing of these two forms of neural activity may produce a BMI that can evoke more natural movements in a paralyzed limb. Synergies could improve performance by taking advantage of natural co-ordination within motor output allowing design of stimulation paradigms that best elicit those synergies.

1.6 Machine learning

The field of machine learning covers a huge array of techniques that all share the general principle of attempting to recreate the learning process electronically. Machine learning was initially a theoretical approach to training networks in a biologically inspired fashion to recreate biological like thinking. Following several AI “winters”, machine learning has finally entered mainstream use in the form of speech recognition, image analysis and trend prediction algorithms. This surge has largely been driven by increased access to computing power and increasingly large datasets. It is a major advantage of machine learning that algorithm performance can be improved by increasing either of these variables. These algorithms also excel in situations where traditional modelling approaches are held back, either due to a lack of understanding of the initial relationship or require greater adaptive capabilities.

In gross overview, machine learning algorithms attempt to model a given relationship between two datasets in order to make predictions from this model. This can be further divided into supervised and unsupervised learning. This refers to whether the data is initially labelled or not with relevant information. Supervised learning might use a set of pictures with the contents of the image already described, whereas unsupervised learning must create these labels as part of the learning process. There is a further subdivision into classification and regression problems. For example, a classification program might be asked to sort a set of pictures into different classes of animals within the picture. A regression problem however asks for a continuous output to be predicted,

the classic illustration of which is to predict stock prices based on previous months reports. As another example of an unsupervised learning regression problem, a special type of artificial neural network (ANN) known as an autoencoder has been used previously for muscle synergy extraction (Spüler et al., 2016). This is an example of using machine learning to learn the structure of data and can be combined with other algorithms for increased performance in some applications.

ANNs are a particularly popular topic within machine learning at present. These networks are at least in part designed to resemble the process of integrating information through a connected network of “neurons”. The functional unit of an ANN is a single neuron with inputs and outputs, an example of which is shown in Figure 1-A (A). The incoming values are multiplied by their weights, summed and then passed to the activation function of the neuron. This activation function applies some operation to the input and then provides that as the output. In principal this system is very simple, and in this case incapable of anything interesting. To make these networks more useful two things are required; more neurons and a way to alter weights towards a specified goal.

Including more neurons is relatively simple to explain, it simply involves adding more connections between nodes, typically separated into different layers, with each layer only connecting to the next in series (although more complex architectures have been used for some purposes). The separation into layers is shown graphically in Figure 1-A (B) which are commonly termed as input, output and hidden layers. Hidden layers are termed such because it is not possible to directly observe their operation as a result of training, only the final output. Networks for extremely complex tasks may have multiple hidden layers of thousands of neurons, or even multiple networks connected in series. These larger networks are termed deep learning. Although there is no formal definition of the term any network of more than a handful of layers may reasonably be considered deep.

Altering the weights between neurons requires a method and goal to drive this alteration. The goal is termed the loss function, with the goal being to minimize the value of the loss function relating the output of the network and its matching label. Common loss functions include the mean squared error or the categorical cross entropy. The minimum value of the loss function is found via gradient descent, a simplified graphical depiction of which is shown in Figure 1-A (C). Determining the minimum value of this parabola requires the function gradient (or direction of change) and a quantity to move down this gradient. The gradient is determined simply by taking the first derivative and the step size is determined

by the user (this is also known as the learning rate in machine learning). This process is repeated iteratively, each step moving towards a minimum, in this case a global minimum. However as seen in Figure 1-A (D) this may be only a local minimum, with gradient “humps” preventing gradient descent from finding the global minimum. The choice of start position within this function space can result in significantly different outcomes between different training attempts. Careful choice of learning rate is essential to avoid this. Too small and the network may become stuck in these local minima, too large and the network will be unable to settle into any minima at all. Gradient descent is computationally expensive if applied sequentially to each layer of weights. As mentioned previously machine learning went through droughts of development known colloquially as an AI winter. One of the important developments that allows ANNs to alter weights efficiently for deep networks was the backpropagation algorithm. This algorithm calculates the gradient of the loss function starting from the output layer and carrying terms of the calculation in reverse order through the network, hence the gradient propagates backwards.

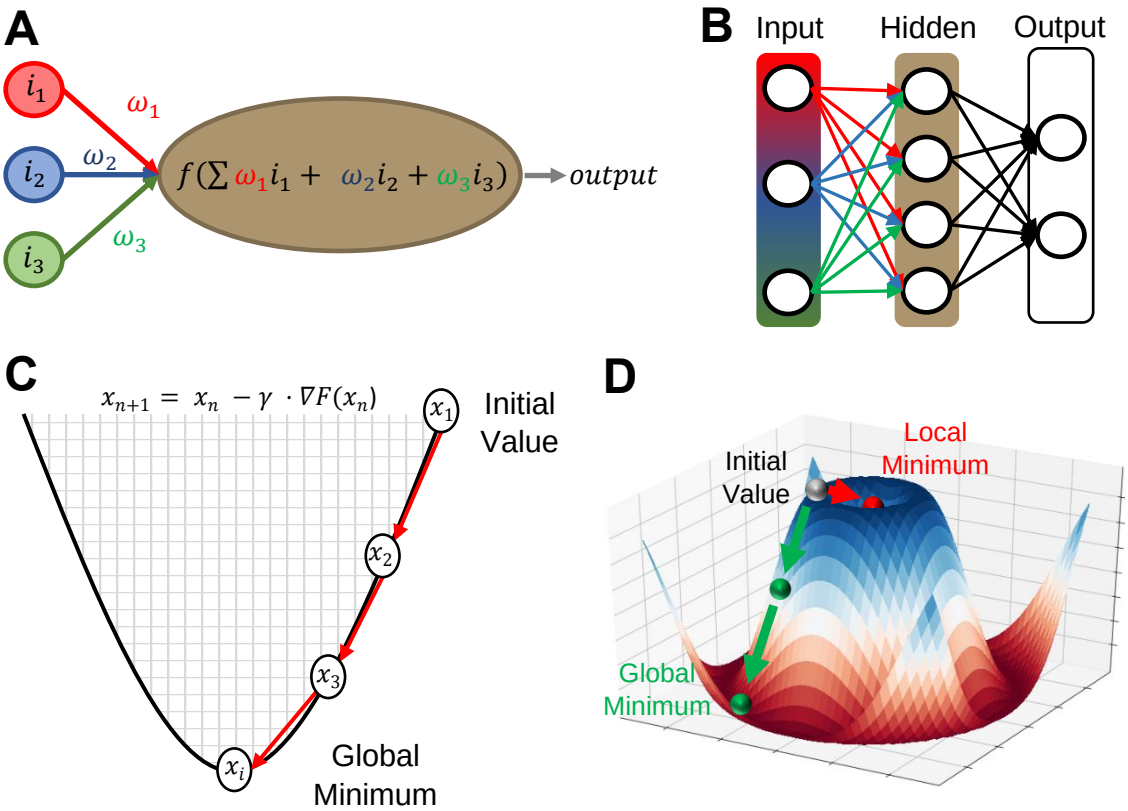

Figure 1-A: **Concepts in machine learning**. A: An individual node of an ANN takes the sum of its inputs, i, multiplied by their respective weights, ω, and applies an activation function, f, to determine its output. f may take any form but is usually a non-linear function with some degree of "thresholding" whereupon certain values cause the node to "fire" similar to biological neurons. B: Nodes are grouped into layers with each node connected to each node in the next layer. These layers have different names; input layers, where data is fed into the network, hidden layers, where most computation takes place, and output layers, where the results of the network are extracted. The weights and activation functions for each connection or layer may be different and are fine-tuned during training. C: Weights are adjusted towards a given target by minimizing a loss function. This is achieved via gradient descent. At a given point x the gradient, ∇, is determined and the next value is a set step, γ, down this gradient. This process is repeated iteratively until the algorithm reaches a global minimum, or in practice a set number of steps is reached. D: Gradient descent is not an infallible process; local minima can be found that are significantly greater than the global minimum. These local minima may not have a gradient to the true minimum and training stalls. As the initial value for weights is usually randomly determined it is possible that different training periods may yield significantly different outcomes depending on this initial value.

1.7 Aims and objectives

1.7.1 Synergy information has been shown to significantly improve the performance of motor control algorithms. There is currently no real time method that can relay this information to subjects or devices. Therefore, one aim of this thesis was to produce an algorithm that can extract synergy information in real time. During development of this algorithm the accuracy and speed of computation for detection of muscle activity onset and muscle synergy extraction was compared for the most commonly used methods. This algorithm was then applied to isometric knee extensions to identify the influence of proprioception on synergy recruitment. Following muscle synergy analysis of the knee extension a mechanistic explanation for these findings was provided by population modelling of interneuron networks at the level of the spinal cord.

1.7.2 FES of the peripheral nervous system is often performed in an ‘ad-hoc’ fashion wherein stimulation paradigms are tailored individually by experts observing and maximising stimulus-response for a given set up. To perform this automatically requires an algorithm that can learn a generalizable transfer function between electrical stimulus and neural response. For the second aim of this thesis: an ANN was designed to model this relationship and then predict the required electrical stimulus for a given output.

1.7.3 Experiments investigating spinal cord or cortical injury currently involve expensive and time intensive animal studies that involve significant impact on quality of life. A computational model that replicates motor deficits observed would reduce the time, cost and animals required for these experiments. Furthermore, computational models can highlight mechanisms of action that may not be easily understood from experimental data. Expanding upon the previously developed interneuron model, for the third aim of this thesis, alterations were made to the model to replicate different forms of nervous system injury. This model was then used as a simulated environment to test the previously described algorithms linked together as a closed loop BMI device.

Chapter 2: General Methods

2.1 General Rationale

Conceptually a BMI device has two major functions. Determining a desired output and producing that output. In practice it is also necessary to monitor the output produced and to provide some level of error correction. In an ideal example neural activity and the associated output are measured and manipulated at the level of specificity required. In other words, if a device can achieve its goal using a gross measure of neural activity, such as EMG recordings, this is superior to one that requires a more specific measure, such as spike firing rates. However, in most circumstances our understanding is limited as to what the level of specificity should be, or in our ability to access it. Some devices attempt to address this problem by interfacing with the nervous system at the level of most specificity e.g. neuronal spikes (Jackson et al., 2006; Shanechi et al., 2014; Alam et al., 2016; Bouton et al., 2016). However, this solution requires complex models of system dynamics to predict how individual neurons or spikes combine to produce gross output. These models are often insufficient as demonstrated by the fact that task performance is improved using a general measure of neural activity such as local field potential (LFP) (Flint et al., 2013; So et al., 2014; Stavisky et al., 2015). Indeed, the synergy hypothesis suggests that the CNS may take advantage of generalized patterns to solve the motor control problem. The level of detail required is instead probably specific for a given task. For the needs of a device controlling the paralyzed limb, the target is to reproduce natural control of the limb as closely as possible. From this perspective muscle synergies seem immediately attractive as an output measure. This in turn necessitates collection of EMG recordings as a non-invasive measure of muscle activity. This has the additional benefit of being widely used in a clinical setting. The EMG waveform consists of indirect measurement of the summed electrical activity of muscle fibres as they contract. Whilst there are limitations to our understanding of how EMG waveforms translate into end point force, ultimately all active movements are the product of EMG activity within different muscles. Therefore, a device that could specifically produce a desired EMG could theoretically recreate any desired synergy. This argument then determines the levels of specificity the device aim for: output measured at the level of synergies, created by input aiming at the level of EMG signals. In this section I will expand upon the methodologies used to achieve this goal.

2.1.1 Rationale for an algorithm-based approach

At the gross level most BMI research can be divided into two fields; device development (getting information into and out of the body) and algorithm research (what is done with this information). Whilst device development is an exciting field with new advances regularly increasing the number and quality of recorded signals that are accessible, it is instructive to the importance of this work to briefly discuss why devices are ultimately subordinate to algorithms. Imagine a perfect device, one that can record and stimulate every individual neuron in the body with infinite accuracy. Whilst this device would truly be a marvel, it would not be possible with algorithms currently available to readily improve upon current treatment options. Indeed, the sea of available information would make it very difficult to determine which information is relevant to a given task. Consider the alternative of the perfect algorithm, one that can perfectly translate information recorded into the required steps to produce the desired effect. Here the way forward is extremely clear, to develop a device that can record and stimulate the specified locations. In this hypothetical, the clear goals provided by the perfect algorithm lead to smoother development than the current process of incrementally increasing recording density with no clear understanding of what the task requirements are (unless the requirements for a perfect algorithm are a perfect device, but such a Sisyphean task can still be better approximated with available tools than with available algorithms). Hence work in this project has focussed on the development of better algorithms for motor control and it is assumed that the engineering developments required to implement them can be achieved given time. In a similar vein, whilst consideration is given to algorithmic complexity, it is presumed that the increase in speed that could be achieved by implementation in an FPGA or ASIC device (an obvious necessity for an implantable device) would dwarf the effects of more efficient code implementation.

2.2.1 Subjects and Ethical approval

Data collection from humans was conducted according to the Declaration of Helsinki and all experimental protocols were approved by the University of Leeds Research Ethics Committee (reference number BIOSCI 16-004). 17 healthy subjects of mixed gender (male = 9, female = 8) with an age range of 18-30 (24.4± 2.57 years) were recruited to participate in this study. Exclusion criteria included previous knee or leg injuries, if participants had done exercise within 48 hours prior to testing, knee stiffness or self-reported pain, use of recreational or performance enhancing drugs, ingested alcohol in

the previous 24 hours or were unable to provide informed consent. Subjects provided informed written consent to the study, noting possible risks associated with the activity.

Experiments and procedures were performed in a manner that conformed to the United Kingdom Animals (Scientific Procedures) Act 1986. Approval was granted by the local Animal Welfare and Ethics committee (University of Leeds). 8 male Wistar rats (≈250g) were used for acute surgery conditions and were killed following each surgery.

2.2.2 Dataset size

A brief discussion on the reasons for the size of datasets described throughout this text. In section 3.3.2 comparisons are made between the performance of different synergy extraction methods on synthetically generated muscle activity. Comparisons were made using one-way analysis of variance (ANOVA) followed by a Tukey's multiple comparison test. This is the most straightforward example of determining the required sample size; as the data is synthetically generated it is possible to generate an initial estimate of the dataset and then easily increase it as required to reach the required sample size. Power analysis was performed using G*Power version 3.1.9.7. This power analysis was initially calculated from 50 examples with an α value of 0.05, an effect size calculated post-hoc as 0.535 and the appropriate group means and the within group standard deviation approximated as 0.3. This analysis predicted that a sample size of 64 would be required to reach a power of 0.95. As it is easy to increase the dataset size using the synthetic synergy generation method described in section 2.4.5 it was decided to increase this to 100 samples.

Choice of sample size is more complex when considering other aspects of this thesis. Descriptive statistical methods are not commonly applied to muscle synergy analysis as they are primarily a method of identifying patterns within a dataset. The dataset is required to be representative of the population and therefore must be of a certain size, but this is not formally defined as with other statistical tests, as muscle synergies analysis is of a more exploratory nature. Therefore, the number of participants selected was chosen to match similar studies within the literature to ease comparison.

In machine learning determining the required sample size is often an empirical process as more traditional methods of determining sample size such as power analysis are not appropriate. Power analysis is unable to predict the required dataset size as there is no null hypothesis to refute; only the end performance of the network. Often times networks are trained on an initial "rule-of-thumb" estimate based on prior experience, such as the

“one-in-ten” rule wherein one variable can be predicted for every 10 examples (Baum and Haussler, 1989; Haykin, 2008; Alwosheel et al., 2018). If following initial training the accuracy of the model is insufficient then more data is collected, or the model is adjusted to try and fit the limitations of the dataset. It is often true that the larger the dataset the better the performance of the model however the complexity of the model and the relationship under investigation can significantly alter the amount of data required (Halevy et al., 2009). Using the “one-in-ten” rule combined with the two parameters the network was asked to predict (width and voltage) it would seem that the network would require 20 animals for accurate training. However, it was found after early analysis that performance was greater than predicted on a limited dataset and a smaller number would likely suffice. To minimize the required animals a streamlined version of the process of network training and prediction described in Chapter 4 was repeated after each surgery. From this it was determined that the model was capable of sufficiently accurate predictions after 8 animals.

2.3 Coding

Algorithms were tested and run using custom written Python 3.6 code and run on a Windows 10 device, Intel® Core™ i5-8400 CPU, 16GB DDR4 ram at 3200Mhz. Code is available via GitHub at https://github.com/gareth-york/neural-bridge. MIIND is available at http://miind.sourceforge.net/ and the model files and simulation results are accessible at https://github.com/hugh-osborne/isotask. Synergy extraction methods were implemented using the scikit-learn library, excepting for NMF which used the nimfa library. ANN’s were implemented using Keras running a Tensorflow backend.

2.4 Synergy Analysis

Whilst any task is made up of individual EMG’s (and the activity of individual motor neurons within them), this is not the complete picture. To achieve the end goal of a task there are an almost infinite number of combinations of EMG’s that could perform the movement due to the overlap in function of certain muscle groups when considering force endpoints, as well as the opposing nature of agonist and antagonist muscle groups. The large overlap of combinations of muscles and contractions which could achieve a task is known as the DOF problem and it contrasts strongly with the repeatable and efficient (but not maximally efficient) way in which tasks tend to be carried out (Bizzi and Cheung, 2013). One proposed solution to this problem is the muscle synergy hypothesis, wherein instead of calculating individual EMG profiles, the task is simplified to patterns of muscle

activity that are combined in a smaller feature space. Synergies have been shown to improve control of virtual and prosthetic limbs compared to the use of individual EMG profiles (Antuvan et al., 2016; Valk et al., 2019; Furui et al., 2019). To extract synergies from EMG waveforms a variety of algorithms have been used, which have been previously compared (Tresch et al., 2006). These comparisons have been repeated here in combination with a variety of methods for determining which parts of the EMG signal are of interest. These algorithms were then used to extract synergies from an isometric knee extension at different angles to examine the role of proprioception in synergy recruitment. A population interneuron model was developed to model the effect of afferent feedback on synergy recruitment using the model MIIND (Multiple instantiations of interacting neural dynamics).

2.4.1 Data Collection

Surface EMG was recorded from seven muscles of the subjects dominant leg; rectus femoris (RF), vastus lateralis (VL), vastus medialis (VM), semitendinosus (ST), biceps femoris (BF), medial gastrocnemius (MG) and tibialis anterior (TA) – of which the MG and TA were discarded due to low signal to noise (SNR) ratio. Data analysis was therefore performed on the five remaining muscle recordings. The skin was prepared for electrodes with shaving, cleaning with alcohol wipes and then application of conductive electrode gel. Data was sampled at 2 KHz using wireless Delsys Trigno IM electrodes. Electrodes were placed on the muscle belly, defined by landmarks based on anatomical observations: VL-between the greater trochanter and the lateral epicondyle; VM - on the distal fifth of the medial knee joint; RF - between the greater trochanter and the lateral epicondyle; VM - on the distal fifth of the medial knee joint; RF - between the anterior superior iliac spine and the superior pole of the patellar, and MG belly located in distal third of the medial knee joint (Rainoldi et al., 2004). Data was principally collected by Piyanee Sriya.

2.4.2 Movement Protocol

Subjects were asked to lay on a standard medical examination bed. They were then shown how to perform an isometric knee extension with the leg brace attached to their dominant leg. Subjects were shown the resulting EMG output recorded using a Delsys Trigno system. Subjects were asked to perform an isometric knee extension at maximal voluntary effort for five seconds, attempting to maximise RF activity. This was repeated six times with a three-minute rest between contractions. The dominant knee was fixed at

one of four angles using a Donjoy TROM locking knee brace at 0°, 20°, 60° and 90°. The angle of the knee was always measured against the hip joint and the bony prominence on the outside of the ankle. Data was collected in two different positions and sessions for each subject. In position one the participant was supine with both legs flat against the bed. In position two the contralateral leg was kept bent such that the foot is flat against the bed so that both the knee and hip are fully flexed. The position selected for each subject was randomized for their first session. In the second session the subject performed the task in the other position.

2.4.3 Data Pre-processing

For testing of onset/offset detection algorithms signals were tested both with and without standard filtering procedures. The filtering process involved an initial band-pass filter (high pass = 20 Hz, low pass = 450 Hz, second order Butterworth filter), followed by rectification and then finally a zero-lag high-pass filter (5 Hz, second order Butterworth filter) to remove frequency changes induced by rectification. Each EMG channel was normalized to the maximum value for that channel across all six contractions. For testing of synergy extraction algorithms, filtering was always used, and visual inspection was used to segment data into equal sections containing one burst. The synergy extraction was performed on the averaged values across contractions for each EMG channel.

2.4.4 Onset/offset-detection

In high SNR conditions muscle contractions appear in EMG signals as “bursts” which are sustained increases in the electrical signal. For most analysis only the contraction period is of interest and therefore the signal burst must be separated from background noise. The simplest way to do this is via visual inspection, which the human eye is excellent at, but this is obviously not available to a computer algorithm. The most commonly used automated method is a thresholding algorithm, wherein activity above the given threshold is activity of interest and anything below threshold is discarded as noise (Staude et al., 2001). The signal amplitude can be used for thresholding, but another common measure is the root mean square (RMS) of “windows” of data. Another value that has been used is sample entropy (SampEn), a measure of the entropy or variability of the signal (Richman and Moorman, 2000; Zhang and Zhou, 2012). The accuracy of onset detection and speed of calculation varies but it has been previously shown that SampEn is an effective method for detecting activity onset in signals with aberrant spiking activity (Zhang and Zhou, 2012). This is important in the context of a BMI device targeting the

paralyzed limb as it is common to see involuntary spikes in the EMG signals of spinal cord injured patients due to hyper-excitability of the motor unit (Elbasiouny et al., 2010). In order to determine the most suitable threshold for this device the three measures previously mentioned, amplitude, RMS and SampEn were tested for speed of calculation, accuracy compared to visual inspection and their susceptibility to increasing levels of noise and random spiking activity.

The three measures examined here were compared using previously collected EMG signals from the upper leg muscles. The signal is split into windows of time 32ms long with a 4ms overlap between windows. There is a compromise between processing time and onset and offset resolution in the window length and overlap. The values used here were found experimentally to have a good balance of accuracy and computation speed. Onset and offset are determined as the window when the threshold value is crossed. The performance of each measure can then be compared to visual inspection. The most straightforward thresholding measure is to simply use the signal amplitude (or in this case the average of the windowed section). RMS is another commonly used method for onset detection and is also sometimes used as a measure of force produced. RMS is calculated using equation (1):

$$x_{rms} = \sqrt{\frac{1}{x}(x_1^2 + x_2^2 + \cdots x_n^2)} \tag{1}$$

The most complex measure examined here is the SampEn of the signal. From the time series with length $n, \{x_1, x_2, x_3, \ldots, x_n\}$ a template vector with length m is constructed. Within this template vector, vector pairs are compared using a distance function wherein pairs are said to match if their distance is less than r and the number of matching pairs counted as B^m. This is repeated for the template vector A^m with length $m + 1$. From this the SampEn of a signal can be calculated for a given value of m, and r by taking the negative logarithm of these two counts as in equation (2):

$$SampEn(x, m, r) = -\ln(\frac{A^m(r)}{B^m(r)}) \tag{2}$$

To determine the threshold for each measure Otsu's method was used. Otsu's method is most commonly used in image filtering tasks to separate images into foreground and background. However, at its essence this task consists of separating a signal into two classes based off some threshold value (Otsu, 1979). In this case our two classes consist of signal of interest and noise. This was found to produce better results across all signals than a predetermined threshold value or a percentage-based threshold e.g. 30%

maximum value. Otsu's method seeks to minimize intraclass variance in the signals histogram by comparing the variance across all possible threshold values. This is calculated with equation (3):

$$\sigma_w^2(t) = \omega_0(t)\sigma_0^2(t) + \omega_1(t)\sigma_1^2(t) \tag{3}$$

Where ω are the probability weights of the two classes separated by threshold t and σ is variance. The probability weight for separation into two classes with a histogram binning of L can be found with equation (4):

$$\omega_0(t) = \sum_{i=0}^{t-1} p(i) \tag{4}$$
$$\omega_1(t) = \sum_{i=t}^{L-1} p(i)$$

The algorithm then searches through all threshold values and finds the threshold that minimizes the $\sigma_w^2(t)$. Measures were then compared for speed of calculation and accuracy compared to visual inspection.

To examine each measures susceptibility to disruption by sources of noise additional tests were carried out. Differing levels of gaussian noise were added to the test signal corresponding to no, low and high levels of additional noise (scaled to 0, 0.5 and 1 of signal amplitude). It is noted that the original signals had an unknown level of noise present, but that this was deemed a high SNR recording based off prior experience. Even signals with relatively high SNR can still be contaminated with brief but frequent aberrant spiking activity. It has been suggested that SampEn is a method for addressing this activity that an amplitude-based threshold would not. Spikes were added to the signal in increasing frequency that consisted of a spike between maximum and minimum signal amplitude over the course of 5ms. This was also combined with the same process of increasing levels of noise. Finally, it was noted that Zhang and Zhou did not include standard filters in their paper examining SampEn's suitability for onset detection (Zhang and Zhou, 2012). Therefore, the effects of standard filtering process was examined on the accuracy of each measure in signals with aberrant spiking.

2.4.5 Synthetic muscle synergy generation

In comparison to onset/offset detection algorithms, where visual inspection provides easy access to accurate onset/offset values, there is no easy way to access the "ground truth" when performing synergy analysis on real datasets. It is not possible to know with 100% certainty that the synergies extracted reflect real control patterns that generated the movement (this is sometimes used as an argument that muscle synergies are due to

biomechanical constraints or a “ghost in the machine”). Therefore, it is useful to generate synthetic muscle activity from simulated synergies as this allows us to compare the effectiveness of different techniques (Tresch et al., 2006). Here generation of synergies was constrained according to commonly agreed facts regarding synergy structure. Namely that synergy vectors are non-negative and that activation coefficients share signal dynamics with EMG signals. The type of muscle activity to be generated was modelled to reflect the same isometric knee extension activity that the synergy extraction algorithm would be tested on. Therefore, the synergy vector was generated as 5 random integers constrained to a floating point between 0 and 1. Activation coefficients were generated using randomly selected contractions selected from the isometric knee extension dataset, taken from a random participant and random muscle. Based on initial analysis of the isometric extension task it was determined that two synergies were sufficient to describe this dataset. To provide maximum comparability to this dataset two synergies were also chosen for the synthetic dataset. A small amount of gaussian noise was added to the synthetic activation coefficient (scaled to 0.25 of signal amplitude). These represent the ground truth synergies and they were combined using matrix multiplication to generate 5 synthetic EMG signals. It was on these synthetic EMGs that the performance of different synergy extraction methods was compared using cosine similarity analysis.

2.4.6 Cosine similarity analysis

Determining the degree to which two vectors are related is a complex task, with a variety of statistical methods available, such as Pearson’s correlation or cosine similarity analysis. Cosine similarity analysis measures the cosine angle between vectors in a way that is less sensitive than other methods to differences in Euclidean distance (having different magnitudes in the projected multidimensional space). This value ranges between 1 and -1 which corresponds to both extremes of similarity and dissimilarity. The cosine of two vectors $\mathbf{A}$ and $\mathbf{B}$ can be calculated using equation (5):

$$\cos\theta = \frac{\|\mathbf{A}\|\|\mathbf{B}\|}{\mathbf{A}\cdot\mathbf{B}} \tag{5}$$

Cosine similarity analysis was used in a pairwise fashion to determine the similarity between synergy vectors and activation coefficients across both simulated datasets and human recordings (Rimini et al., 2017). In the case of comparing synergy extraction algorithms across the simulated datasets, each algorithm’s extracted synergies were normalized to the average cosine similarity with 100 randomly generated synthetic

examples. The cosine value between these random examples and the extracted synergies reflects any bias in the synthetic synergy generation algorithm. Normalizing to this value should remove this bias.

2.4.7 Synergy extraction algorithms

As previously described, muscle synergies are hypothesised to be patterns of muscle activity used to solve the DOF problem. These patterns are not initially observable from visual inspection of the untransformed data as they exist in a lower data dimension (a simple example of this is to compare a 3-dimensional sphere to a 2-dimensional slice of that sphere. The reduced dimensions of the circle provide a reasonable approximation of the sphere whilst being easier to visualise). Dimensions could be removed from the dataset arbitrarily but this risks discarding much of the data of interest. Instead dimensionality reduction algorithms seek to transform data into a new dimensional space. This new dimensional space is constructed such that variability is concentrated into a smaller set of information dense dimensions. Information theory shows that this dimensionality reduction reflects latent structure in the data, in this case muscle synergies (Lee and Seung, 2000). If these methods are successful, then certain dimensions can be discarded as only containing a small portion of the variability of the original dataset. There are a variety of methods available for synergy extraction and their performance has been previously examined in various contexts (Tresch et al., 2006). However, there remains some disagreement between studies on the most accurate method for various datasets. Four of the most commonly used algorithms are principal component analysis (PCA), independent component analysis (ICA), non-negative matrix factorization (NMF) and factor analysis (FA). The implementation of these methods was examined for speed in terms of calculation time and accuracy in terms of the cosine similarity values between the real and extracted synergies. This accuracy was confirmed using ANOVA and a Tukey multiple comparison test.

2.4.8 Principal component analysis

PCA attempts to concentrate data into a set of orthogonal principal component vectors that explain the majority of variance in that data (Pearson, 1901; Hotelling, 1933). As the majority of the variance is captured within the first few principal components, by only including these components a dimensionality reduction is achieved. Let this dataset be a matrix defined as $\mathbf{X}$ with size $n \times n$ where n is the length of the dataset and p is the number of variables. It is important that the data is centred on a zero mean by subtracting

its mean value from each variable. From this zero-meaned dataset, the covariance matrix $\mathbf{C}$, of $p \times p$ variables are then calculated using equation (6):

$$cov(X,Y) = \frac{1}{n-1}\sum_{i=1}^{n}(X_i - \overline{x}))(Y_i - \overline{y}) \quad (6)$$

Where X and Y are variables within $\mathbf{X}$ and this process is repeated for all p. This matrix is symmetrical and given in matrix notation takes the form:

$$\mathbf{C} = \frac{X^{\intercal}X}{(n-1)}$$

From this the eigenvalues and eigenvectors can be calculated by diagonalizing the matrix giving the form:

$$\mathbf{C} = \mathbf{VLV}$$

Where $\mathbf{V}$ is the matrix of eigenvectors and $\mathbf{L}$ is the matrix of eigenvalues arranged in decreasing order. The eigenvectors are normalized, and this gives orthogonal unit vectors, which can be interpreted as orthogonal axis on a chart. These axes are the principal components which form the new variables that describe the dataset. The choice of the first PCA axis is that which has the minimal total distance between data points and the PCA axis. This is also the axis which captures the maximal variance of the data. This procedure is repeated leading to the descending scale of importance in PCA components seen in $\mathbf{L}$. Additionally, each additional PCA component must be uncorrelated with the previous components, which is equivalent to being orthogonal in the feature space. This process is more efficiently calculated using singular value decomposition of $\mathbf{X}$ from which it can be proven that singular vectors and values are equal or directly related to principal directions and eigenvalues.

2.4.9 Factor analysis

FA has the closest degree of similarity to PCA, although it is approaching the same problem from the opposite direction (Bartholomew et al., 2008). Whereas PCA attempts to describe the observed dataset with a smaller number of “better” variables, FA assumes that these smaller latent variables caused the observed dataset. The output of PCA and FA is often highly similar, so the difference is partially academic, but it influences understanding of how each technique functions. Consider the dataset $\mathbf{X}$ which is made up of individual data points of p variables with each variable having n data points

such that $X_p = \{x_1, x_2, \dots, x_n\}$. Each variable can be described by a combination of m common factors as in equation (7):

$$X_i = a_{i1}F_1 + a_{i2}\,F_2 + \cdots \;\; a_{im}\,F_m + e_i \tag{7}$$

Where F is the common factor, a is known as the factor loading or score and e is a factor specific error term which is the variance that this factor cannot explain. Calculating these factor scores is done in one of two ways, either using the principal component method to account for the greatest variance (in which case the processes become mathematically analogous at this point, although the scores are only proportional to the principal components) or by common factor analysis selecting the least number of factors that can account for the total variance in the set of variables. This is usually followed by factor rotation to aid in data interpretation and to attempt to force closely related subgroups of variables to score highly on just one factor. The choice of rotation method largely relates to whether it is desirable for factors to be correlated or uncorrelated. In this case an orthogonal rotation was chosen for uncorrelated factors for easier comparison with the other synergy analysis techniques.

2.4.10 Independent component analysis

ICA is a blind source separation method which can be used to extract muscle synergies from EMG data (Comon, 1994). Due to its name, and the fact that it is sometimes applied to similar problems, it is sometimes unduly assumed that ICA and PCA are similar in function. Besides attempting to find a set of basis vectors that describe the data, the two techniques have little in common. In PCA the goal is to find basis vectors that capture the most variance (within the other constraints of the algorithm). ICA attempts to find vectors that are statistically independent of one another by maximizing the non-Gaussianity of the vectors selected. In fact, for the purposes of synergy extraction one of the core limitations of ICA is that it is not possible to determine the order or importance of each identified source.

An intuitive understanding of the difference can be illustrated by the cocktail party problem (McDermott, 2009). Imagine a room hosting a cocktail party with multiple conversations being recorded by a set of microphones placed around the room. Each microphone records the sounds from the party made up of the same set of sound sources (the conversations) but receives a different mixture due to their placement in the room. The problem here is to try and isolate and identify the original conversations from the mixtures recorded. PCA is unlikely to extract the original signals unless by chance the

principal components happen to align well along these signals. ICA on the other hand puts greater emphasis on extracting the original sources. The first assumption is that the observed data is made up of statistically independent signals at all time points (an assumption that is, in practice, reasonably robust to violation). It is also assumed that the original sources have non-Gaussian distributions, which is often true for biological signals.

Following these assumptions ICA attempts to solve problems of the class defined by equation (8):

$$\mathbf{X} = \mathbf{AS} \tag{8}$$

Where $\mathbf{X}$ is a vector with size p multivariate input measurements, $\mathbf{S}$ is the original source vector also size p made up of independently distributed variables and $\mathbf{A}$ is the $p \times p$ mixing matrix. For a given dataset of $\mathbf{X}_N$, ICA attempts to estimate both $\mathbf{A}$ and $\mathbf{S}$. For our purposes $\mathbf{A}$ represents the synergy vectors and $\mathbf{S}$ are the activation coefficients. There are a variety of methods for estimating these matrices, here FastICA is used as a method with an excellent balance of computation time, accuracy and robustness to noise. The precise details of FastICA are presented in more detail by Hyvärinen and Oja (2000) but the process involves iteratively updating an initially random weighting for basis vectors until the process converges on an estimated value of non-Gaussianity (Hyvärinen and Oja, 2000).

2.4.11 Non-negative matrix factorization

As in the previous examples NMF attempts to find a reasonable approximation of a larger dataset whilst reducing its overall dimensions. As with ICA, NMF can be applied to blind source separation problems, in that it attempts to find basis vectors that approximate the original pre-mixing signals (Tresch and Bizzi, 1999; Lee and Seung, 2000). NMF's chief advantage compared to other approaches for the purposes of synergy analysis is that the constraint of non-negativity aligns well with muscle activity i.e. muscle activation is never negative. NMF has also previously been shown to be more effective at identifying latent structure in the data when compared to other techniques such as principal component analysis (Ebied et al., 2018).

Consider the matrix $\mathbf{X}$ of size $n \times p$ where n is the length of the dataset and p are the number of variables. In the case of NMF basis vectors are constructed via an iterative algorithm, similar to ICA, but matrix values are constrained to be non-negative and the

objective function varies, most commonly and used here is the Frobenius norm. This class of problem can be defined by equation (9):

$$\mathbf{X} = \mathbf{WC} \tag{9}$$

Such that, $\mathbf{C}$ is an $N \times n$ matrix where N is the chosen NMF rank factor. Each row of $\mathbf{C}$ represents some structure in the time series similar to a PCA component. $\mathbf{W}$ is a $p \times N$ matrix which, when multiplied by $\mathbf{C}$, approximates $\mathbf{X}$. Each column of $\mathbf{W}$ quantifies the amount that the corresponding row in $\mathbf{C}$ contributes to the original data in $\mathbf{X}$ (Lee and Seung, 2000; Donoho and Stodden, 2004; Berry et al., 2007; Torres-Oviedo and Ting, 2007). Each synergy is represented by the corresponding column in $\mathbf{W}$ and row in $\mathbf{C}$. $\mathbf{C}$ is termed the activation pattern of the synergy as it represents some underlying structure of the original EMG time series. $\mathbf{W}$ is referred to as the muscle contribution vector of the synergy as each component value indicates the contribution of the synergy's activation pattern to the associated muscle activity. This naming convention has been used to refer to the equivalent outputs for each extraction algorithm examined.

There are a number of methods for calculating $\mathbf{W}$ and $\mathbf{C}$ but the method used here is an implementation of Lee and Seung's multiplicative update rule (Lee and Seung, 2000). $\mathbf{W}$ and $\mathbf{C}$ are initialized using an SVD approximation of the matrix and then iteratively updated using equation (10) and (11) (Boutsidis and Gallopoulos, 2008):

$$\mathbf{C}_{[i,j]}^{n+1} \leftarrow \mathbf{C}_{[i,j]}^{n} \frac{((\mathbf{W}^{n})^{T}\mathbf{X})_{[i,j]}}{((\mathbf{W}^{n})^{T}\mathbf{W}^{n}\mathbf{C}^{n})_{[i,j]}} \tag{10}$$

$$\mathbf{W}_{[i,j]}^{n+1} \leftarrow \mathbf{W}_{[i,j]}^{n} \frac{(\mathbf{X}(\mathbf{C}^{n+1})^{T}\mathbf{X})_{[i,j]}}{(\mathbf{W}^{n}\mathbf{C}^{n+1}(\mathbf{C}^{n+1})^{T})_{[i,j]}} \tag{11}$$

This is repeated until the Frobenius norm of $\mathbf{W}$ and $\mathbf{C}$ ceases to decrease (within a tolerance range) or a maximum number of runs is reached ($n = 30$).

2.4.12 Selection of rank factor

For the purposes of muscle synergy analysis rank factor is equivalent to the number of synergies selected. It is the number of new dimensions that the data has been reduced to e.g. from 5 EMG dimensions to 2 synergy dimensions means a rank factor of 2. Selection of rank factor is critical to produce dimensionality reduction during synergy extraction. PCA, NMF and FA can be sorted by the variance accounted for (VAF). In these cases, rank factor was chosen consistent with previously literature such that rank

factor was increased to the minimum required to be greater than 90%. VAF was calculated for each synergy profile for both the individual muscle and for all muscles collectively. If VAF was below 90%, the resulting synergies were discarded (Tresch et al., 2006). In ICA this is not possible, and the choice must be made via other methods. In this case it was decided that the number of components for ICA would be chosen to match that agreed upon by the preceding methods as there was no disagreement between them.

2.6 Neuronal Models

Our aim was to create a neural population model such that applying NMF to the firing rate activity of the motor neuron populations would yield the same synergy patterns as those identified in the EMG data. The model does not attempt to reproduce simulated EMG signals. Instead, it was assumed that the cumulative activity of multiple motor units described by the average activity of distinct motor neuron populations would serve as a proxy for EMG. We first considered rate-based models which represent a population metric, for example the average firing rate or oscillation frequency, abstracted from the underlying individual neurons. Rate-based models are suitable for reproducing firing rates in neural circuits, but there is no clear relationship with the state of the underlying neural substrate (Wilson and Cowan, 1972; Kuramoto, 1991). Although not essential for this work, considering detailed modelling with Rybak's group, as well as future requirements for the model, it was desirable to use a technique that retains a closer relationship with the state of spiking neurons that comprise the neural circuit. Population Density Techniques (PDTs) do so: they retain information about the state of neurons in the circuits but calculate population level aggregates directly.

2.6.1 Population Density Techniques

PDTs model neural circuits in terms of homogeneous populations of neurons. The individual neurons are described by a model, such as the leaky-integrate-and-fire model. The model of an individual neuron is characterised by a so-called state space: the values that determine the state of individual spiking neurons. For a simple neuron model this can be its membrane potential. More complex models represent the state of other elements such as synapses. PDTs represent a population by a single density function that represents how neurons are distributed across the neuron's state space.

2.6.2 MIIND

MIIND is a neural simulator which implements a version of a PDT to simulate multiple interacting populations of neurons (de Kamps et al., 2008; Marc, 2011). It can provide a visual representation of the probability density function by displaying the density during simulation. Figure 3-L shows an example of this visual representation. A network of populations can be built in MIIND using a simple XML style code format to list the individual populations and the connections between them. Populations in the network interact via their average firing rates, which are assumed to be Poisson distributed spike trains. For each connection, the firing rate of the source population becomes the average rate of the Poisson distributed input spikes to the destination population. The connections defined in the XML code, have three parameters: the post synaptic potential or instantaneous synaptic efficacy, the number of individual connections between source neurons and target neurons, and a delay which can be used to approximate time taken for spike propagation and synapse transmission. The MIIND modelling framework was developed by Hugh Osborne and Marc de Kamps.

2.6.3 The Spinal Circuit Model

MIIND was used to build a network of populations of exponential integrate and fire (EIF) neurons according to the connectivity diagram in Figure 2-A. Table 2-A shows the connection parameters for all populations in the model. All populations use the same underlying neuron model as described in equation (12):

$$\tau \frac{dv}{dt} = (v - v_{rest}) + \Delta_T e^{\frac{v - v_{thres}}{\Delta_T}} \tag{12}$$

Where v is the membrane potential, v_{rest} = −70 mV, Δ_T = 1.48, v_{thres}= −56 mV, and τ = 3.3 ms. These parameters were chosen such that populations could produce a wide range of average firing rates between 0 and 200 Hz to exhibit typical neuronal frequencies. An EIF model was chosen in contrast to the more commonly used Hodgkin Huxley style neurons. This is because the objective was not to reproduce the EMG signals exactly, but to provide a concise explanation for overall synergy patterns. It is expected that any particular description of activation of ion channels (as in a Hodgkin Huxley style model) would have no significant impact on the population level activity or synergy patterns in this task and would therefore dilute the power of the model. The main structure of the network consists of two neural populations, named “Extensor

Interneurons" and "Flexor Interneurons", connected together in a network with five motor neuron populations, one for each muscle. The Extensor and Flexor Interneuron populations represent combinations of excitatory and inhibitory neurons and therefore can project both kinds of connections to other populations in the network. Other studies have previously described the connection motif of agonist inhibition with antagonist excitation and this is utilised here to connect the interneuron and motor neuron populations to elicit the agonist/antagonist relationship between the five muscles (Sherrington, 1909; Doss and Karpovich, 1965; Bigland-Ritchie, 1981; Pierrot-Deseilligny and Burke, 2005). These features, including the mutual inhibition between the two interneuron populations, also appear in the McCrea and Rybak CPG model (McCrea and Rybak, 2008). Although rhythm and pattern formation are not included in this model, the implications for applying a CPG model to an isometric task are discussed later.

All supraspinal activity comes from the Cortical Drive input and is responsible for the "contraction". There is a direct connection to the MN-RF motor neuron population indicative of the muscle which is being maximally contracted in this task. Cortical Drive also projects to the Extensor and Flexor Interneuron populations. As there are more excitatory than inhibitory connections from the Extensor and Flexor Interneuron populations to the motor neuron populations, the Cortical Drive indirectly causes excitation of all motor neuron populations as well as MN-RF. During the simulation, the input to the two interneuron populations begins at 0Hz before increasing to 260Hz over 1 second, then five seconds later, dropping back to 0Hz over 1 second.

It was hypothesised that the most important factor in shaping the observed synergies would be the connectivity of the network model and that they could be modulated with a proprioceptive input. To simulate changes in proprioceptive feedback due to the knee angle, the Extensor Afferent Feedback input to the Extensor Interneuron population was introduced and for different trials was altered between 110Hz and 180Hz. The Flexor Afferent Feedback input was held constant. The average firing rate of each of the five motor neuron populations was recorded at a rate of 10 KHz (corresponding to the 0.1ms time step of the simulation) then sampled at 2ms intervals. NMF was performed on the resultant time series as described for the experimental recordings.

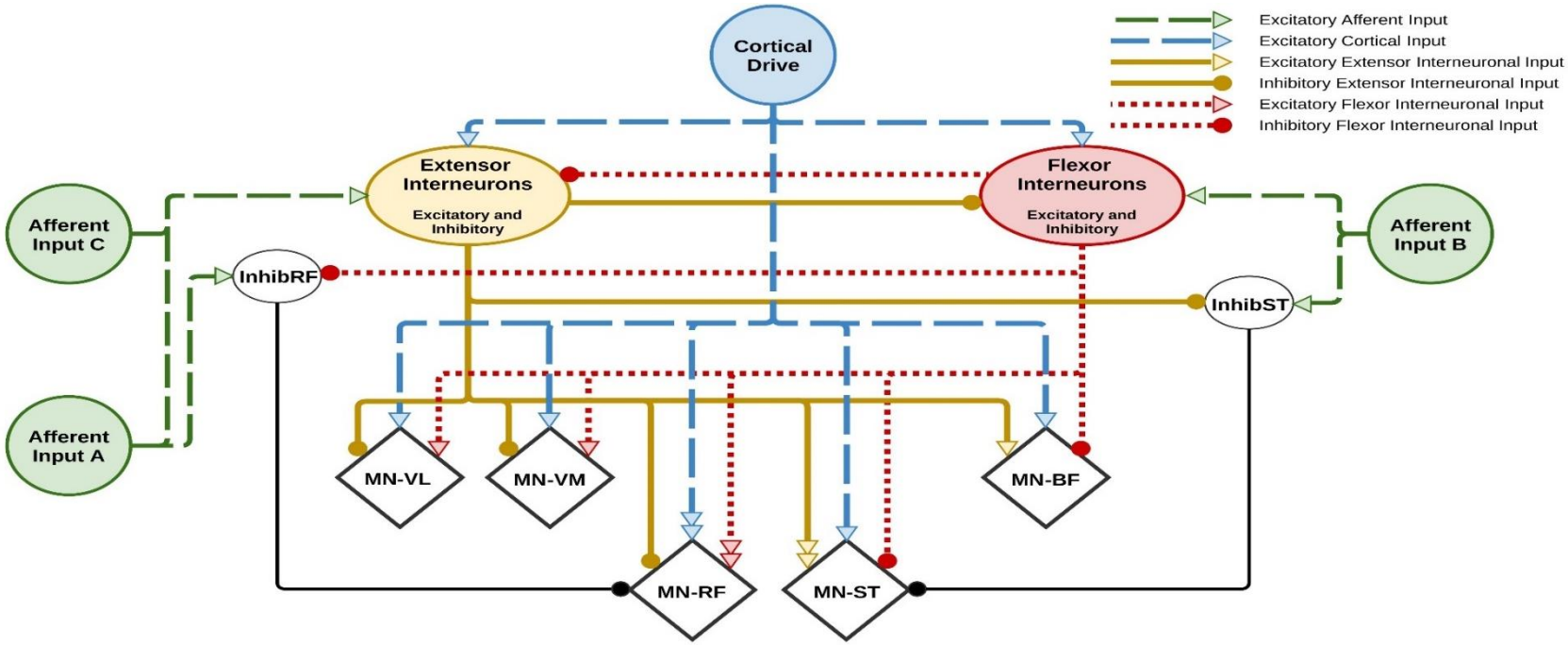

Figure 2-A: **Schematic of connections between simulated spinal populations**. MN-VL (Vastus Lateralis), MN-VM (Vastus Medialis), MN-RF (Rectus Femoris), MN-ST (Semitendinosus) and MN-BF (Biceps Femoris) motor neuron populations are identified as diamonds although all populations consist of EIF neurons. The Extensor and Flexor Interneuron populations allow both outgoing excitatory and inhibitory connections. All populations receive a background level of input producing a baseline activity. Parameters for the network connectivity are provided in Table 1-A. MN-RF and MN-ST receive much higher excitation from the interneuron populations than the other motor neuron populations (indicated as a double arrow). The InhibRF and InhibST populations are used to offset the level of bias given to the MN-RF and MN-ST populations. Afferent Input A and B control the balance of input to the Flexor and Extensor Interneuron populations respectively which influences the agonist/antagonist bias in synergy 2. Afferent Input C represents an additional input activated at the limit of extension to provide a strong inhibition (via inhibitory Extensor Interneurons) to the agonist motor neuron populations. Connections that exist in other models, but which are not required to produce the observed synergies have been omitted. For example, direct afferent inputs to motor neuron populations. The relative strengths of each connection are also not shown (with the exception of MN-RF and MN-ST) but can be found in the connectivity parameters (Table 1-A). Network designed and coded by Hugh Osborne.

Population name	Source population name	Post synaptic delta efficacy (mV)	Average number of incoming connections to each neuron	Connection delay time (ms)	Average firing rate where defined (Hz)
MN-RF	Extensor Interneurons	-0.052	35	2	
MN-VL	Extensor Interneurons	-0.052	35	2	
MN-VM	Extensor Interneurons	-0.052	35	2	
MN-ST	Extensor Interneurons	-0.052	140	2	
MN-BF	Extensor Interneurons	-0.052	70	2	
MN-RF	Flexor interneurons	-0.052	140	2	
MN-VL	Flexor interneurons	-0.052	70	2	
MN-VM	Flexor interneurons	-0.052	70	2	
MN-ST	Flexor interneurons	-0.052	35	2	
MN-BF	Flexor interneurons	-0.052	35	2	
MN-RF	InhibRF	-0.052	70	2	
MN-ST	InhibST	-0.052	70	2	
InhibST	Extensor interneurons	-0.052	70	2	
InhibRF	Flexor interneurons	-0.052	70	2	
Extensor interneurons	Flexor interneurons	-0.052	35	2	
Flexor interneurons	Extensor interneurons	-0.052	35	2	
Extensor interneurons	Background	0.1	100	0	400
Flexor interneurons	Background	0.1	100	0	400
InhibST	Background	0.1	100		400
InhibRF	Background	0.1	100	0	300
MN-RF	Background	0.1	100	0	300
MN-VL	Background	0.1	100	0	300
MN-VM	Background	0.1	100	0	300
MN-ST	Background	0.1	100	0	300
MN-BF	Background	0.1	100	0	300
MN-RF	Cortical drive	0.1	100	0	45*
MN-VL	Cortical drive	0.1	100	0	20
MN-VM	Cortical drive	0.1	100	0	20
MN-ST	Cortical drive	0.1	100	0	20
MN-BF	Cortical drive	0.1	100	0	20
Extensor interneurons	Cortical drive	0.1	100	0	60
Flexor interneurons	Cortical drive	0.1	100	0	60
Extensor interneurons	Extensor afferent input	0.1	100	0	110 to 180**
Flexor interneurons	Flexor afferent input	0.1	100	0	90
InhibST	Extensor afferent input	0.1	100	0	110
InhibRF	Flexor afferent input	0.1	100	0	10

* During the task, Cortical Input transitions from 0Hz to these values back to 0Hz

** Afferent input remains constant throughout the activity but is set between 110Hz and 180Hz to produce different synergy patterns.

Table 2-A: Parameters relevant to each connection between populations and from inputs in the model. Values for input activity are provided in the form of an average firing rate.

Finally, the network was augmented (The greyed area of Figure 2-A) to generate a knee flexor bias for RF and an extensor bias for ST which was observed in the experimental results. An additional excitatory connection was added to the model from the Extensor Interneuron population to MN-ST, and from the Flexor Interneuron population to MN-RF. This is equivalent to increasing the number of excitatory connections overall between those populations. In order to modulate the effect of afferent feedback input on these connections, two additional populations of inhibitory neurons were added to the model: InhibST and InhibRF. This network motif of an additional excitatory drive coupled with a controllable inhibitory input has previously been used to reproduce observed activity in Semitendionsus and Rectus Femoris of a cat and further supports the use of CPG models for human studies (Shevtsova et al., 2016).

In the experiment task, two positions were used to identify the effect of passive insufficiency on the synergies recruited. It was expected that the contralateral hip position would serve only to influence the degree of muscle stretch which in the model would already be accounted for in the activity of the afferent feedback input. There is, therefore, no analogue to hip position defined in the model.

2.7 Machine learning models “fuzzy” non-linear relationships

For FES, many devices use *a posteriori* information to determine how stimulation should be delivered e.g. if stimulus at a site results in extension of the limb, that site is now always used for extension. This approach does not attempt to understand how stimulation produces movement and only constitutes a very simple transfer function between input and output. Specific control of individual EMGs requires algorithms with a greater degree of control over stimulation parameters than what is currently available. Determining how electrical stimulation at a set of given points relates to electrical activity at another point (in the form of EMG’s) is a multidimensional problem with a high degree of variability between participants and different stimulation sites. A truly general transfer function would allow for translation across all this variability; however, this is difficult to achieve due to the increasing complexity of the functions shape as specificity decreases. Stimulation at the periphery is more specific than the spinal cord, which is more so again than at the cortex, and the complexity of individual control of a given muscle becomes more problematic. No such algorithm currently exists, even in the periphery, which the algorithms developed in this section aims to address. The algorithms here was used to

control stimulation of the rat hindlimb at the level of the peripheral nerve for the purposes of recruiting specified EMG waveforms.

2.7.1 Surgical Procedure

To collect the training dataset for the ANN the sciatic and tibial nerves were stimulated with a large stimulation paradigm of mixed pulse width and voltages. A schematic representation of the surgical preparation is shown in Figure 2-B (figure adapted from Smith et al., 2018). Each rat was induced with a mixture of ketamine and xylazine (10:1) delivered intraperitoneally and was maintained with a mixture of ketamine and saline (1:1) delivered via carotid cannula. Proper anaesthetic plane was tested throughout surgery via the toe pinch method. Normal body temperature was maintained (37±1°C) via a thermometer-controlled heat blanket and heat lamp. Following the loss of paw withdrawal, the right ventral hindlimb was exposed and an incision made lateral to the femur. The sciatic nerve was exposed via blunt dissection proximal to the bifurcation into tibial and peroneal nerves and the cuff attached at this point. In a subset of animals a second cuff was also attached to the tibial nerve below the branch point. This was not repeated in all animals due to the significant increase in time required to provide the much larger stimulation paradigm required for stimulus across multiple sites. In all cases the cuff was aligned lateral to the nerve, such that the stimulating wires within were parallel to the nerve path. Cuffs were not sutured to avoid nerve compression and the surgical site was kept moist with a non-conductive mineral oil. Test pulses were delivered to ensure proper placement of the cuff. The Achilles tendon was then dissected and attached to an ergometer via metal rings sutured into the end point. A pair of insulated fine copper wires (40 AWG; 79 µm in diameter) with 1.5- to 2-mm bared tips were inserted in pairs into LG, MG, EDL, EHP and TA using a hypodermic needle (27 G). Test pulses were again delivered to ensure placement of recording electrodes was correct. The surgical site was then closed via a haemostat to prevent drying and to better simulate *in vivo* conditions and joint position. Optimal response length was determined experimentally in one animal by altering the length of the muscle, measured via Microdrive on the stereotaxic setup.

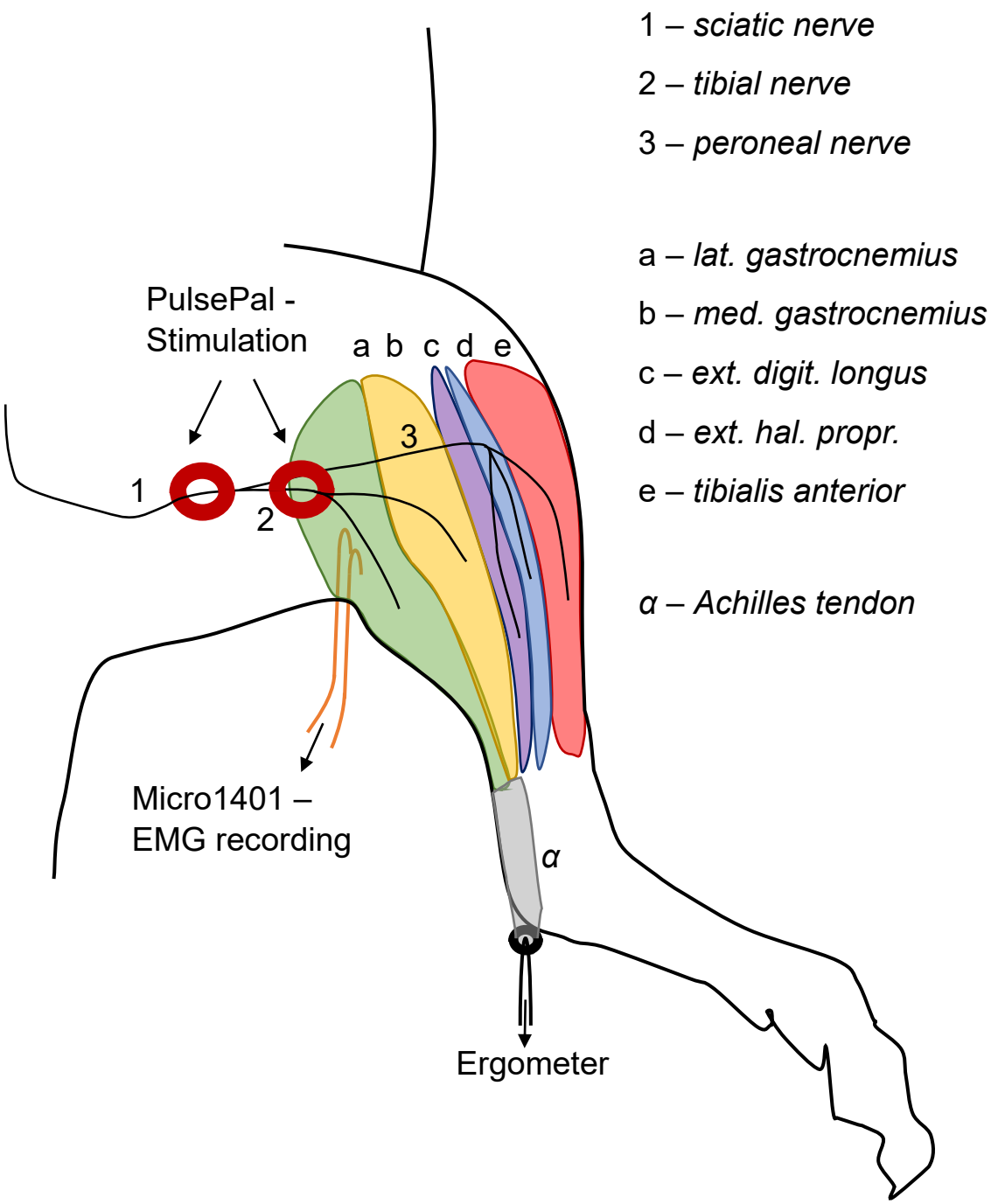

Figure 2-B: Surgical preparation for stimulation of the sciatic and tibial nerves. The sciatic nerve (1) branches into the tibial (2) and common peroneal (3) nerves. The peroneal nerve goes on to become the deep fibular nerve (The depiction of nerve anatomy shown here is limited to nerves relevant to the experiment). The sciatic and tibial nerves were exposed and stimulating cuffs were attached (red circles). EMG recordings were taken from medial and lateral gastrocnemius (*a*,*b),* extensor digitorum longus (*c*), extensor hallucis proprius (*d*) and tibialis anterior (*e*) via a pair of copper hook electrodes inserted into the muscle belly. (Only a single pair is shown here for clarity). Force recordings were made using an ergometer attached to a metal ring sutured into the Achilles tendon. Adapted from Smith et al., 2018.

2.7.2 Data collection

EMG recordings were made from 4 muscles of the rat hindlimb; extensor digitorum longus (EDL), extensor hallucis proprius (EHP) medial and lateral gastrocnemius (MG, LG) and tibialis anterior (TA). TA signals were discarded from all rats due to poor signal quality. Force recordings were made via an ergometer attached to the Achilles tendon. Although recordings were made from 8 animals, it was not possible to get high quality responses from every muscle in any animal. Details on the number of recorded muscles from each animal, the threshold potential and how the stimulus range compared to this threshold, and an estimate of the rheobase for each animal are shown in table 2-B. The threshold value was calculated as the voltage at which the minimum pulse width (100 µs) generated a response. Rheobase was estimated as the largest width signal (2000 µs) with the smallest voltage that generated a response. This value does not reflect the true rheobase as the pulse widths used here are not sufficiently long to approximate infinite pulse width. However, for the stimulation dataset recorded this still provides insight into the electrophysiological properties of the nerve. Data was sampled at 10Khz using a CED micro 1401 data acquisition interface and Spike8 recording software [Cambridge Electronic Design (CED), Cambridge, United Kingdom]. Electrodes were placed within the central mass of the muscle belly.

2.7.3 Stimulation Protocol:

Stimulation was provided via a handmade multistrand stainless-steel wire in a flexible epoxy cuff using the Sanworks PulsePal isolated stimulator via a custom written Python program. Stimulus pulses were balanced biphasic square pulses with variable width (100-2000 µs increments of 100 µs) and voltage (100-2000mV in increments of 100mV). The range of stimulus parameters was selected to cover both minimal i.e. no response and maximal response within the resolution of the PulsePal device. The saturation point for the muscles under examination was determined through exploratory stimulation. This process involved manually adjusting stimulus voltage and width until the measured response ceased to increase in peak to peak amplitude. This was repeated in each animal at the start of recording and it was determined that across animals' saturation occurs at approximately 2V and 2000µs, so this was determined to be the maximum values for the stimulation paradigm.

These parameters create a stimulus paradigm of 400 pulses. Additionally, test pulses were delivered as the first, last and every hundredth pulse leading to a total of 404 pulses

in each stimulation paradigm. Test pulses were also balanced biphasic square pulses with a fixed width and voltage (200 µs - 5000mV). To avoid inducing fatigue or other changes in excitability of the nerve, pulses were separated by 3s. In those animals where a second cuff was attached to the tibial nerve stimulation was provided to each cuff separately as well stimulating both cuffs at the same time. When stimulus was provided to both cuffs the stimulation parameters were kept the same for each cuff.

2.7.4 Data pre-processing and artificial neural network design

After collection, signals were segmented to remove signal artefact from a predefined point following stimulus delivery synched with the PulsePal device. For training purposes four parameters were extracted from the EMG signals; max amplitude, RMS, waveform length and SampEn. Combinations of these values have been shown to result in a high degree of waveform separation (Phinyomark et al., 2013). This training dataset and the matching stimulation parameters were then shuffled to avoid bias from ordering. Data was split into training and validation datasets in a 3:1 ratio. Network layers consist of an input layer size corresponding to the EMG parameters for each muscle (or motor neuron output when applied to the MIIND network), two hidden layers one of 2000 $\tanh$ and another of 2000 leaky rectified linear units (leaky ReLu), and finally a linear output layer of size 2 (corresponding to the stimulation parameters of pulse voltage and width). This network was trained using the mean squared error as its loss function and an adaptive gradient optimizer (initial learning rate = 0.05). Training occurred for 6000 epochs or until validation accuracy ceased to improve for 50 epochs. The network accuracy was reported and then for illustration purposes the network was asked to predict the training dataset. This process was repeated with the dataset restricted to just 7 of the recorded animals and the network was then asked to predict the dataset for the now unseen 8th animal. A full description of the mathematics involved in tensor calculation is beyond the scope of this thesis, but full documentation of the methods used here are available at: https://keras.io/ and https://www.tensorflow.org/.

Animal ID	Muscles Recorded	Muscles with clear signal	Ergometer recording	Threshold value per muscle	Stimulus range	Estimated Rheobase	Tibial Stimulation
1	LG, MG	LG	✕	700mV	T-3T	300mV	✔
2	LG, MG	LG, MG	✕	400mV	T-3.5T	700mV	✔
3	EDL, EHP	None	✔	N/A	N/A	N/A	✕
4	EDL, EHP	EDL, EHP	✕	600mV EDL 500mV EHP	T-5T	500mV	✕
5	LG, MG	None	✔	1300mV - based on ERG response	N/A	N/A	✕
6	LG, MG	LG, MG	✔	1300mV	T-1.3T	800mV	✕
7	EDL, EHP	EDL, EHP	✕	100mV	T-20T	100mV	✕
8	EDL, TA	EDL, TA	✕	100mV	T-20T	100mV	✕
	Total						
	LG	3	2				
	MG	2	2				
	EDL	2	1				
	EHP	2	1				
	TA	1	0				

Table 2-B: Summary of results measured per animal. Column two records the muscles from which the signal was recorded. Column three records which of these recordings were deemed of sufficient quality for further analysis. Indicated in column 4 are the animals from which ergometer recordings were collected. Column 5 records the value at which the shortest stimulus pulse (100 µs) generated a response via the sciatic cuff. This was deemed the threshold value and was calculated for each muscle in the recording and is listed separately when this value differs between muscles. From this value the stimulus range was calculated in terms of the maximum voltage within the stimulus paradigm. The rheobase of each nerve was estimated as the smallest voltage that the longest stimulus pulse (2000 µs) elicited a response. Tibial stimulation indicates in which animals' tibial stimulation was attempted. Provided below this are the total number of recordings for each muscle separated into EMG and ergometer recordings.

2.8 Closed loop control and MIIND injury modelling

The algorithmic implementation developed here was designed to test the ability of the previously described algorithms to restore healthy muscle synergies in an *in silico* model. In contrast to the implementation shown here, closed loop controllers in BMI devices rarely incorporate motor output into the stimulation provided. This moves closer towards true closed loop control by incorporating the produced synergies into future stimulation signals. The MIIND network previously described in Section 2.6 was used as a basis for modelling both healthy and injured states. Simulations have a direct advantage over biological experiments as they have access to the ground truth when extracting information from the system. This allows precise error measurement and comparison to biological models. Stimulation was provided at selected sites in the interneuron network and the motor neuron output measured. This formed the dataset to train the same ANN described in Section 2.7, so this also provided an opportunity to further test the generalizability of the algorithm to a new stimulation environment.

2.8.2 Network injury models

The previously established MIIND network was used as an example of a healthy interneuron network. Two different injury types were targeted for modelling, cortical and peripheral injury, and different degrees of injury of total or partial loss of connecting neurons. The location of these injuries is shown in Figure 2-C. Cortical injury was modelled by removal of descending input to either the extensor or flexor interneuron pools or both, simulating an injury to the spinal cord or to the cortex itself as in stroke. This leaves the afferent feedback, and inhibitory links between interneuron pools intact but removes descending control. Peripheral injury was modelled by the removal of afferent input to interneuron pools and was similarly replicated in unilateral and bilateral injuries.

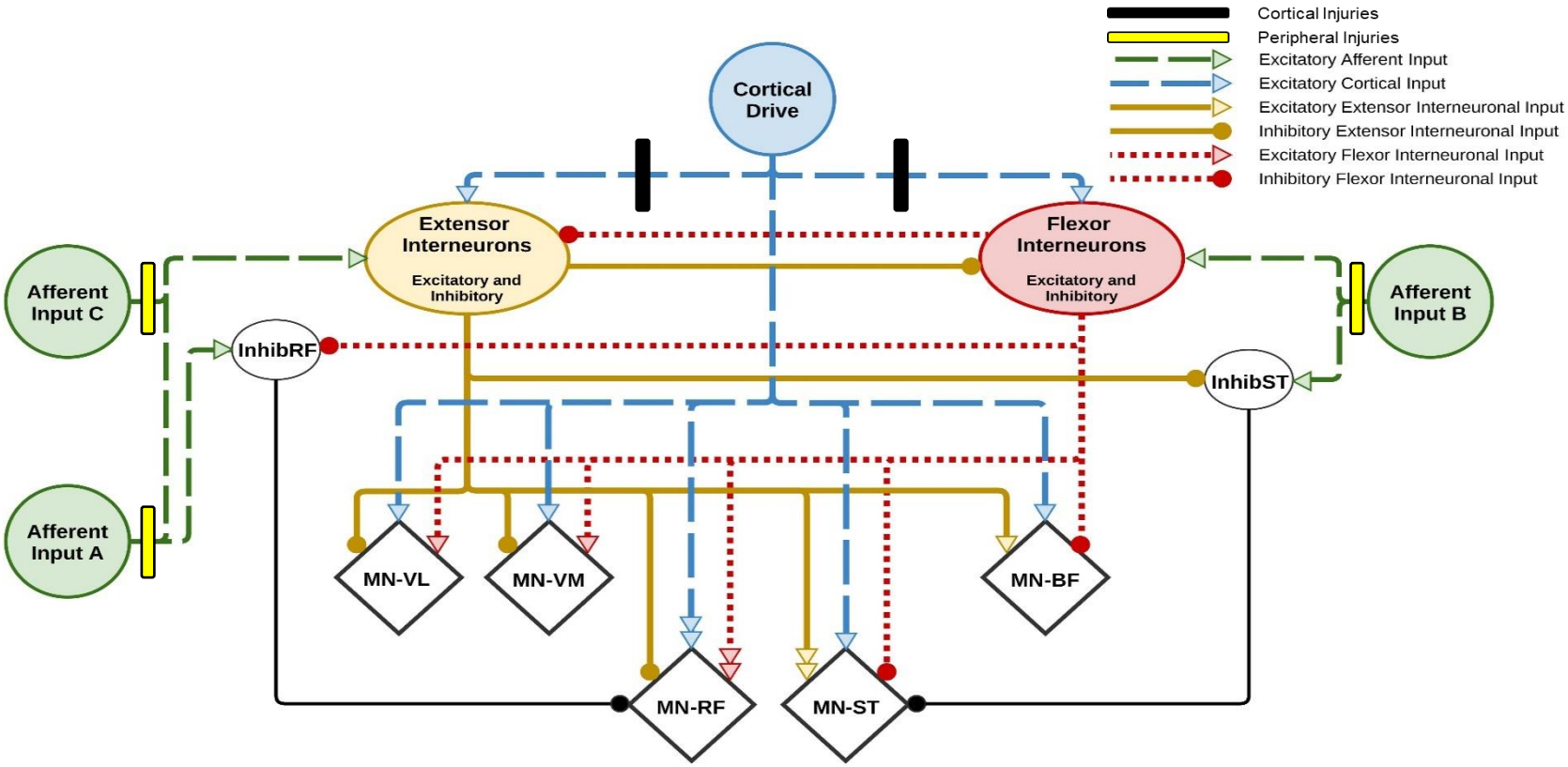

Figure 2-C: **Removed or reduced connections between simulated interneuron populations to recreate different injuries to the nervous system**. Alterations were made to connections between populations within a simulated model of interneurons controlling muscles of the upper leg to recreate injuries in different parts of the nervous system. Total and partial injuries were considered by either removing or halving connections between nodes of the network. Injury location was divided into cortical or peripheral injuries indicated by the rectangular bars (BLACK, YELLOW). Injuries were further subdivided into unilateral or bilateral injuries. MN-VL (Vastus Lateralis), MN-VM (Vastus Medialis), MN-RF (Rectus Femoris), MN-ST (Semitendinosus) and MN-BF (Biceps Femoris) motor neuron populations are identified as diamonds although all populations consist of EIF neurons. Model parameters are shared with figure 2-A and are provided in Table 1-A.

2.8.3 Reconstruction of healthy synergies using an ANN

After simulation of the different injury types, synergies were extracted using NMF from the resulting motor neuron outputs as previously described. These synergies were then compared to the healthy output directly where possible, however as previously described synergies were selected to account for 90% VAF which can lead to differing ranks of synergy extracted. The MIIND network can simulate electrical stimulation at multiple points in the form of an incoming excitatory connection. Whilst it would be possible within the simulation, stimulation was restricted to excitatory stimulation as electrical inhibition via FES is not well established and remains difficult to implement (Damiano et al., 2013; Avendaño-Coy et al., 2017; Kim et al., 2018) Different sets of stimulation parameters were fed into different points of the network dependent on the injury type. For cortical injuries, interneuron pools for the injured site were targeted for stimulation. In peripheral injuries stimulation at these sites makes less sense (particularly in the case of total loss of connections from the injured pool) and therefore motor neurons were stimulated individually. This abstracts the response of a real network wherein precise targeting of each motor neuron is not possible. However, as is shown in Chapter 4 it is in principle possible to selectively recruit a subset of EMG output from a given stimulation point. The same network architecture described in Chapter 4 was then trained on the stimulation and EMG parameters extracted from the injured MIIND network. From the predictions of this network it is possible to predict the required stimulation to generate the healthy EMG variables that produce the healthy synergies. These stimulation parameters were then fed back into the simulation and compared to the healthy network output.

Chapter 3: Online real time synergy analysis – proprioceptive feedback and isometric knee extension

3.1 Abstract

Muscle synergies are hypothesized to be a solution for simplifying the DOF problem in motor control. The methods for extracting muscle synergies are grouped together as dimensionality reduction algorithms, and the effectiveness has been previously shown to differ between datasets. To perform synergy analysis, it is also first required to define the muscle activity of interest. This is usually performed via visual inspection, but automated methods also exist. The performance in terms of speed and accuracy of various onset/offset detection algorithms was compared on their own, and in combination with dimensionality reduction algorithms on a synthetic dataset. From this the most accurate of these algorithms, NMF, was used to investigate the role of proprioception in control of muscle synergy recruitment. Proprioceptive feedback and its role in control of isometric tasks is often overlooked. In this study recordings were taken from the upper leg muscles during an isometric knee extension task where the knee was fixed at different angles, limiting afferent feedback to proprioceptive sources. Subjects were asked to voluntarily activate their rectus femoris muscle for four different internal knee angles and for two different positions of the contralateral leg. Muscle synergy analysis was used to identify canonical temporal patterns in the data. The second muscle synergy showed a collection of patterns at differing angles and positions suggesting the integration of functionally separate afferent signals into muscle activity. The MIIND neural simulation platform was used to develop a spinal population model capturing the combined activity of motor neuron populations for each of the five muscles. The model, based on current understanding of neuromuscular activity in cats includes, for the first time in a human study, separate inhibitory interneuron populations controlling the bifunctional rectus femoris and semitendinosus. When applying the same synergy analysis to the output activity from the model, it was possible to qualitatively reproduce similar muscle synergy patterns and from there deduce three functionally separate afferent signals responsible for the variation in the second synergy.

3.2 Introduction

Execution of a motor task is considered to be modular in nature and is modified by sensory inputs from the periphery and descending input from the brain. This modular

nature has been given many names, but the field has now largely agreed upon the term muscle synergies. A similar consensus has not been reached on the methods for identifying muscle synergies, although NMF and ICA are becoming more dominant in terms of popularity, the effectiveness of different algorithms varies between studies. In order to understand which method and its implementation would be most accurate for our purposes it is necessary to compare these different methods.

The role of proprioceptive feedback in the recruitment of muscle fibres to counter load experienced during a given task is well studied. However, its role in control of interactions between muscles during isometric tasks is still poorly understood. The effect of proprioceptive feedback in models of central motor control is controversial and is thought to be only marginally involved in isometric tasks, especially if static and at a single joint. A previous report on activation patterns in muscles of the upper arm during an isometric task showed no change when arm position was altered (Roh et al., 2012). Furthermore, a study of muscles in the hindlimb of a cat during a balance task showed an invariance to starting position (Torres-Oviedo et al., 2006). However, in this chapter, evidence will be presented for the opposing view and a mechanism is proposed for a role of proprioception in the recruitment of muscles during an isometric task.

3.2.1 Current understanding of synergy recruitment does not adequately explain the role of afferent feedback

There is great variation in the way a motor task can be performed, even at a single joint. Each variation is produced from a combination of muscle recruitment patterns, often described in terms of time. These patterns are commonly referred to as muscle synergies. Their use by the CNS to alleviate the DOF problem is accepted but little is known about the mechanism of their recruitment (Grillner, 1985; Bizzi et al., 1991; Tresch et al., 2002). Similar synergies are reported across species, especially for routine repetitive tasks like locomotion in vertebrates where antagonistic pairs are recruited at and across joints to generate a coordinated alternating pattern of activity (Dominici et al., 2011; Yang et al., 2019). Although not all neurons associated with this recruitment pattern have been identified, their functional grouping into populations within the spinal cord is undisputed, as is their ability to produce all locomotor output patterns observed under fictive conditions (Martin et al., 2007). The current accepted model for control of locomotion is a three layered CPG (McCrea and Rybak, 2008; Rybak et al., 2015). In descending order, the three layers of this model rhythm generation, pattern formation

and the motor neurons themselves. These descending layers interact with and control the next layer or produce motor output in the case of the motor neurons. Although this model can reproduce the rhythm, pattern and output from motor neurones during locomotion the component parts of this network model have rarely been applied to human activity (Markin et al., 2012; Shevtsova et al., 2016).

In this study, the experimental data reported clearly shows an influence of proprioceptive feedback on the structure of observed synergies. Based on this experimental data a model for isometric tasks in humans was created that uses key elements of the model proposed by Rybak et al (Rybak et al., 2015).This model is described at the level of populations of neurons and is simulated using population density techniques (PDTs) which have been shown to accurately model population aggregates (like firing rates) while retaining a close correspondence to spiking neurons - more so than neural mass models - without producing the overhead of simulating thousands of neurons (de Kamps et al., 2019).

3.2.2 MIIND is a model of spiking neurons that efficiently models populations

In this study, for the first time in humans, it was possible to reproduce experimental outcomes using a model of the CPG during a simple isometric task. This finding suggests that the architecture of the model is possibly suited to reproduce the output of vertebrate locomotor CPGs, even if recorded as muscle firing and not neurograms as in fictive locomotor studies. The appropriateness of population models for investigating motor function is further demonstrated here. The neural simulation software package, MIIND, is introduced as a tool for easily prototyping and developing such population models and producing theoretical activity output which aids in clear understanding of the functional effect of model features (de Kamps et al., 2008; de Kamps et al., 2019).

MIIND is a software implementation of a method for simulating populations of neurons using PDTs. Instead of directly simulating a finite population of neurons, PDTs instead consider a probability density function (PDF) which describes the probability of finding a neuron with a certain membrane potential or other state variable in the population. As well as providing a computationally efficient method for simulation, the major benefit of PDTs is that they can be used to calculate a theoretical average firing rate for the population (as well as other metrics such as average membrane potential). This eliminates the need for sampling, binning and smoothing techniques required with more traditional methods of direct simulation. Because PDTs are still based on the model

definition of the underlying neurons, the output activity remains linked to cell structure and while other techniques can often rely on poorly justified assumptions regarding the sources of variability (noise) in the population, PDTs isolate this assumption to the type of distribution of random input spikes. MIIND by default assumes the input to be Poisson distributed and provides a software environment for simulating the interaction of multiple populations via their Poisson distributed average firing rates. MIIND's specific PDT implementation is agnostic to the underlying neuron model and produces a visual representation of the probability density function which makes building networks flexible and provides an insight into the state of each population. MIIND is particularly well suited to situations with known populations of neurons as the source of observed behaviour but the observations themselves (such as EMG) are cumulative and indirect measures of neural activity.

3.2.3 Experimental rationale

Establishing the effectiveness of onset/offset detection is more than simply a matter of comparing the results to visual inspection. Hyperparameters such as how the data is segmented or filtered before passing through the algorithm can affect performance for different methods differently. These variables were kept consistent across testing conditions to give each method a level playing field. As visual inspection is held as the gold standard within the field it is reasonable to compare performance between algorithms by eye. Performing this comparison suggests that costly computational cost to SampEn calculation may not be as useful as previously suggested. Comparing dimensionality reduction algorithms requires a ground truth to measure results against. Therefore, the first step required a method for synthetic synergy generation to provide this ground truth (Tresch and Cheung, 2006). The performance of the most commonly used synergy extraction algorithms was then compared across different noise conditions, differing levels of aberrant spiking activity, and in combination with onset/offset detection. The results from these comparisons agree with previous findings about the effectiveness of NMF but highlights how in certain circumstances ICA may be more effective.

To investigate the effect of afferent feedback on muscle synergy recruitment, we examined the change in interactions among a group of selected muscles, at fixed knee joint angles during an isometric knee extension. The interactions between homonymous and heteronymous muscles are well known but rarely examined in the same isometric task (Pierrot-Deseilligny and Burke, 2005). Recordings were made from seven muscles

in healthy young subjects while they performed an isometric knee extension focusing on voluntarily activating the rectus femoris muscle of the quadriceps. It was hypothesised that this would result in the same synergies being recruited at all angles of the task and that changes in the recruitment pattern of these synergies would reflect alterations to the synergy (as opposed to recruitment of new synergies) due to static proprioceptive feedback from muscle stretch. Observed changes to the recruitment of the quadriceps and hamstrings, in combination with our model, suggest that afferent feedback does affect the recruitment of muscle synergies during an isometric task. This clearly demonstrates that assumptions regarding proprioceptive feedback in motor control have not been sufficiently investigated.

3.3 Results

3.3.1 A moving average window accounts for aberrant spiking activity

The accuracy and speed of different thresholding methods for detecting EMG onset is shown in Figure 3-A. Accuracy here is defined as the ability to detect the onset/offset of muscle activity of interest. An accurate measure will identify the activity and exclude noise. In this example of high SNR activity without spiking activity all measures perform similarly, determining the onset of activity as closely as possible within the limits of the sliding window. Of the three methods examined both average amplitude and RMS were nearly instantaneous, whereas SampEn averaged at 0.59s for calculation time. Figure 3-B shows the accuracy of each measure in the presence of aberrant spiking. In this case average amplitude and SampEn identify the activity of interest under all spiking conditions whereas RMS becomes inaccurate selecting the entire signal as activity of interest. This contrasts with findings in the literature which states that SampEn should be superior under these conditions. Figure 3-C shows the changes that occur when SNR ratio decreases in combination with aberrant spiking. Under low noise conditions each algorithm is approximately as accurate as each other as seen in the left most column As SNR decreases RMS is the first to show signs of decreasing accuracy, as seen in the middle column, whereas both average amplitude and SampEn only starts to decrease in accuracy until the very low SNR ratio condition in the right hand column, wherein each measure begins to incorrectly identify some spikes as activity of interest. Figure 3-D demonstrates the effects of standard filtering regimes on each of the onset algorithms. It is apparent that each algorithm's performance is degraded by the presence of normal filtering methods, RMS and the average amplitude measure begin to incorrectly identify

spikes as activity under the medium noise condition where previously using the average amplitude this did not occur until the very low SNR condition. SampEn is particularly badly affected, and incorrectly identifies spikes as activity even under the high SNR condition.

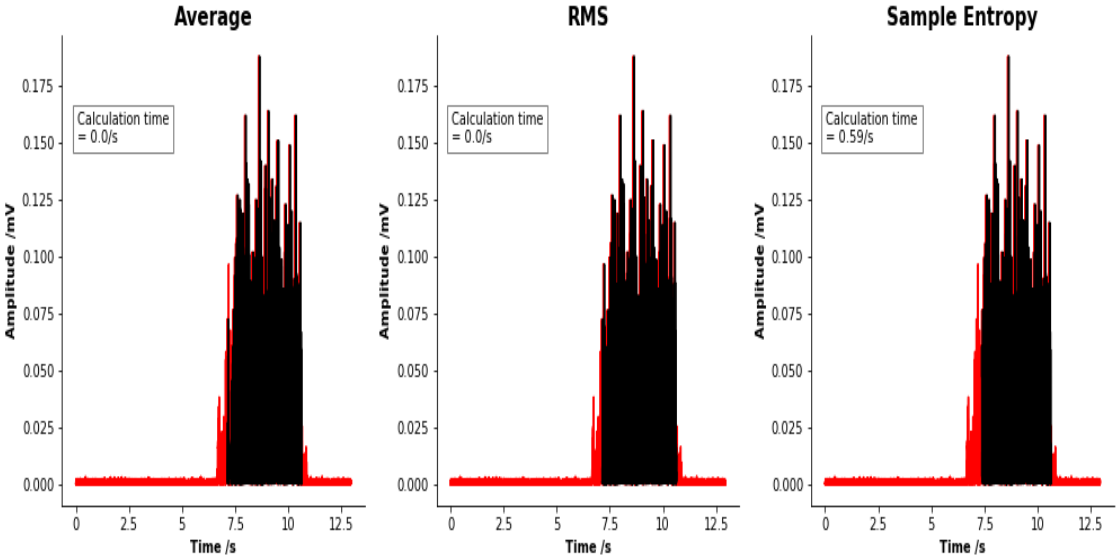

Figure 3-A: **Comparison of accuracy and calculation speed of three algorithms for detection of onset of muscle activity.** EMG signal is recorded from rectus femoris muscle via surface electrodes during an isometric knee extension (red). The identified activity for each algorithm is shown overlaid on top of the muscle activity (black). The three algorithms used for onset detection are the average, root mean square (RMS) and sample entropy. The threshold for each value was determined using an Otsu filter, commonly used in image/edge detection to filter a signal into two groups, in this case muscle activity and baseline. Each algorithm included a sliding window of 32ms with an overlap of 4ms. The only filtering methods applied to the data was a rectification step in contrast to normal noise filtering processes including bandpass/low pass filters. The speed of each algorithm was tested using the hardware and implemented in Python 3 as noted in Chapter 2.3 and is indicated above the signal.

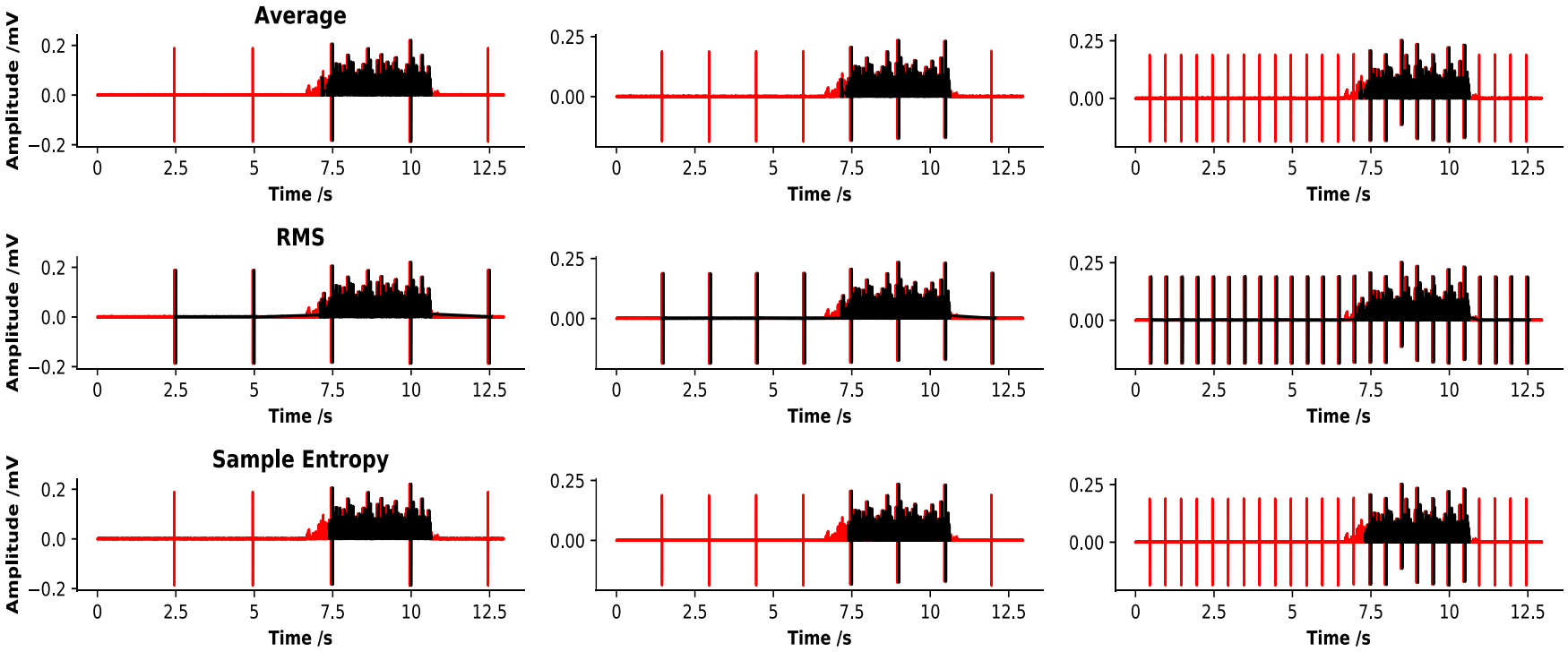

Figure 3-B: **Accuracy comparison between three algorithms for detection of onset of muscle activity with increasing levels of aberrant spiking activity**. Aberrant spikes were added to the signal in intervals of 2.5, 1.5 or 0.5s (columns). The three algorithms used for onset detection are the average, root mean square (RMS) and sample entropy (rows). Each spike was identical, made up of the signal maximum then minimum for a period of 0.0015s each.

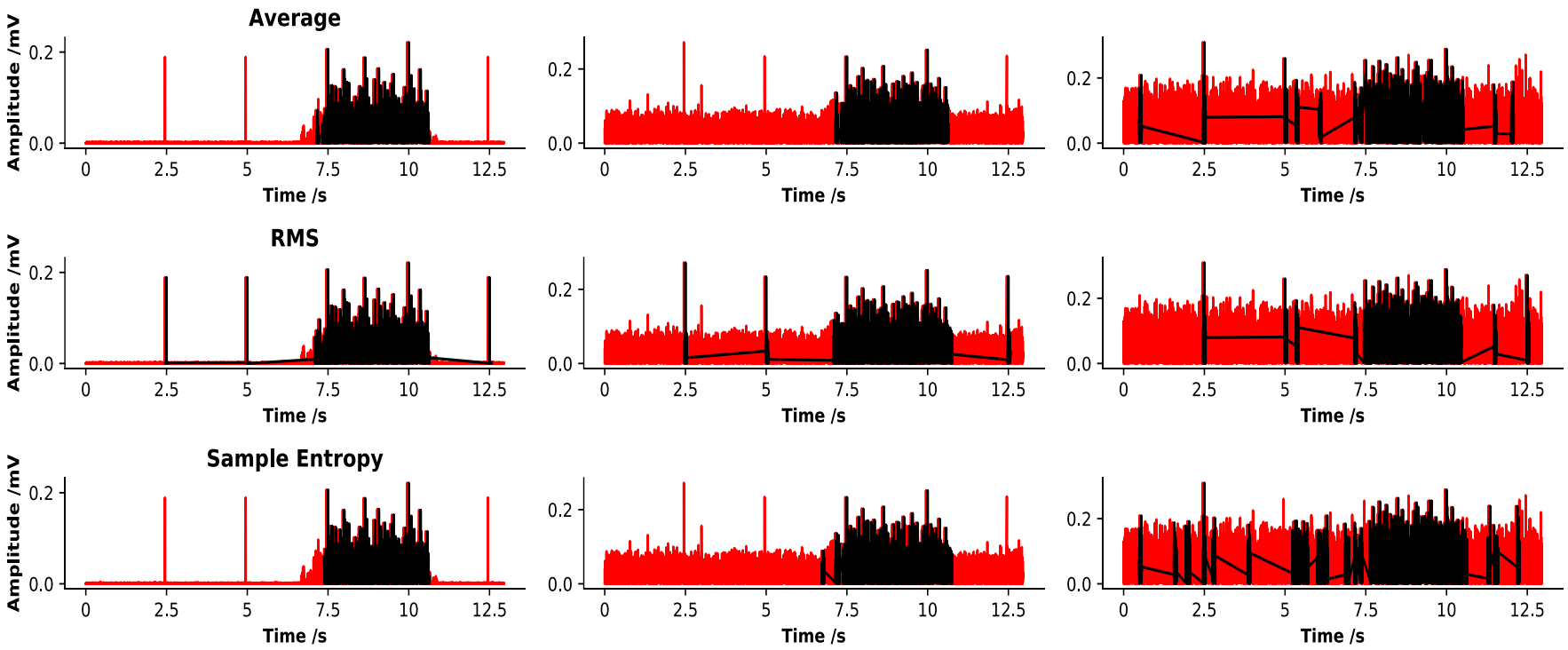

Figure 3-C: **Accuracy comparison between three algorithms for detection of onset of muscle activity with aberrant spiking activity and increasing levels of noise**. Aberrant spikes were added to the signal in intervals of 2.5s. Gaussian noise was added to each signal with a centre of 1 scaled by a multiplier of 0 (no additional noise), 6 or 18 (columns). The three algorithms used for onset detection are the average, root mean square (RMS) and sample entropy (rows). Each spike was identical, made up of the signal maximum then minimum for a period of 0.0015s each.

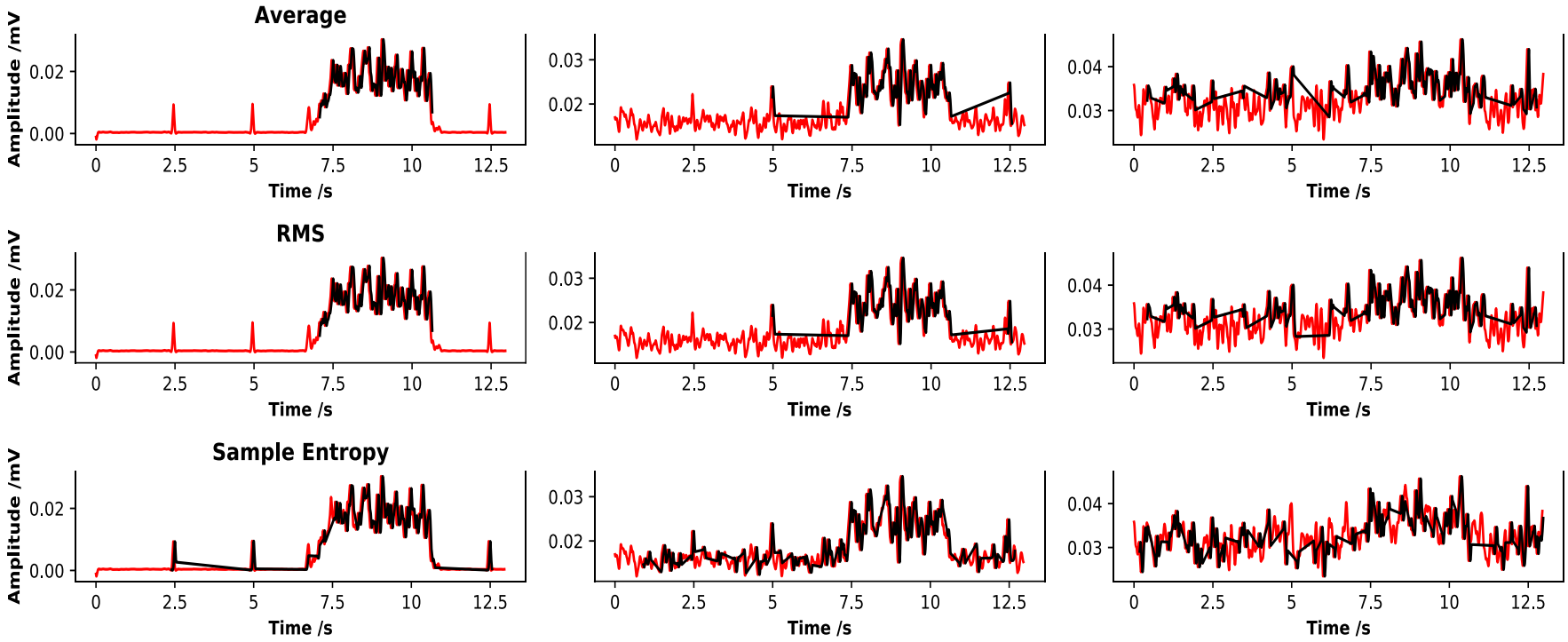

Figure 3-D: **Effect of standard filtering methods on accuracy comparison between three algorithms for detection of onset of muscle activity with aberrant spiking activity and increasing levels of noise.** Filtering consisted of a three-stage process. Signals were initially band-pass filtered (high pass = 20 Hz, low pass = 450 Hz, second order Butterworth filter), rectified and then finally zero-lag high-pass filtered (5 Hz, second order Butterworth filter) to remove frequency changes induced by rectification. Selection of filtering parameters was based off commonly used values for EMG analysis in the literature. Aberrant spikes were added to the signal in intervals of 2.5s. Gaussian noise was added to each signal with a centre of 1 scaled by a multiplier of 0 (no additional noise), 6 or 18 (columns). The three algorithms used for onset detection are the average, root mean square (RMS) and sample entropy (rows). Each spike was identical, made up of the signal maximum then minimum for a period of 0.0015s each.

3.3.2 NMF performs best among common synergy extraction methods

The performance of different synergy extraction algorithms was also examined for speed and accuracy. The four algorithms tested were PCA, ICA, factor analysis and NMF. To compare the accuracy of these methods it is necessary to have access to the original synergies that generated the EMG activity of interest. As described in section 2.4.5 EMG signals were generated from synthetic synergies and the algorithms were then asked to reverse this process and identify these muscle synergies. A representative example of the synergies generated, and the resulting EMG waveforms are shown in Figure 3-E. Both the synthetic synergies and the generated EMG waveforms are shown. Synergy vectors represent the contribution of each “channel” which are equivalent to muscles in real world terms. Synergy coefficients show when the synergy is recruited during a given movement or contraction. These waveforms and synergies match well with previous descriptions of muscle synergies and EMG waveforms.

The accuracy of each method was measured as the cosine similarity between the extracted synergies and the real synergies. A representative example is shown in Figure 3-F, although later figures show the cosine similarity calculated as the average performance over multiple synthetic synergies. In this example none of the extraction methods extract the synergies with perfect accuracy, however NMF has the highest r value for both synergies and for vectors and activation coefficients. Figure 3-G shows the average cosine values normalized to the performance due to random chance. Comparisons were made between these values using one-way analysis of variance (ANOVA) followed by a Tukey’s multiple comparison test. Residuals were tested for normality using a histogram and a Levene’s test for equal variance. This was followed by a one-way ANOVA. The mean cosine similarity was found to be significantly different for both synergy activation coefficients ($F = 3951.02$, $p < 0.05$) and for synergy vectors ($F = 3273.21$, $p < 0.05$). A Tukey multiple comparison test identified the direction and magnitude of this difference. For synergy activation coefficients all methods except FA and PCA were found to be significantly different (mean difference = 0.0019, $p = 0.550$) and that mean cosine similarity of NMF was significantly greater in comparison to all other methods (NMF– PCA; mean difference = 0.3934, $p < 0.05$, NMF– FA; mean difference = 0.3915, $p < 0.05$, NMF– ICA; mean difference = 0. 2974, $p < 0.05$). This relationship was also found to be true for synergy vectors with FA and PCA being not significantly different (mean difference = 0.0053, $p = 0.678$) and with NMF being significantly more accurate in comparison to all other methods (NMF– PCA; mean

difference = 0.0568, $p < 0.05$, NMF– FA; mean difference = 0.0515, $p < 0.05$, NMF–ICA; mean difference = 0.1103, $p < 0.05$). NMF shows a clear advantage in accuracy for identifying activation and synergy vectors. Of note here is the poor performance of ICA which in some implementations has been indicated to be the most accurate (Tresch and Cheung, 2006).

When different onset/offset detection algorithms were also used the performance of all methods degraded as shown in Figure 3-H. A two-way ANOVA was required to identify the effect of onset detection method and synergy extraction method on cosine similarity. Residuals were tested for normality using a histogram and a Levene's test for equal variance. There were statistically significant interactions between cosine similarity for both onset detection and between synergy extraction methods when examining synergy activation coefficients ($F = 327.63$, $p < 0.005$ and $F = 276.45$, $p < 0.005$ respectively). There was also a significant between group interaction for onset detection and synergy extraction ($F = 25.31$, $p < 0.005$). This finding was also true when examining synergy vectors with statistically significant interactions between cosine similarity for both onset detection and between synergy extraction methods ($F = 7.43$, $p < 0.005$ and $F = 8.37$, $p < 0.005$ respectively) but there was no longer the same between group interaction ($F = 1.25$, $p = 0.262$). The simple main effects of these interactions were identified using multiple pairwise comparisons. A table with the full pairwise comparisons is available in the Appendices. Relevant results to this analysis are the significantly lower cosine values for all algorithms across every onset detection algorithm. NMF continues to outperform all other extraction algorithms in combination with each onset detection algorithm. Of these methods a moving average reduced performance the least and SampEn the most.

In terms of calculation speed algorithms were compared for a single example of EMGs. PCA was calculated in <0.0001s, FA, in 0.17s, ICA in 1.14s and NMF in 0.08s. From these results NMF presents a balance between an acceptable calculation speed (0.08s corresponds to 12.5 frames per second, or about half the speed that is required for smooth capture of motion in video. This delay is small enough that other aspects of the code are likely to dominate lag in implementation) and accuracy. PCA was faster than NMF but had significantly lower r values when applied to the synthetic dataset. Therefore, NMF was chosen as the method for further implementation within the online synergy extraction algorithm.

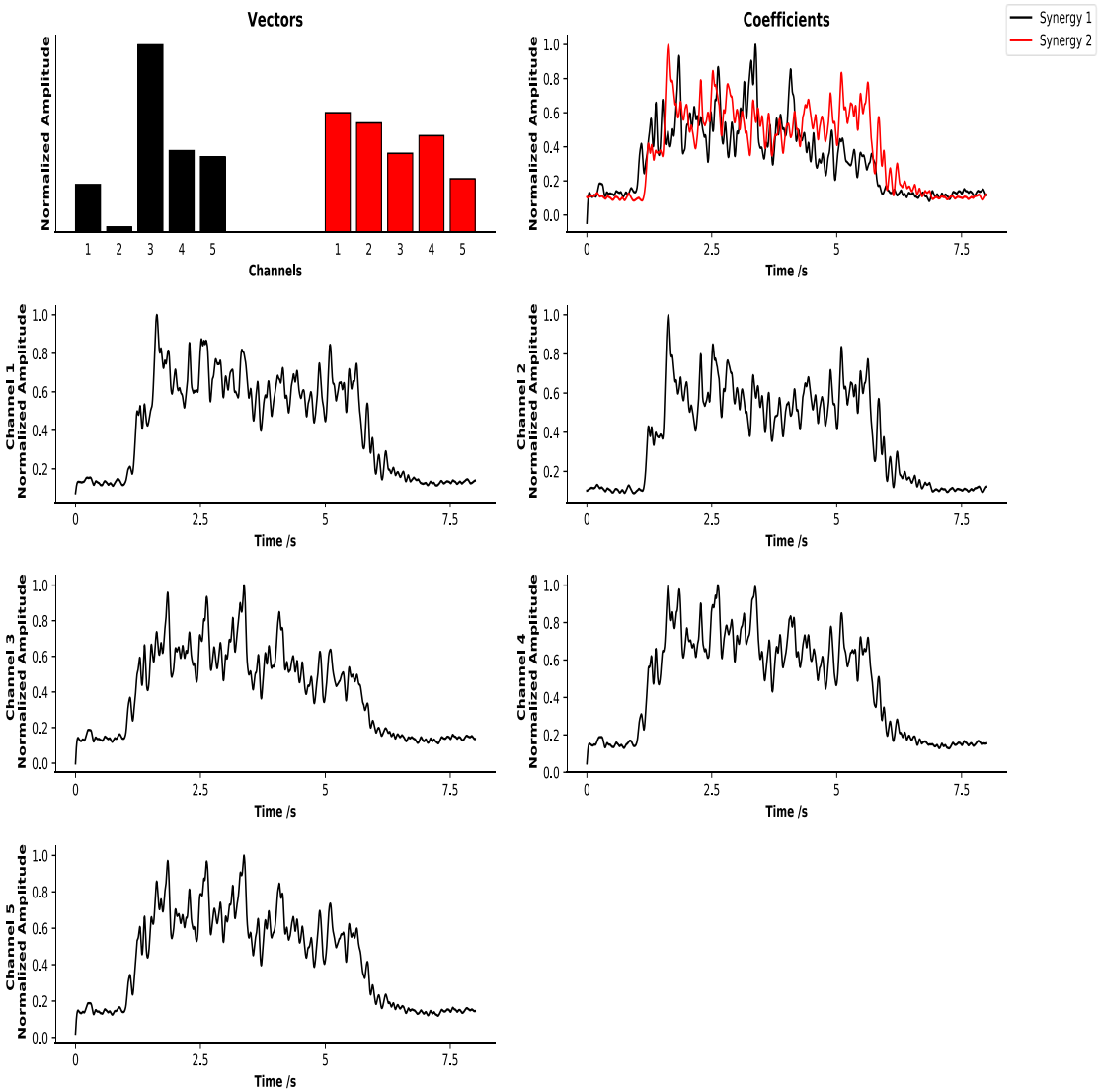

Figure 3-E: **Example of simulated synergy coefficients and vectors and resulting synthetic muscle activity.** (TOP LEFT) Bar chart represents synergy vectors corresponding to individual channel (muscle) contribution to the synergy 1 and 2 (black, red). Vectors were randomly generated numbers constrained to be positive numbers between 0 and 1 due to the positive nature of muscle activity ruling out negative synergies. (TOP RIGHT) Line graphs are synergy coefficients corresponding to recruitment of synergy 1 and 2 across the muscle contraction (black, red). Coefficients were generated by selecting a random muscle and participant from a previously collected dataset of upper leg muscle EMGs recorded during isometric knee extraction with an added Gaussian noise distribution centred on 1 and scaled by 3, standard filtering (high pass= 20 Hz, low pass = 450 Hz, second order Butterworth filter) and then normalized to maximum signal amplitude. (BOTTOM) Synthetic muscle activity was generated by taking the dot product of the two vector and coefficient matrices. These were then normalized to their maximum amplitude.

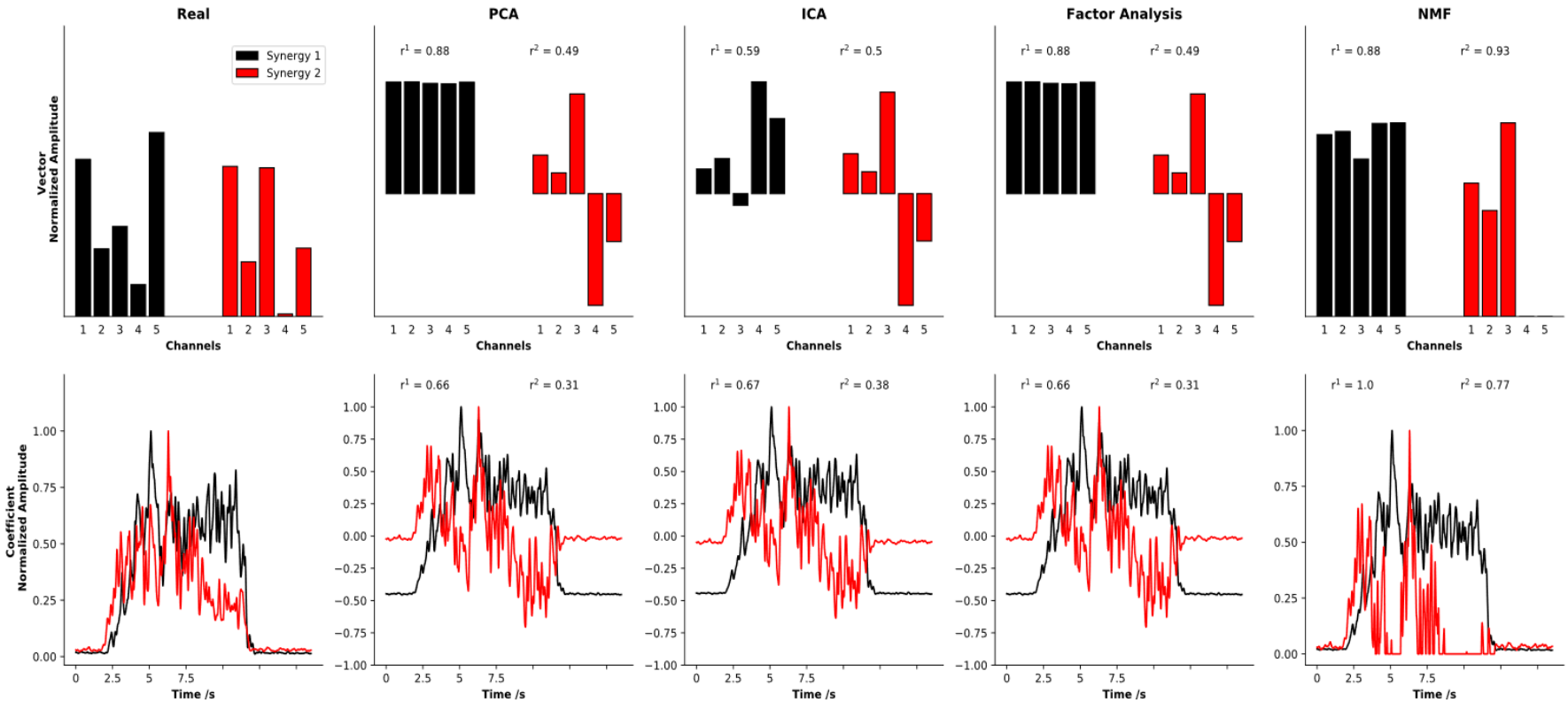

Figure 3-F: **Accuracy of four commonly used muscle synergy extraction methods on a representative example of synthetic synergies.** Synergies were extracted from the muscle activity generated by the dot product of the synthetic synergies, labelled real, using principal component analysis (PCA), independent component analysis (ICA), factor analysis (FA) and non-negative matrix factorization (NMF) (columns). Bar charts represent synergy vectors, line charts are synergy coefficients for synergy 1 and 2 normalized to their maximum value (rows, black and red). R values correspond to cosine similarity values, wherein -1 corresponds to negatively correlated values, 1 corresponds to perfect correlation and 0 represents uncorrelated values. Algorithm performance could be due to random chance. This was accounted for by calculating the cosine value between the extracted synergy and 50 other examples of uncorrelated examples of synthetic data, which corrects for bias due to the data simulation method. Cosine values were then normalized to this value due to random chance such that r = 0 corresponds to correlation due to random chance.

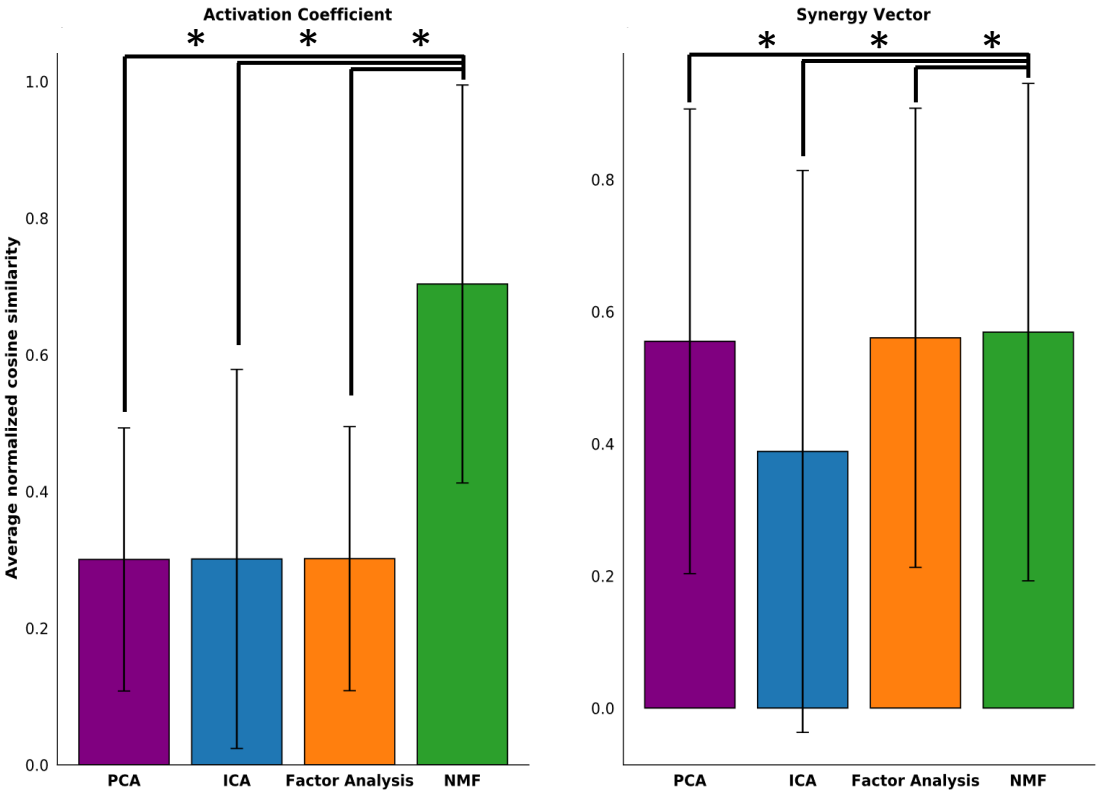

Figure 3-G: **Average cosine similarity between synthetic synergies and synergies extracted by four commonly used muscle synergy extraction methods.** Synergies were extracted from 100 examples of synthetically generated muscle activity separated into synergy activation coefficients and vectors. Error bars are standard deviation. Synergy extraction methods used were principal component analysis (PCA), independent component analysis (ICA), factor analysis (FA) and non-negative matrix factorization (NMF). Asterix and black bars above bar charts indicate significance following ANOVA and Tukey multiple comparison test in relation to mean cosine similarity of NMF. NMF was found to have significantly greater cosine values than other methods for both activation coefficients (NMF– PCA; mean difference = 0.3934, $p < 0.05$, NMF– FA; mean difference = 0.3915, $p < 0.05$, NMF–ICA; mean difference = 0. 2974, $p < 0.05$) and for synergy vectors (NMF– PCA; mean difference = 0.0568, $p < 0.05$, NMF– FA; mean difference = 0.0515, $p < 0.05$, NMF–ICA; mean difference = 0.1103, $p < 0.05$).

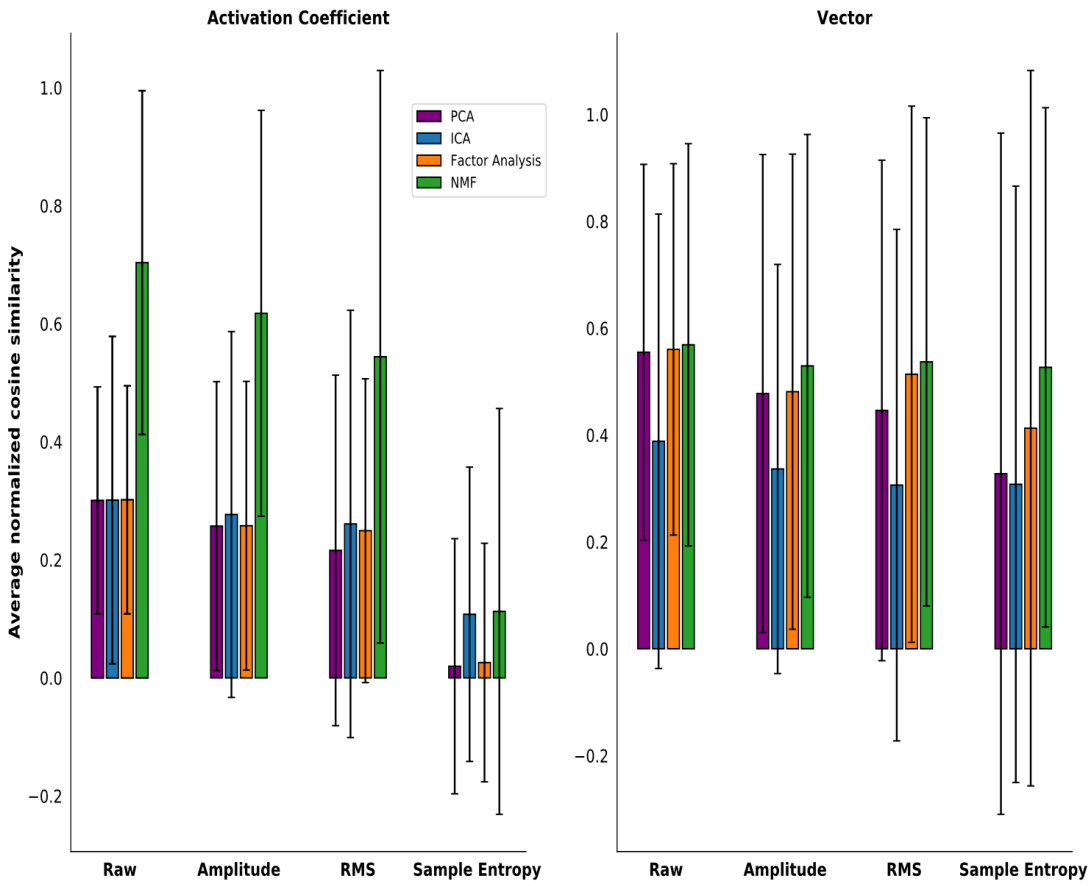

Figure 3-H: **Effect of three different onset detection algorithms on synergy detection accuracy of four commonly used muscle synergy extraction methods**. Synergies were extracted from 100 examples of synthetically generated muscle activity following detection of muscle activity of interest by three onset detection measures. The measures used was an average of the signal amplitude (Amplitude), the root mean square (RMS) and the sample entropy (Sample Entropy). Performance on raw data is shown for comparison (Raw). All detection algorithms used a sliding window of 32ms with a 4ms overlap. Error bars are standard deviation. Synergy extraction methods used were principal component analysis (PCA), independent component analysis (ICA), factor analysis (FA) and non-negative matrix factorization (NMF).

3.3.3 Application of NMF to isometric knee extension task

Of the 7 different muscles of the leg recorded only 5 of these were used for further analysis of activity and patterns as on examination the muscles TA and MG were always inactive, as expected due to the nature of the task. Muscle synergies were extracted from the EMGs recorded from 5 muscles across two different positions to examine how proprioceptive feedback alters muscle synergy recruitment. The contralateral hip was flexed or relaxed to induce passive insufficiency in the recorded leg to highlight differences in proprioceptive feedback. A photo capturing the different leg positions is shown in the Appendices. A spinal population circuit model was created with connections between interneurons, motor neurons and afferent feedback, based on current CPG models and accepted neural circuits (Pierrot-Deseilligny and Burke, 2005). The model was generated after extraction of the experimentally observed muscle synergies. Alterations were made to the overall structure of the model based on these findings (such as the required additional excitatory connections required to replicate the bias towards RF and ST) Figure 3-L shows the EMG signals for all five muscles after rectification and smoothing, and the average firing rates of the motor neuron populations in the simulation. It is difficult to discern the meaning of differences between the time series, highlighting the need for analysis techniques such as NMF.

3.3.4 NMF identifies two muscle synergies from the EMG activity

To identify synergies appropriate for experiment-model comparison, NMF was performed with a range of rank values, as previously mentioned the rank factor corresponds to the number of synergies extracted. The appropriate rank to use was chosen as the number required to raise the VAF above 90% which can be observed in Figure 3-I as the dotted line. In this case rank two raised VAF above this threshold. Although 90% is an arbitrary threshold, and there are other methods for choosing appropriate rank, patterns identified by three or more synergies were less consistent across participants. As described in Section 2.4, each synergy consists of a column of matrix $\mathbf{W}$ with length five (one value per muscle) and a row of matrix $\mathbf{C}$ representing a time series describing some underlying structure of the original data. For each muscle, the corresponding component of $\mathbf{W}_{*s}$ multiplied by $\mathbf{C}_{*s}$ gives the contribution of synergy, s, to that muscle's EMG. Cosine similarity analysis was performed on the synergy rows and columns across participants for each position, synergy and angle. There is high correlation between synergy 1 results among the participants, regardless of position and

internal knee angle as seen in Table 3-A. Though not as high as synergy 1, there is also high correlation between participants for synergy 2. Despite some variation, the r values in Table 3-A suggest that there is a common pattern of muscle synergy recruitment across all participants.

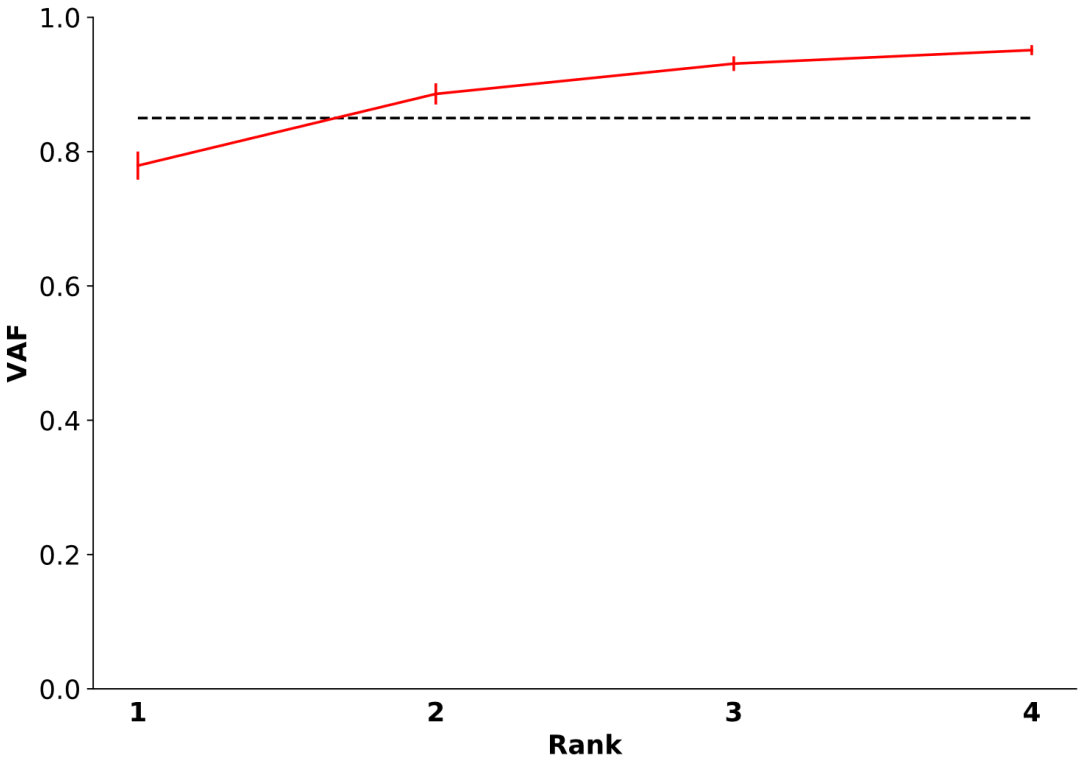

Figure 3-I: **Average variance accounted for (VAF) scree plot for rank one to four NMF dimensionality reduction across all angles and both positions of the isometric knee extension task.** The 90% VAF threshold indicates that two is the appropriate rank to use and therefore the number of synergies to extract. Error bars show Standard Error of the Mean (SEM).

	Synergy(s)				Angle
Position 1		0°	20°	60°	90°
Muscle Contribution Vector ($\mathbf{W}_{*S}$)	**1**	0.92	0.94	0.88	0.89
	2	0.77	0.66	0.69	0.58
Activation pattern ($\mathbf{C}_{*S}$)	**1**	0.96	0.97	0.97	0.97
	2	0.66	0.75	0.73	0.69
Position 2					
Muscle Contribution Vector ($\mathbf{W}_{*S}$)	**1**	0.94	0.93	0.92	0.89
	2	0.67	0.65	0.62	0.70
Activation pattern ($\mathbf{C}_{*S}$)	**1**	0.96	0.96	0.97	0.96
	2	0.68	0.74	0.73	0.76

Table 3-A: **Synergy rows and columns (as defined in section 2.4.10) were compared across all pairs of participants using cosine similarity analysis following synergy extraction using NMF.** Cosine similarity analysis outputs a value between -1 (negatively correlated) 0 (uncorrelated) and 1 (positively correlated***).*** For both positions (activating or inactivating the contralateral hip flexors) and for all internal knee angles, there is high correlation between subjects indicating that, during the task, the same synergy patterns are being recruited by the majority of subjects.

3.3.5 Synergy 1: Coordinated, balanced recruitment of all muscles is a canonical recruitment pattern in anisometric task

The NMF process generates, for each of the two synergies, a time series activation pattern and a vector of five values, one for each muscle. Figure 3-J shows the vector and time series of synergy 1 (A) and 2 (B) for both positions across different internal knee angles. The activation patterns (line plots) should be considered in conjunction with the five value muscle contribution vectors shown in the bar charts. Synergy 1 represents general coordinated muscle recruitment as would be expected in an isometric extension and contributes to the majority of the observed EMG activity. Because of this, the activation pattern closely matches the overall profile observed in the raw EMG data (the transition from low to high to low activity during the contraction). The high muscle contribution values for all five muscles indicates that this activation pattern is present in all five EMG recordings. Both the activation pattern and muscle contribution weights are well conserved across all angles, positions, and muscle groups. Among the muscle contribution values, there is a slight shift between 0° and 90° from a quadriceps bias to a hamstring's bias, however this change is less apparent in position 2. The well correlated vector values in synergy 1 were used to eliminate outliers and reduce the variability of synergy 2. If any synergy 1 vector value fell below 5 or above 6.3, we removed that trial from the results. In many of the trials which were excluded, the time series activation patterns were observably different from the average. While these could represent other legitimate synergies, the two modal synergy pattern was chosen for further investigation as representing the majority of subjects.

3.3.6 Synergy 2: The degree of muscle stretch regulates a balance between the activity of agonist and antagonist muscles

The shape of the activation pattern of synergy 2 indicates that this synergy captures a difference between the activity of each muscle during the resting and transition periods at the beginning and end of the contraction. During the contraction, the contribution of synergy 2 reduces to near zero because all muscles reach their maximal activity which is the feature captured solely by synergy 1. The patterns of synergy 2 change for different knee angles and position indicating that there is a proprioceptive effect on muscle activation even in an isometric task such as this. In position 1, as the internal knee angle is increased, there is a marked drop in the average of contribution vector values for the antagonist muscles whereas the average of the agonist muscles shows the opposite

trend. At 90°, the average magnitudes are the same for both muscle groups indicating that the proprioceptive feedback is balanced. In individual cases, the vector values vary as to which muscles receive a bias which is confirmed by the high variability of the data at this angle. What is important is that there appears to be no preference for any muscles in contrast to the lower angles.

3.3.7 Synergy 2: At the limit of extension, afferent signals strongly affect synergy patterns in both positions

At 0°, in both positions, the contribution vector values for the agonist muscles are zero while the antagonist muscles show high non-zero values. This indicates that the range of activity of the antagonist muscles was reduced compared to the agonists. This is consistent with additional excitation to the knee flexors or inhibition of the extensors when the leg is near the limit of extension. In position 2 at 20°, the antagonist bias is flipped to the agonists. Such a stark difference between 0° and 20° could be due to the nonlinear nature of afferent feedback but it could also demonstrate two functionally different afferent signals at play. One signal to represent extreme extension which is active at 0° and another to represent the overall muscle stretch which at this angle and position shows a bias towards the knee extensors. At 20°, the first signal may be switched off. In position 1, the strong antagonist bias remains at 20°, suggesting that, if there is afferent activity signalling the extension limit, it persists due to passive insufficiency.

3.3.8 Synergy 2: Across many angles and positions, there is a stronger bias towards the bifunctional muscles

In many individual cases, the synergy 2 pattern sets the contribution vector value of either RF or ST very high compared to the other muscles. In position 2, with the exception of 0°, there is a higher average vector value for RF than any other muscle with a lower variance. At 0° for both positions and at 20° in position 1 (near the extension limit) there is a strong bias to ST compared to biceps femoris. At higher angles in position 1, the ST bias appears to reduce and then vanish entirely.

3.3.9 The model reproduces synergies observed experimentally

During each MIIND simulation, the two afferent feedback inputs were kept constant and the Cortical Drive input was changed from low to high activity to reproduce the contraction behaviour. All populations produced average firing rates which were either

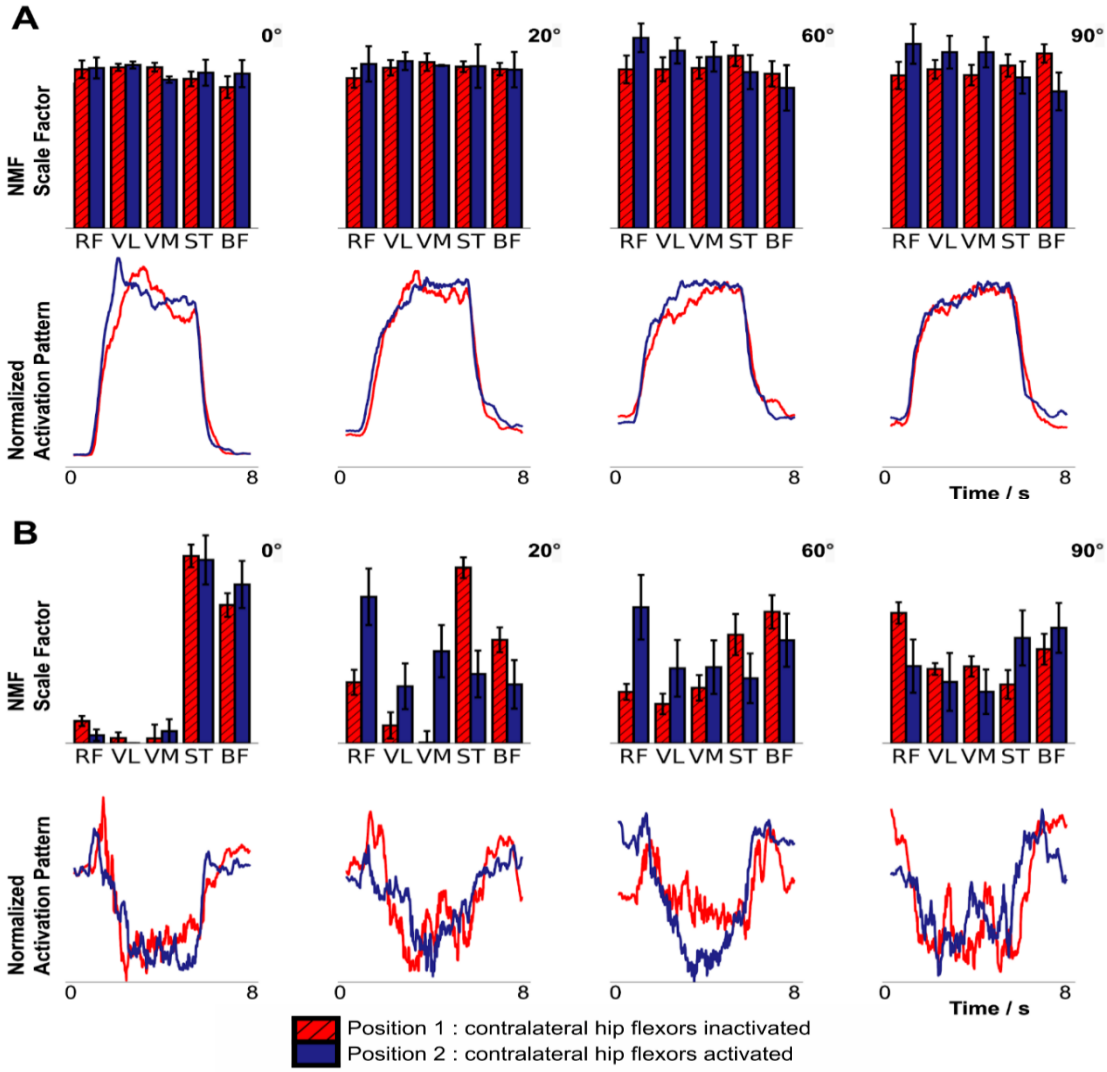

***Figure 3-J*: Muscle synergies extracted using rank two NMF from an isometric knee extension task at four internal angles of the knee (0°, 20°, 60°, and 90°). (**N = 17, mixed gender, male = 9, female = 8, age range of 18-30 (24.4±2.57years). Subjects performed 6 contractions of 5s with the subject being asked to maximize rectus femoris activity. NMF was performed on the average EMG of each subject's 6 contractions. The experiment was repeated across two positions inactivating (red values) or activating (blue) contralateral hip flexors. Line charts are activation patterns identified by NMF as underlying structure in the original EMG time series. Bar charts show the contribution of the associated activation pattern to the activity of each of the five muscles in arbitrary units. Error bars represent standard error of the mean. A: Synergy 1 demonstrates a balanced, coordinated contraction across muscle groups in line with what is observed in the raw EMG data. B: Synergy 2 for position 1 (top in red) shows the balancing of antagonist/agonist activations between the quadricep muscles and hamstrings. Synergy 2 for position 2 (middle in blue) shows the same extreme antagonist bias at 0°with the leg at maximal extension. However, there is a strong agonist bias at 20°perhaps demonstrating the effect of less passive insufficiency. RF:Rectus Femoris; VL:Vastus Lateralis; VM:Vastus Medialis;ST:Semitendinosus; BF:Biceps Femoris

passed to connected populations in the network or recorded for analysis. The activity of the five motor neuron populations, MN-RF, MN-VL, MN-VM, MN-ST and MN-BF, was analysed. The raw output from these populations is shown in Figure 3-L (top right). The output is a great deal smoother than the overlaid EMG recording data due to MIIND's simulation technique and the lack of many of the experimental sources of noise. Though there is undoubtedly a great deal more information available in the EMG traces, the model is designed only to explain how the two synergies are produced and, as will be shown, a smooth rise and fall in activity is sufficient.

The heat plots in Figure 3-L (top left) show the probability density functions produced by MIIND for each population in the network. As shown in Section 2.6, the density function describes the likelihood of finding a neuron from the population with a given membrane potential. The top density plot shows the state of the MN-RF population during the period before the action begins. The lower density plot shows the state when the input is maximal. In the lower density plot, there is a higher probability of finding neurons at the threshold (-51mV) indicating that the average firing rate of that population is higher. The population transitions to the top density once again after the Cortical Drive returns to zero. These transitions are also visible in the probability density functions of the other motor neuron populations due to the indirect excitation from Cortical Drive via the Extensor and Flexor Interneuron populations. Therefore, for all motor neuron populations, as with the EMG signals, the average firing rate output shows an increase to a high level of activity followed by a decrease to rest.

In the same manner as the EMG recordings, rank 2 NMF was performed on the time series of average firing rates of the motor neuron populations in the model producing a five-value muscle contribution vector and time series activation pattern for both synergies. The afferent feedback inputs to the Extensor Interneuron, InhibRF and InhibST populations were altered and the results were compared to those of the isometric task. Figure 3-K shows the results from the NMF process. As seen in Figure 3-K (A) for synergy 1, the activation pattern matches the shape of the descending input pattern from the Cortical Drive input (5 seconds of maximal activity with a 1 second ramp up and down). The five muscle contribution values are all well above zero indicating that the activation pattern is a component in the activity of all the motor neuron populations.

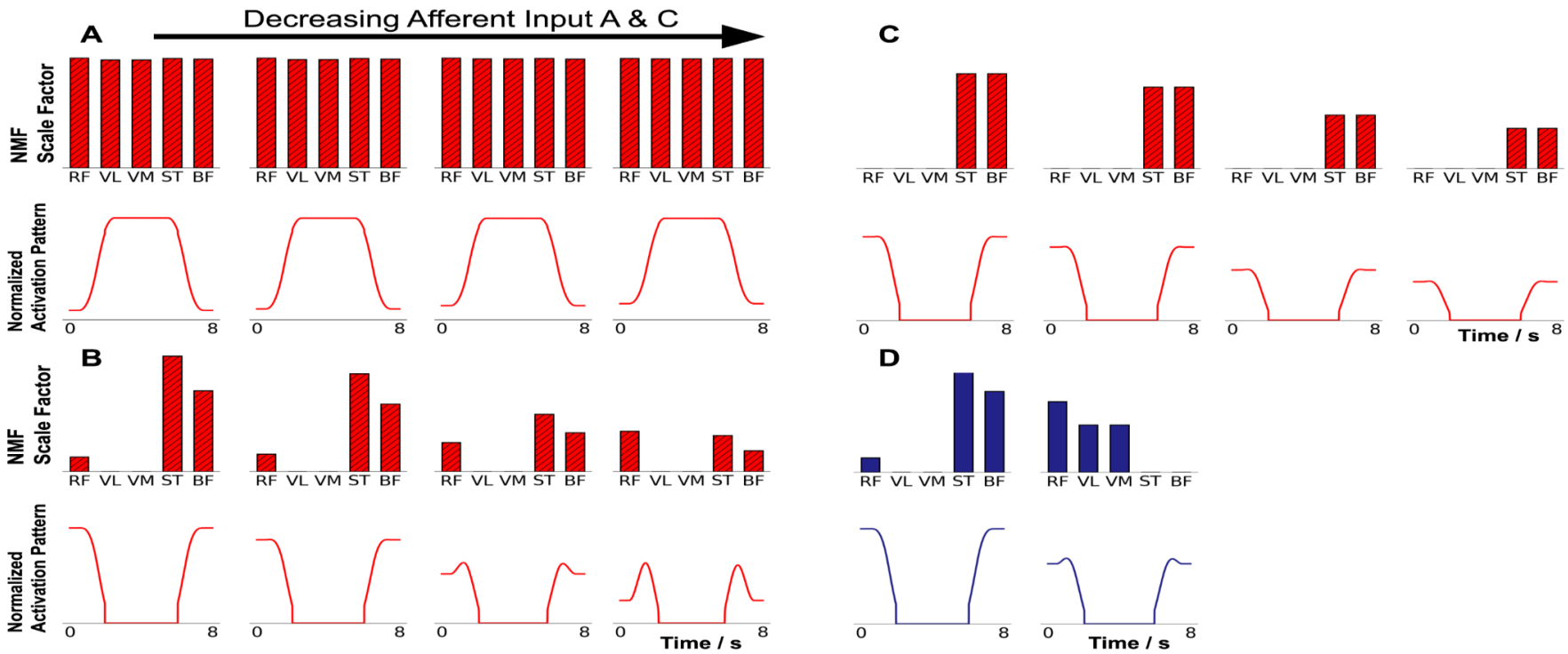

Figure 3-K: **Muscle synergy features extracted using rank 2 NMF applied to the average firing rates of five motorneuron populations for different levels of input from Afferent Input A (1).** As with the experimental results, line plots indicate the activation pattern for each synergy and bar charts indicate that pattern's contribution to each motor neuron population's activity. (A) Synergy 1. The activation pattern and contribution vector remain constant for all levels of afferent input. (B) Synergy 2 produced by the model in figure 2-A. The two farthest left charts show exaggerated antagonist bias due to activity from Afferent Input C in addition to Afferent Input A. (C) Synergy 2 produced by the model in which all motor neuron populations have the same connection strength from Extensor and Flexor Interneuron populations (MN-RF and MN-ST receive no additional bias). (D) To reproduce the Synergy 2 patterns of position 2 at 0°(left) and 20°(right). On the right, Afferent Input A was further reduced to below the level of Afferent Input B resulting in bias towards the agonist motor neuron populations. On the left, even with a low level of Afferent Input A, a high Afferent Input C to represent maximal extension at the knee can reproduce the pattern for position 2 at 0°.

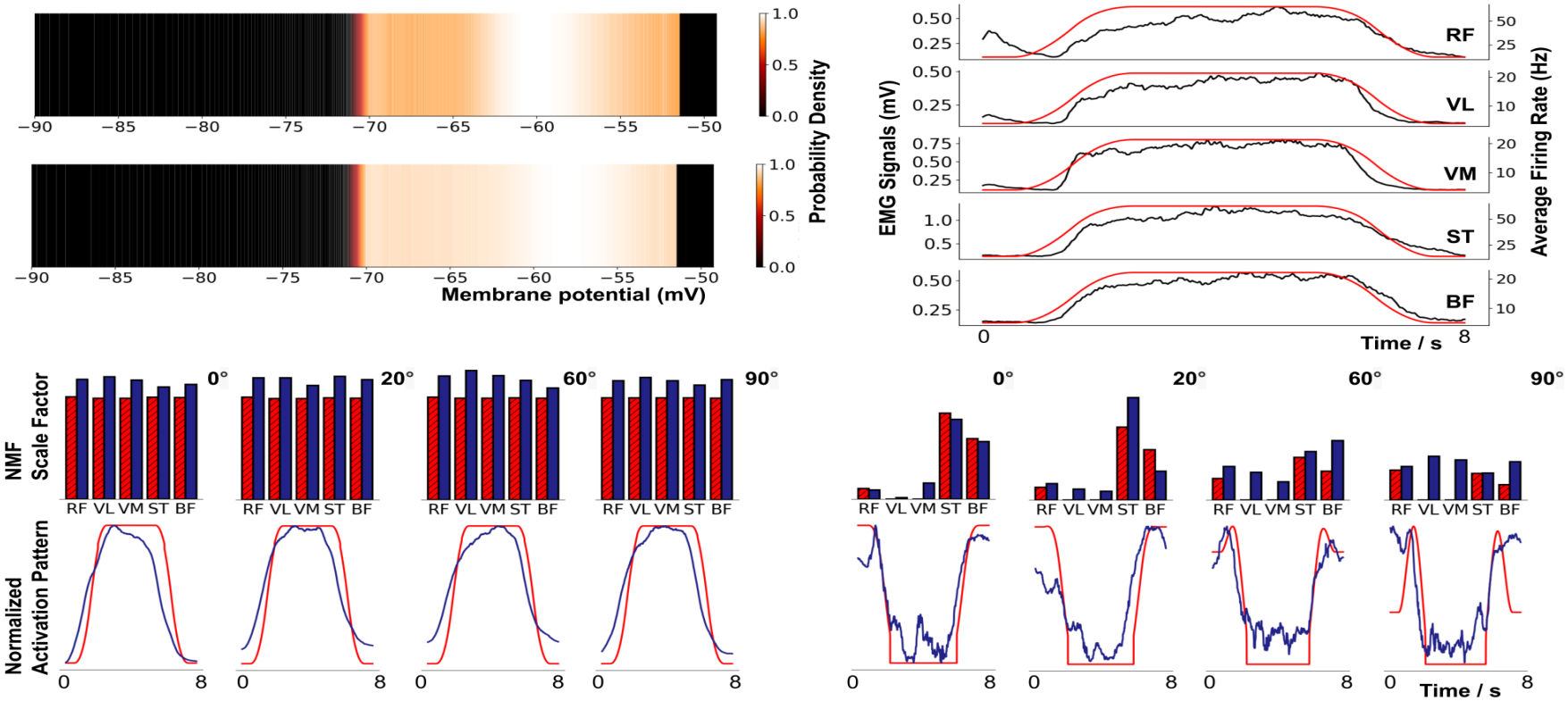

Figure 3-L: **Comparison of simulation results to experimental findings following synergy extraction.** (TOP LEFT): The probability density function of the MN-RF population in the model before input from cortical drive (upper) and during the contraction (lower). Colour brightness indicates the probability of a neuron in the population having that membrane potential. The y axis of the plots represents an arbitrary value for simple exponential integrate and fire neurons. A higher probability at the threshold of -51mV indicates a higher average firing rate for the population. (TOP RIGHT): The average firing rate of each motor neuron population in the model and the rectified and smoothed EMG output for each muscle. Bottom: The muscle contribution vector and activation pattern time series for synergy 1 (left) and 2 (right) for the model (hatched bars) and for experimental data from position 1 (solid bars with std errors). Indicative levels of afferent activity in the model have been used for comparison with each internal knee angle of the experiment.

3.3.10 Changing afferent inputs A or B creates a bias in synergy 2 between agonist and antagonist motor neuron populations

The synergy 2 seen in Figure 3-K (B) activation pattern drops to zero during the contraction and returns to its starting value at the end. The degree to which this pattern contributes to each motor neuron population's activity changes with the different combinations of afferent inputs. When afferent input A is higher than B, the activation pattern contributes to the antagonist motor neuron populations significantly more than the agonists as was observed in the experimental results. The additional excitation from input A causes an imbalance in activity between the Extensor Interneuron population and Flexor Interneuron population. The resultant higher firing rate of the Extensor Interneuron population causes additional excitation of MN-ST and MN-BF and inhibition of MN-RF, MN-VL and MN-VM. Therefore, during the entire contraction task including the resting period, the antagonist motor neuron populations have a consistently higher firing rate than the agonist populations. This is how a bias in the synergy pattern to either the agonists or antagonists is controlled. As the difference between afferent inputs A and B is reduced, the contribution of this pattern lowers until itis eliminated across all five populations. For the EMG recordings, at 20° in position 2, the agonist/antagonist bias is reversed. This can be reproduced in the model by increasing afferent input B above A which creates a bias towards the agonist motor neuron populations in the contribution vector. It is possible that as passive insufficiency is reduced in position 2, the afferent feedback further shifts to the Flexor Interneurons following the trend identified with increasing angle in position 1.

3.3.11 The additional connection strength to MN-RF and MN-ST produces a bias for those two populations in synergy 2

In position 1, the contribution vector value of ST is higher than that of BF at 0°. This bias remains at 20° then reduces at 60°before being eliminated entirely at 90°. The additional connections between the Extensor Interneuron population and MN-ST cause the activity of MN-ST to increase both during the rest and contraction periods (although the range is reduced) which induces a higher contribution vector value for MN-ST compared to MN-BF. This effect is "multiplied "by the higher activity of the Extensor Interneuron population compared to the Flexor Interneuron population which explains why the bias is greater when afferent input A is much higher than B. However, were this the only mechanism for altering the bias, it should still be visible at 90°where the afferent inputs are balanced. In

order to eliminate the bias, the inhibitory population InhibST is required to offset the additional activity from the Extensor Interneuron population. This mechanism is mirrored for the MN-RF population. In position 2 with the exception of 0°, RF has a consistently high contribution vector value. The additional connections to MN-RF from the Flexor Interneuron population enable a difference in the synergy pattern to that of MN-VL and MN-VM and the InhibRF population allows modulation of the bias.

3.3.12 Afferent input C provides a strong bias in synergy 2 for the antagonist muscles during maximum extension

To produce the synergy 2 patterns at 0° in both positions and 20° in position 1, all that is required is to provide a large amount of excitation through afferent input A. The sharp change to the synergy patterns at 60°in position 1 and 20° in position 2 indicates that the afferent input does not change linearly or there is a separate additional afferent signal causing this pattern. In both cases, this can be modelled with a separate afferent input C. In the model, at 0° in both positions, afferent inputs A and B are switched off and C is switched on to produce the required pattern. If A and B remained active, the agonist motor neuron populations in position 1 would be completely inhibited, eliminating both synergies. Likewise, in position 2, afferent input C would need to be much higher to overcome the opposing excitation of the Flexor Interneuron population from input B. At maximal extension therefore, the model predicts a step change in afferent signals or an entirely separate afferent pathway which is activated in this scenario. Although this afferent input is labelled as a single pathway within the model it may correspond to one or many sources that produce this step change in behaviour.

3.3.13 The model does not account for variation in afferent signals from trial to trial

Figure 3-L shows the side by side comparison of the synergies extracted from the simulation and average synergies from the EMG recordings for both positions. As discussed above, many of the patterns and trends are captured by the model. However, there are a few differences worthy of discussion. In position 1, the model produces no contribution vector values in synergy 2 for MN-VL and MN-VM in contrast to the experimental results. The model provides no variability in the inputs to these populations and no mechanism for changing their activity in comparison to MN-RF. This is particularly obvious at 90°where, in the experimental results, there is an equal chance of seeing a

high contribution vector value for all muscles which leads to the common low average vector value with high variability. The equivalent in the model is a zero-vector value for all motor neuron populations in synergy 2. The trend in agonist/antagonist synergy bias in position 1 which is perhaps extended to 20° in position 2 is not continued for 60° and 90°. The model currently offers no explanation for the changes in synergy pattern although it is still possible to reproduce them by changing the afferent inputs and/or cortical drive to specific motor neuron populations.

3.4 Discussion

The major findings of this study show that synergy recruitment during an isometric knee extension is affected by proprioceptive feedback, and that these synergies can be reproduced by a neural population model integrating afferent feedback. We also show that the performance of automated methods of muscle activity analysis, whether it be onset/offset detection or synergy extraction algorithms, varies dependent on the data examined and the choice of hyper parameters. The synergies recruited during the isometric task are well conserved across conditions and individuals, consisting of simultaneous muscle activation and the balancing of agonist-antagonist recruitment relative to internal angle of the knee. These results are further supported by findings from a novel simulation of the local spinal circuits showing proprioception from muscles contribute to synergy level organization of motor control in humans during isometric tasks. Whilst our results are largely in line with previously established literature regarding synergy recruitment, we differ in our finding that joint angle and therefore afferent feedback regarding joint position alters synergy recruitment (Torres-Oviedo et al., 2006; Roh et al., 2012; Sohn and Ting, 2016). We propose that in this case, because the available synergies are constrained due to the nature of an isometric task, adaptation is achieved through changes in recruitment. Inspection of the synergies extracted during NMF analysis matches well with biomechanical interactions expected of the muscles, with synergy 1 reflecting coordinated contraction of all muscle groups and synergy 2 reflecting the agonist-antagonist pairing of the hamstrings and quadriceps. The similarity of each synergy's activation pattern supports that these are the same synergies being recruited at each angle. The changes observed in synergy 2 at different internal angles of the knee demonstrates a clear effect of proprioception on synergy recruitment. Quadriceps and hamstring activity in synergy 2 is balanced at a smaller angle when the contralateral hip is flexed. This further reinforces that these changes reflect the influence of afferent feedback due to change in relative muscle stretch requiring re-balancing of

the agonist-antagonist activity. This finding challenges long held assumptions that proprioception does not play a role in isometric tasks and synergy recruitment.

An important factor in justifying our results is the appearance of high contribution vector values for the antagonist muscles in both synergies. When studying synergies using NMF, it can be the case that the contribution vectors are almost entirely disjoint across synergies. When this happens, it is an indication that the NMF process has simply classified the original set of EMGs into matching groups. This can be confirmed if the synergy activation patterns are almost identical to the associated EMGs. In our study, the high antagonist contribution values in both synergy 1 and 2, coupled with the activation pattern in synergy 2 being starkly different to the EMG time series, indicates that NM has identified underlying structure in the data.

3.4.1 Evaluation of muscle activity analysis algorithms is data dependent

Two related methods of analysing EMG signals were evaluated in the first section of this study, onset/offset detection and dimensionality reduction for the purposes of synergy extraction. In an automated setting, determining the activity of interest is of vital importance. Of the methods examined here a sliding window of average values was found to be as effective as the more computationally intensive measure of SampEn. Averaging was as effective in high noise conditions, as well as with extremely high frequency spiking activity, conditions it has been suggested previously SampEn had a distinct advantage in. Furthermore, whilst the performance of all algorithms was worse in the presence of standard filtering methods, the performance of SampEn was particularly badly affected, whereas a sliding average was still comparable to methods of visual inspection. Using RMS as a measure was inferior in conditions except the no noise signals and is therefore entirely unsuitable for onset/offset detection. With the significant decrease in computation time associated with a sliding window it calls into doubt the utility of SampEn as a measure for automated burst segmentation in an online scenario.

The performance of synergy extraction algorithms was compared on synthetically generated EMG signals. Of these methods the performance in terms of cosine similarity advantages between methods was similar for determining synergy vectors whereas NMF has a significant advantage in activation coefficients. Examining specific examples within this dataset it becomes clear that of the four methods examined, NMF had much fewer examples of poorly matched samples than other methods. This was particularly evident

in the case of ICA wherein some matches outperformed NMF and in some cases it was the worst performing method. In terms of computational speed PCA is performed almost instantaneously and therefore has the greatest advantage when speed is of the utmost importance. ICA on the other hand is the slowest of methods and would be unsuitable with a naive implementation for real time uses. Finally, all methods appeared sensitive to onset/offset detection algorithms. This is likely due to the inclusion of additional “noise” data in comparison to visual segmentation which only includes activity of interest. NMF appears to strike a balance between computation speed and accuracy, although it should be noted that NMF calculation time increases steeply as the sample size increases. From this result and due to its algorithmic restrictions being in line with assumptions regarding muscle synergies, NMF was selected as the synergy extraction algorithm for further testing.

3.4.2 Muscle synergies extracted from isometric extension of the knee are altered in relation to internal angle of the knee

Our results contrast with findings that muscle synergies present during isometric force generation in the hand are insensitive to changes in position or load (Roh et al., 2012). The difference in findings may be reflective of either a different mode of control for muscles of the upper limb or a difference in requirement and outcome of the task resulting in recruitment of more stable synergies. Further examination is required to investigate the cause of these differences. More striking still is the comparison to synergy recruitment during postural perturbations these dynamic movements required five synergies to adequately explain variance and yet none of these synergies were significantly altered with changes in posture or initial limb configuration (Torres-Oviedo et al., 2006). It would seem reasonable to assume that these conditions would be more sensitive to changes in afferent drive due to the greater complexity of the movements involved. We hypothesised that a fixed isometric task should isolate changes in muscle synergies to those due to proprioceptive feedback. Greater restriction of movement may necessitate alteration of synergy recruitment to produce changes in end-point forces, whereas more dynamic movements might allow subtle postural changes to produce the same outcome. To support our experimental findings, we identified a candidate network which, when modulated by afferent feedback reproducing the experimentally observed synergies.

3.4.3 Interneuron modelling of the CPG demonstrates changes in levels of afferent feedback are sufficient to alter synergy recruitment

The mechanism of action is hard to determine in a human spinal cord due to the lack of direct recordings from these circuits, but using MIIND, we built a population network model based on biological evidence to propose the likely mechanism of action. This simulation reproduced the same synergies as derived from the EMG data, changing the afferent input to the neural populations in this model, the synergy recruitment trends matched those observed with increasing internal knee angle. This model then demonstrates how muscle synergies can be encoded in neural population circuits and furthermore that synergy analysis of experimental data can be used to directly drive model development.

This model's similarity to previously studied spinal circuits supports conclusions that synergy encoding takes place in the spinal cord (Hultborn et al., 1987; Saltiel et al., 2001; Pierrot-Deseilligny and Burke, 2005; Dominici et al., 2011; Shevtsova et al., 2016). Supraspinal input was provided to the MN-RF motor neuron population and Extensor and Flexor Interneuron populations only and so specific bias e.g. in the antagonist muscles, was introduced through the circuitry of the model itself leading to the patterns observed in synergy 2. During this study, it became clear that altering the circuitry of the model (and the level of afferent input) mainly affected the activity of each motor neuron population at rest and its activity during maximal contraction. The contribution value of synergy 2 in the simulation was found to be inversely proportional to the difference between the maximal and minimal activity and this can also be observed in the experimental results.

We have thus demonstrated that a model based on well understood afferent inputs to spinal circuits that fits into existing CPG models of locomotion in cats, can be effectively used to predict synergies in simple isometric tasks in humans (Jankowska et al., 1967; Pratt and Jordan, 1987; McCrea and Rybak, 2008). This speaks to the robustness of the mechanisms in the model. In particular, it is clear that synergy 2 relies on the reciprocal inhibition between extensor and flexor populations which is also an important feature required for locomotion. What remains unanswered is firstly whether the cortical drive presented in this network bypasses the rhythm generation and pattern formation layers of the CPG, and if the extensor and flexor populations can be co-active when mediating a common drive to all muscles for voluntary tasks. Secondly, whether the full CPG model can be applied to understanding other cyclical limb motion like locomotion in humans.

Instead of using the traditional technique of direct simulation of individual neurons, we have instead used the MIIND simulation package, an environment allowing easy simulation of populations of neurons. It requires only the definition of connectivity at the population level, making it easy to setup and adjust a population network during development. Parameter tweaking is an inevitable part of the modelling process requiring cycles of adjustment followed by simulation. Reducing the need for adjustments to the neuron model itself was one reason why we used the simple exponential integrate and fire instead of a more complex Hodgkin-Huxley style neuron. This model was able to reproduce the desired synergy patterns without the need for the increased complexity of the Hodgkin-Huxley model. While building the network model we experimented with different connection configurations between populations. MIIND's XML style code, used to describe the network, made it simple to add, remove or adjust connections, as well as to add further populations for the RF and ST bias. For one dimensional neuron models, MIIND can simulate a population network with much greater speed than direct methods and this allowed simulations to be run on a local machine without the need for high performance computing, significantly improving the turnaround time between changing and testing the model. From our experience here, we advocate the use of simple neuron models where appropriate, i.e. reduce the dimensionality of the neural model as far as possible. First, this increases simulation speed and second, this focuses thinking on which are the essential neuronal mechanisms before simulation starts.

3.5 Conclusion

In conclusion, the comparisons between onset detection and synergy analysis methods found a moving average and NMF were fast and accurate ways of identifying synergy activity of interest. There was a clear effect identified of proprioceptive drive on the pattern of muscle synergy recruitment during a voluntary task. We propose a likely mechanism of action using a population model which reproduces the same synergy patterns as those observed experimentally, thus pointing to the spinal cord as the site for synergy encoding. Finally, this population network derived from earlier CPG models points towards the fact that spinal circuit components can act in both rhythmic tasks such as walking and in voluntary static tasks.

- A moving average window of raw signal amplitude was just as effective as more computationally intense methods of onset detection
- NMF was most accurate amongst synergy extraction methods
- All onset detection algorithms degraded synergy extraction accuracy

- Afferent feedback alters synergy recruitment in an isometric knee extension task
- The MIIND network successfully replicated the changes observed in experimental findings by integrating afferent feedback into a model of the CPG
- These findings challenge assumptions in the field regarding muscle synergy recruitment and the way these findings are analysed

Chapter 4: Control of stimulation paradigms using artificial neural networks to generate EMG waveforms in the rat hind limb

4.1 Abstract

Electrical stimulation of a motor nerve produces activity in the nerves it innervates. The relationship between the stimulation delivered and the resulting muscle activity follows a complex non-linear relationship which varies depending on the location and type of stimulus delivered. Whilst methods exist to establish the stimulus parameters required to excite a nerve these methods are time-consuming to translate into a predictive model and lack good generalizability. Furthermore, less has been done to examine precisely the effect stimulus parameters have on the resulting EMG waveforms particularly when stimulating at a more distant point on the nerve. The complexity of the problem is compounded by the presence of branching points within a nerve which mean that stimulation may recruit a range of muscles, some with more specificity than others.

Predicting the stimulus required to generate a specific waveform would allow a BMI device to selectively generate a wide variety of motor outputs. ANN's are particularly well suited for modelling this type of non-linear relationship with a good degree of generalizability. This series of experiments was designed to test whether an ANN could learn to predict EMG features for a given set of stimulation parameters applied to the sciatic nerve in the rat hind limb (n = 8). Cuff electrodes were attached to the sciatic and tibial nerve. Stimulation protocols were delivered to each cuff using the PulsePal 2.0 programmable stimulator varying the voltage and duration of the delivered pulse. These parameters were exhaustively combined to provide total coverage of the stimulation range. Motor response was measured using copper electrodes inserted into the muscle belly and via an ergometer attached to the Achilles tendon. EMG parameters were extracted from these signals and used to train an ANN. The EMG parameters of interest were SampEn, RMS, peak value and waveform length. Following training this ANN was then asked to predict the required stimulus pulse to generate a specific EMG waveform. When trained on the entire dataset the network successfully predicted the stimulation parameters required to generate a given dataset with an accuracy of 92%. To test the networks ability to generalize over the variability between different animals, the network was tasked with predicting the stimulation parameters for a subset (n = 1) of the dataset. In this case the network failed to correctly predict the pulse width, but still accurately predicts the pulse voltage. This may be due to a greater overlap in pulse width and resulting EMG parameters and that pulse voltage is the major determining factor in EMG

output. This algorithm provides a method for predicting and generating EMG waveforms without human supervision. This algorithm could be integrated into a BMI device to allow for targeted generation of EMG waveforms.

4.2 Introduction

There are well established methods for identifying the electrophysiological properties of a nerve, such as its activation threshold (Bostock et al., 1998). Most commonly these involve threshold-tracking wherein parameters such as the rheobase (minimum current amplitude required to produce a response using an infinite width pulse) or chronaxie (the pulse width which generates a response using exactly twice the rheobase amplitude) of a nerve are determined from strength-duration curves (Bostock, 1983; Mogyoros et al., 1996). By using these tools a variety of conditions affecting stimulation parameters have been examined such as membrane potential, temperature or myelination (Brismar, 1981; Bostock, 1983; Bostock and Bergmans, 1994). These features allow prediction of motor output for a given stimulus.

Similarly, there are models and experimental data available that allow for modelling of both single muscle fibres, motor units and whole EMG waveforms (Griep et al., 1978; Dimitrov and Dimitrova, 1998; Rodriguez-Falces et al., 2012). Whilst it is possible to generate detailed models of whole systems by combining these models into a larger simulation, this approach swiftly becomes extremely complex and specific to a given scenario. Adaptation to new scenarios is difficult and may require extensive amounts of new experimental work to validate. Machine learning algorithms are ideally suited to providing a degree of generalization to complex modelling problems, without having to generate a new model architecture by hand.

Through further understanding of the electrophysiological properties of nerve and muscle fibres it is hoped that new treatments for spinal cord injury may be possible via stimulation of nerve fibres (Liberson et al., 1961; Moe and Post, 1962; Ho et al., 2014). Stimulation of interneuron pools in anaesthetised frogs, turtles and mudpuppies have demonstrated recruitment of complex movements or force vectors in multiple muscles (Saltiel et al., 1998; Tresch et al., 2002). FES has also shown promise in encouraging recovery of neural pathways when combined with exercise in humans (Field-Fote, 2001; Kapadia et al., 2014). However, for a BMI device to restore motor control, further difficulties must be overcome. The BMI device must be capable of modelling the response of muscles separated by some distance, potentially across multiple branching points within a nerve.

Ideally this system would able to account for the variability between subjects and be flexible enough to transfer between different stimulus sites. This chapter demonstrates that some of these difficulties can be overcome using ANNs. The ANN developed and presented here successfully models EMG output resulting from electrical stimulation of the sciatic nerve in the rat hindlimb and produces accurate generalizable predictions of stimulus parameters.

4.2.1 Current methods of tuning stimulation parameters lack specificity and are difficult to automate

Electrical stimulation has been used therapeutically at every level of the nervous system; stimulation of the cortex for treatment resistant epilepsy or Parkinson's disease, surface level peripheral nerve stimulation for foot drop and at the level of the spinal cord to help rehabilitation following spinal cord injury (Field-Fote, 2001; Benabid, 2003; Kapadia et al., 2014; Daly and Huggins, 2015; Chang, 2018; York and Chakrabarty, 2019). In spite of this widespread usage a common limitation to all approaches is a high degree of variability between patients. This necessitates individual adjustments for each case or patient and the expertise of the operator performing this turning of stimulus parameters can significantly affect the effectiveness of the treatment. The choice of stimulation parameters is often adjusted ad-hoc as the stimulus/response relationship changes over time due to any number of factors, including injury recovery, electrode decay or at a shorter scale due to fatigue. The limitations in traditional methods are particularly problematic in the field of BMI devices where the requirements for fine tuning can be amplified, requiring adjustments every time the device is used. A more effective solution requires an automated method that can cope with the differences between subjects. In this regard the field of machine learning may hold the answer with novel application of ANNs.

4.2.2 Machine learning algorithms are ideally suited to solving nonlinear problems with incomplete knowledge

ANNs are modelled, at least in principle, to reflect similar principles of learning as observed in their biological equivalents. Several features of the ANN learning process make them well suited to the problem in hand. ANN’s learn through an iterative process of updates across thousands of connections between nodes of the network. The number of connections and nodes means that an ANN can model functions with a large number

of variables which allows them to model highly non-linear functions. The iterative update process provides a method for easily updating the ANN in relation to new data or to changes in the original conditions; the network is simply re-trained on the new data. ANNs are also “black-box” solutions, in other words they do not require significant pre-existing models of the system in question, simply large quantities of related data. This comes with drawbacks, as it is not possible to understand precisely how the algorithm comes to a particular output. However, they also exhibit a startling ability to generalize from data they have observed to unknown circumstances. To summarize, ANNs provide a means of modelling non-linear, variable relationships with the capability to generalize across intersubject variability and to unknown conditions, provided the training dataset is of sufficient quantity and quality of data. Therefore, they may be able to overcome the difficulties previously described in modelling the transfer function between nerve stimulation and motor output.

Other attempts have been made to use ANNs to control nerve stimulation. These methods have varied in how they define their input and how they measure output. Some algorithms use fixed stimulation patterns without the capacity to provide fine-tuned control (Lan et al., 1994). Many algorithms use kinematic signals instead of EMG waveforms as the input data (Riess and Abbas, 2000; Prentice et al., 2001; Hincapié et al., 2005; Hincapie and Kirsch, 2009). Others have examined stimulating a limited number of muscles (Giuffrida and Crago, 2005). In comparison to previous work the network shown here has focused on increased detail in control over stimulus parameters and using EMG signals recorded across multiple muscles. The granularity in selection of stimulus parameters should allow for greater specificity in recruitment of EMG waveforms.

4.2.3 Experimental rationale

The aim of this chapter was to establish if an ANN could model how stimulation of the sciatic nerve relates to activity in LG, MG, EHP, EDL and TA muscles. Recordings were made from 8 male Wistar rats following stimulation of the sciatic nerve, as well as tibial stimulation in a subset of 2 rats. It was expected that stimulation of the sciatic nerve would result in recruitment of all the recorded muscles. The addition of tibial nerve stimulation was to allow for selective recruitment of EHP, EDL and TA. Difficulties were faced in recording all muscles simultaneously and therefore it was not possible to demonstrate this selectivity comprehensively. Tibial stimulation was therefore not

analysed further within the ANN. The threshold response in the animal where tibial stimulation was successful is available in the Appendices where the difference in selectivity between stimulation sites is apparent.

LG, MG, EHP, EDL and TA were selected for recording for two reasons. Firstly, these muscles share common innervation in the form of the sciatic nerve; but LG and MG, and EHP, EDL and TA are separated by a branching point in the sciatic where the sciatic becomes the tibial and peroneal nerves. The tibial goes on to innervate LG and MG whereas the peroneal nerve goes on to innervate EHP, EDL and TA (by later branching again into the deep fibular nerve which directly innervates EHP, EDL and TA). This gives a distribution of muscles to examine with varying distance from the stimulation site, which will highlight the networks ability to selectively recruit certain muscles. The second reason was due to the ease of surgical access, both to the muscles themselves and the innervating sciatic nerve.

Stimulating the sciatic nerve limits the transfer function to the lowest level of the CNS. The peripheral nervous system provides a wide range of parameters the ANN must account for to achieve accurate stimulus prediction. These include the stimulation provided (which itself has the sub parameters of voltage, current, phase, length or width of pulse and pulse shape), the site of stimulation, the stimulating apparatus and changes in the output across the stimulation paradigm. The stimulating apparatus was kept the same and concerted effort was made to keep the surgical set up consistent between animals. The stimulation paradigm was designed to cover both minimal i.e. no response and maximal response within the resolution of the PulsePal device. The saturation point for the muscles under examination was determined through exploratory stimulation through which it was determined that saturation occurs at approximately 2V and 2000µs, so this was determined to be the maximum values for the stimulation paradigm.

To ensure that the response to a set stimulus was the same across the experiment, the response to a fixed test pulse (200 µs - 5000mV) was recorded throughout the stimulation paradigm. If the response to the test pulse changed this could be accounted for by normalizing to the calibration curve generated. The effect of muscle length on the response was also accounted for by determining the maximal response to stimulation across a range of muscle lengths. Correcting and accounting for these factors should mean that the only difference between EMG waveforms is due to differences between animals, and due to the stimulation parameters. Therefore, this dataset will test the

ANN's ability to model these stimulation parameters as well as its ability to generalize the variability of each animal's response.

Parameters describing the EMG waveforms shape were the input to the ANN. These parameters need to describe the waveform well enough that they distinguish two different waveforms as being different. For sufficient specificity between waveforms four parameters were chosen for extraction and training; max amplitude, waveform length, RMS and SampEn. These measures have previously been demonstrated to provide a high degree of accuracy in classification of EMG waveforms (Phinyomark et al., 2013). Therefore, these parameters should provide sufficient detail for the ANN to distinguish between different waveforms across the dataset.

The accuracy of the network's prediction of stimulation parameters was examined using the entire dataset of 8 animals. The accuracy of the network is simply measuring how often the network's prediction matches the true value for the entire dataset. This was then compared to its performance predicting an unseen animal, which was achieved by retraining the network on the same dataset with one animal removed. The network was then asked to make predictions on the removed animals EMG output. The results of this prediction suggest that ANNs are capable of modelling a generalizable transfer function for electrical stimulation of the sciatic nerve that accounts for factors such as inter-animal variability, non-linear and differential threshold responses.

4.3 Results

During the stimulation experiments 5 muscles were recorded from (MG, LG, EDL, EHP and TA) during stimulation, however TA was discarded from the training dataset as none of the recordings were deemed of sufficiently SNR. Difficulties were faced in achieving high quality recordings from each muscle in every animal, and in achieving high SNR EMG and ergometer recordings at the same time. EMG recordings tended to be best for pairs of muscles, EDL and EHP and MG and LG. These problems can be put down to the long time period required for the surgical set-up and the stimulation paradigm (>3hours). This precluded multiple recording attempts from one animal as it placed animal welfare at risk. This time pressure was amplified in the cases of tibial stimulation as the time required for stimulation was significantly increased (one recording session required 7.5 hours). Therefore, it was decided to focus on sciatic stimulation for the remaining animals as a trade-off between the time required and to maximise the opportunity to record high SNR recordings of the muscles under investigation.

A representative set of EMG signals from each muscle and the ergometer reading in response to the test signal (200 µs – 5000mV) is available in the appendices. The response to threshold (T), subthreshold (0.5T) and suprathreshold (2T) stimulation is shown in Figure 4-A. It should be noted that these responses were not recorded separately, they are part of the normal stimulation paradigm, and are therefore included in the ANN training dataset. Successful training would indicate that the ANN has learnt in some way how the nerve responds to different stimulus in relation to these threshold values.

4.3.1 Calibration for muscle length and changes across the stimulation paradigm

Calibration curves were calculated so that the EMG parameters could be corrected for. changes across the simulation paradigm by normalizing to the value of this curve across the dataset. The calibration curves were calculated from the test pulses delivered at every 100th stimulation point. As can be seen in Figure 4-B these calibration curves are different for each muscle. LG appears to decrease in max amplitude, RMS and SampEn. The SampEn of MG also appears to have a “hump” in its response, peaking during the middle of the stimulation protocol. Calibration curves were also calculated for changes in the length of the muscle. This value was determined experimentally in one animal (rat 1) by repeated stimulation with the test pulse at a range of muscle lengths. The

responses to stimulation at different muscle lengths are shown in Figure 4-C, and the optimal length was found to be 33.5mm.

4.3.2 EMG parameters response to stimulation is a complex non-linear relationship

The mean values for each EMG parameter across the total stimulation paradigm can be seen in Figure 4-D. The relationship between stimulation width and voltage is unclear from these values. The relationship is different for voltage and width, and for each muscle. There appears to be linear phase in the response to increasing voltage in most muscles. This linear phase is most clear in the max amplitude of EHP which follows a clear increase in max amplitude as the voltage of the stimulation pulse increases. The max amplitude of the other muscles reaches saturation point at much lower voltages, in particular LG and MG have a very sharp rise to saturation, whereupon the increase in voltage only results in a small increase in max amplitude. EDL is a mixture of the two with an almost sigmoidal response in max amplitude, quickly reaching a saturation point at a given threshold. The effect of width on max amplitude appears minimal which can be seen as each “triangle” of responses in max amplitude are very similar. RMS appears to share features with the max amplitude, as would be expected mathematically. EDL and EHP show a linear increase in RMS response to increased voltage whereas pulse width does not appear to have a significant effect on RMS. LG and MG appear to reach the same saturation in RMS response as observed in max amplitude. Initially width appears to have no effect, but at approximately 900 µs RMS drops significantly before beginning to rise again with increase in voltage and width. This same change is observed in the waveform length of the signal for MG and LG. The waveform length of EDL and EHP shows a more linear response than the other parameters and it is unclear if saturation occurs for this parameter within the stimulation range tested. The SampEn for each parameter appears to follow an inversion of the previous patterns, as SampEn decreases with increasing voltage. Furthermore, the same change in response at 900 µs is observed for LG and MG. Each parameter investigated and each muscle appears to demonstrate linearity in its response at certain points in the stimulation paradigm. However, the response of the dataset as a whole is non-linear due to the presence of saturation points and the variability in the responses of individual muscles.

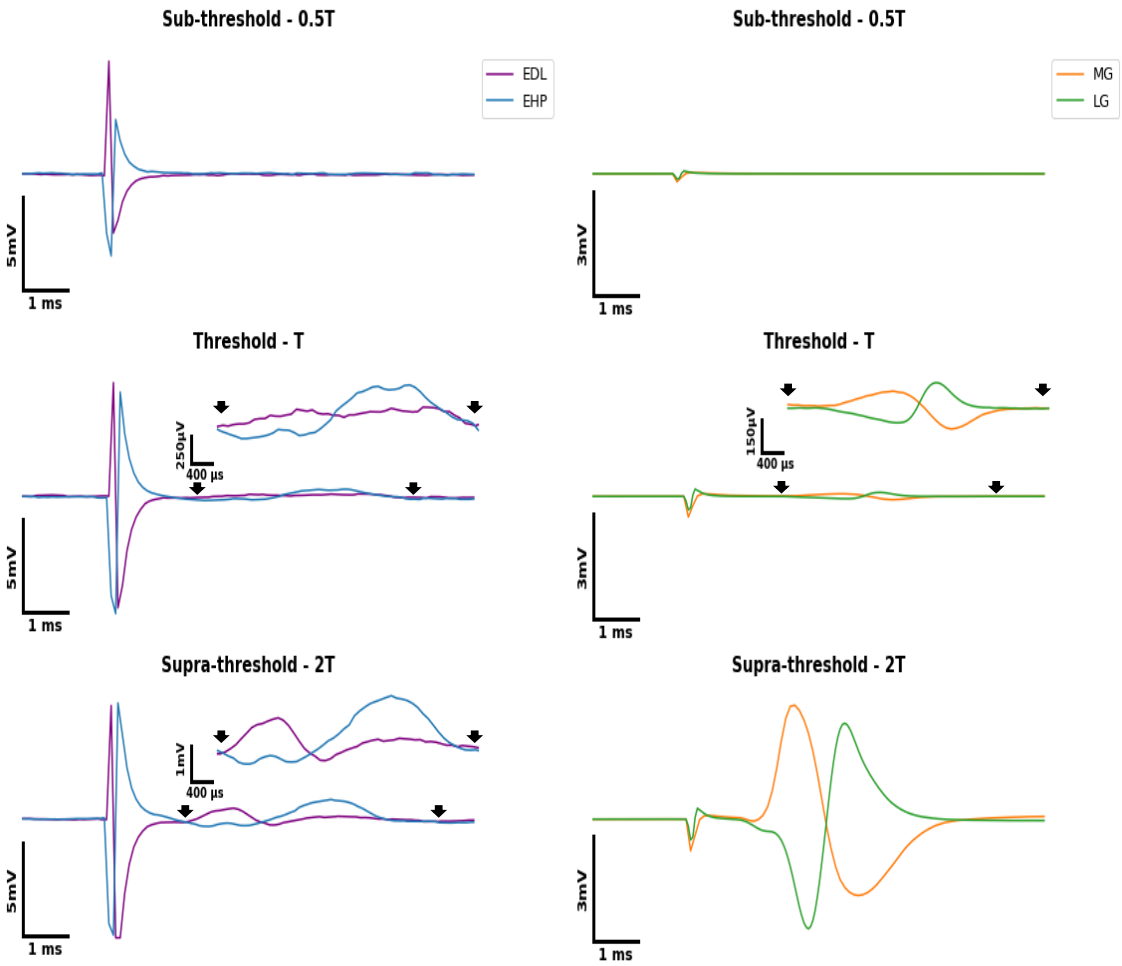

Figure 4-A: **Representative examples of sub threshold, threshold and supra-threshold signals.** Signals are representative pairs selected from rat 2 (LG and MG) and 4 (EDL and EHP). Recordings were taken from EDL, EHP, LG and MG via copper wire inserted into the muscle belly. Where an inset trace is provided it is the activity of interest of the muscle pair between the points indicated by the black arrows, increased to a scale for easier visual analysis. Threshold is defined as the shortest, smallest pulse that elicited a response; in this case the threshold was 100 µs – 600mV for EDL and EHP and 100 µs – 400mV for LG and MG. Sub threshold signals are stimulus pulses that failed to elicit a response, the pulse shown here is 100 µs – 300mV and 100 µs – 200mV respectively, or half the threshold value. Supra-threshold values are signals that are above threshold and are presumed to be near the saturation point in their response. This is represented here with a stimulus pulse twice the voltage of the threshold response, 100 µs – 1200mV.

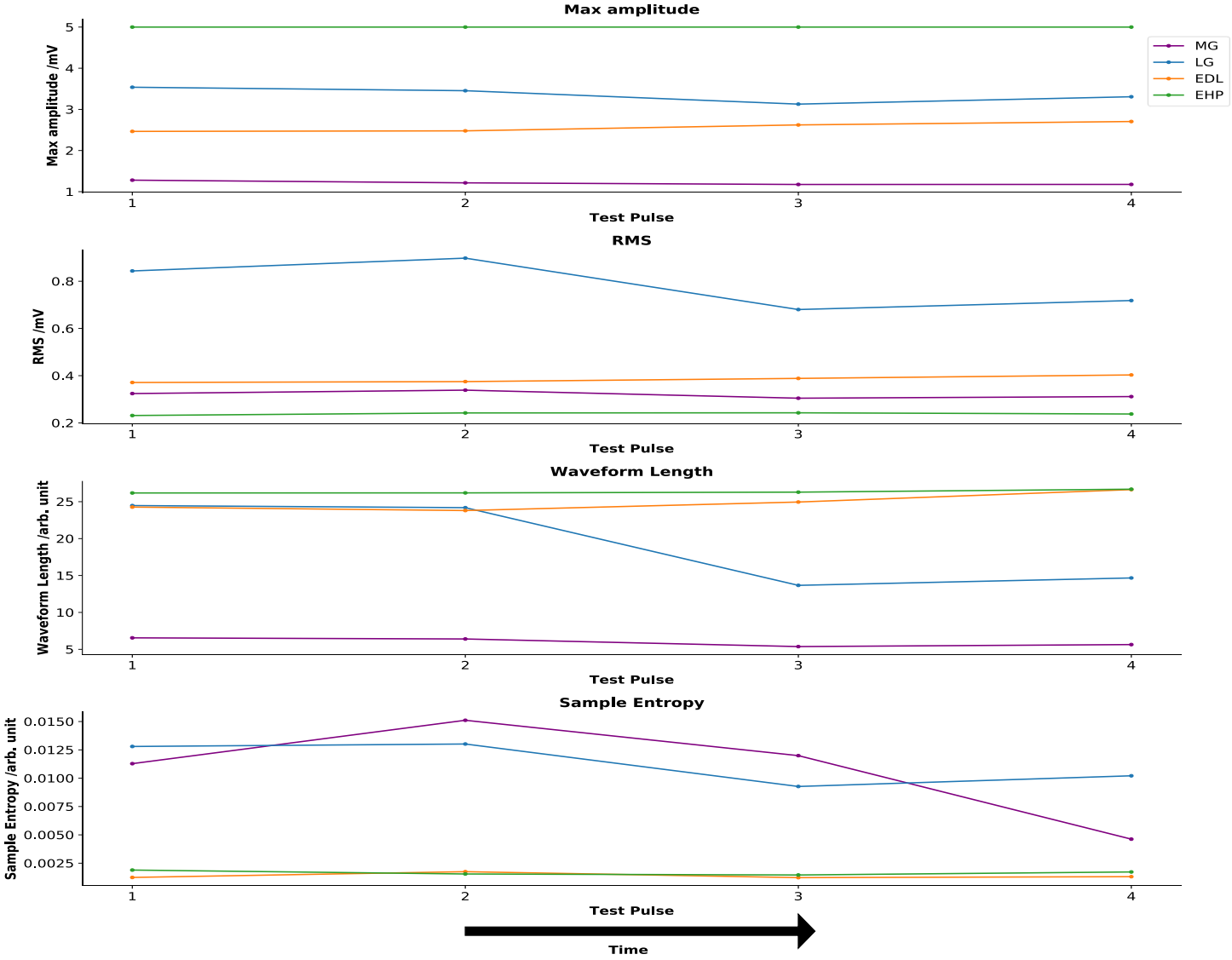

Figure 4-B: **Change in response to test pulses for each muscle across the stimulation paradigm.** Four parameters were used to train an artificial neural network to predict how stimulation results in EMG waveforms, max amplitude, root mean square (RMS), waveform length and sample entropy. To correct for changes that occurred across the stimulation paradigm a test pulse was delivered at the start and end of the paradigm and every 100 pulses delivered. The test pulse delivered consisted of a balanced biphasic square wave (200 µs - 5000mV). Changes in response to the test pulse can be calculated and corrected for during training by normalizing to this correction curve.

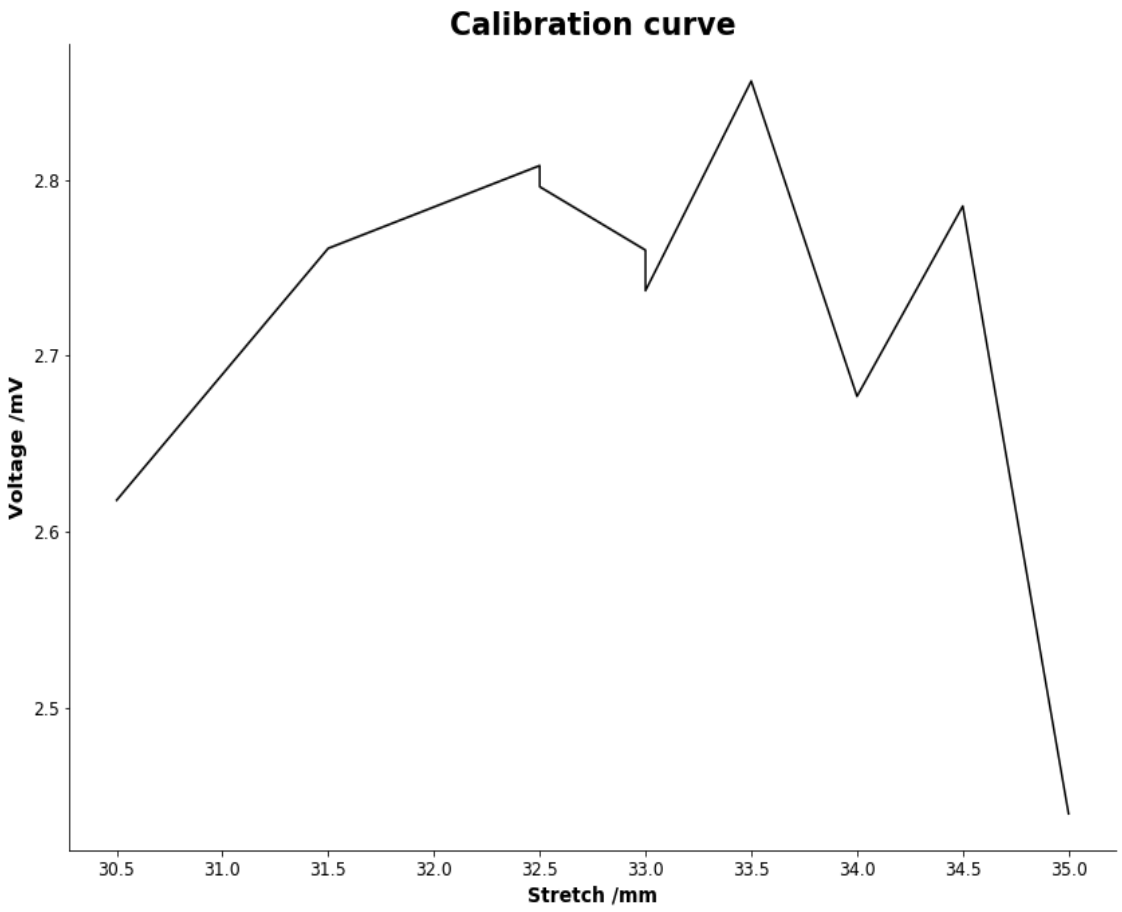

Figure 4-C: **Calibration curve for changes in output due to muscle length.** Ergometer response was calibrated to the length which produced the maximum response to a test pulse of (200 µs - 5000mV). The ergometer measured gross motor output due to stimulation via a metal ring attached to the Achilles tendon. Test pulses were delivered, and the output of the ergometer was measured between 30.5mm and 35mm measured using microdrive values on the stereotaxic apparatus that the animal was placed in.

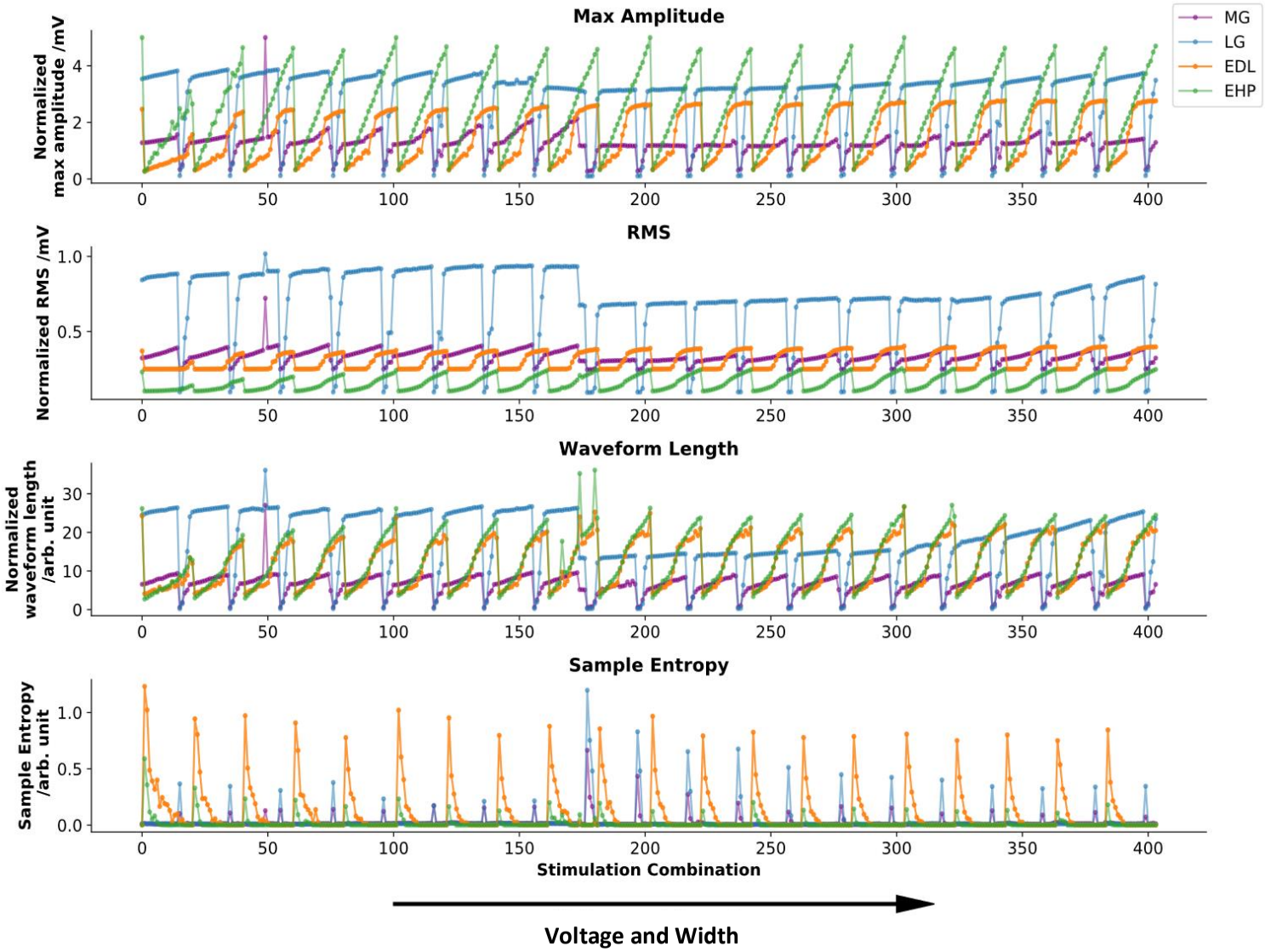

Figure 4-D: **Mean values for the four values used for artificial neural network training.** The four parameters included in the dataset are max amplitude, root mean square (RMS), waveform length and sample entropy. These parameters were extracted from the extensor digitorum longus (EDL), extensor hallucis proprius (EHP) medial and lateral gastrocnemius (MG, LG). Parameters were averaged across 8 animals (incomplete values for each muscle). Each value was normalized to the maximum value across the dataset. Response to test pulses are included within this dataset alongside the stimulation paradigm

4.3.2 Network training successfully predicted EMG parameters in known and unknown conditions

The network training results for the entire dataset ($n = 8$) are shown in Figure 4-E and can be observed to reach a local minimum without overfitting. Predictions of the network based on the training data set are shown in Figure 4-H. The accuracy for this network when trained on 8 animals and 75% of the data is 92% for the test dataset and 93% for the validation data set. This demonstrates that the network has accurately modelled the relationship between stimulation parameters and EMG parameters. When the network was trained on 7 animals and given an unknown animal to predict training accuracy reaches 82% for the test date set and 78% for the validation data set. The training curve for this subset is shown in Figure 4-F. The results from the prediction on an unknown animal are shown in Figure 4-H from which it can be observed that the voltage prediction is again extremely accurate whereas the width prediction has become inaccurate. To further examine why the width prediction is inaccurate the summed variance of EMG parameters was compared across pulses with equal voltage and with equal. Pulses with equal voltage had a summed variance of 12.17 and pulses with equal width had a summed variance of 7.2. The difference in summed variance indicates that pulses with equal voltage were more similar to each other than pulses with equal voltage.

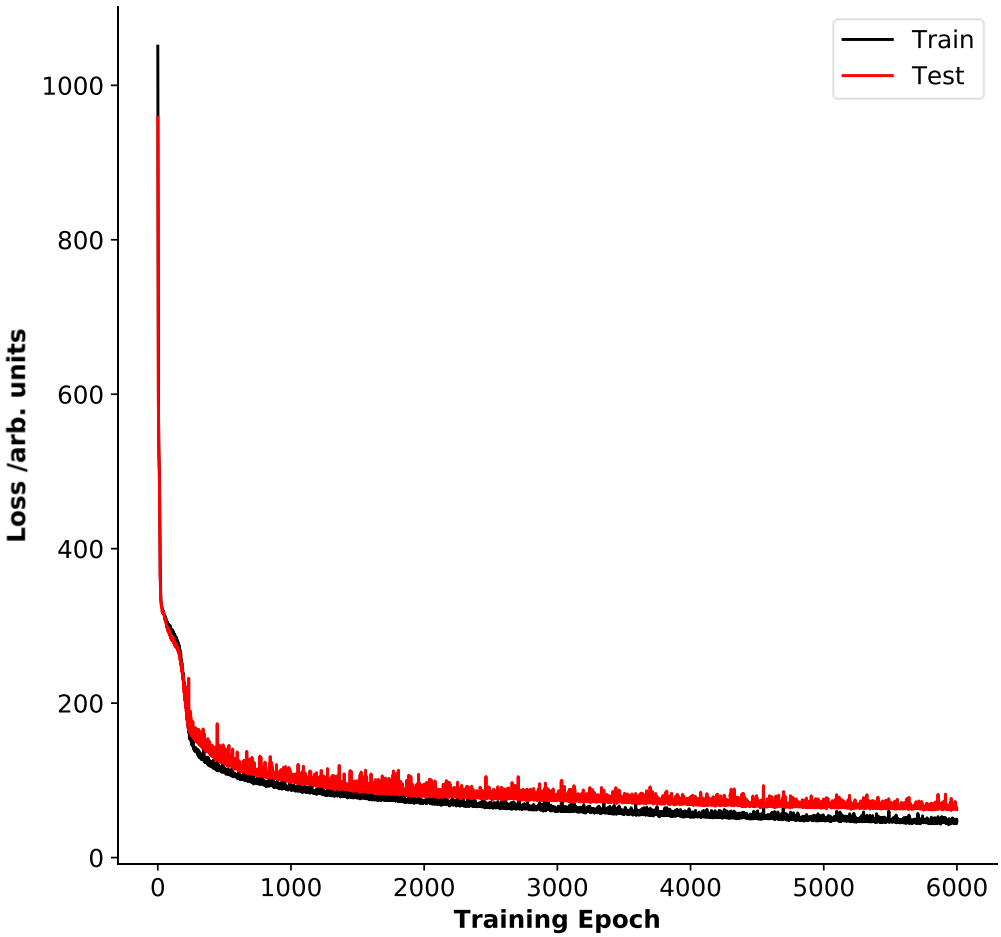

Figure 4-E: **Artificial neural network performance across training epochs on a complete dataset**. Dataset consists of stimulation parameters and resulting EMG parameters in the rat hindlimb ($n = 8$). Loss is measured using the binary cross-entropy between the target value and network output. To detect overfitting network performance is measured using two datasets, the train dataset which consists of data the network has been trained on, and test which is data the network has not previously seen (black, red, split of 0.75/0.25 between train and test datasets). Overfitting occurs when the performance on train and test differs substantially or when test ceases to improve. In this graph overfitting starts to be detected at approximately the 3000th epoch but performance continues to increase on both datasets until the end of training.

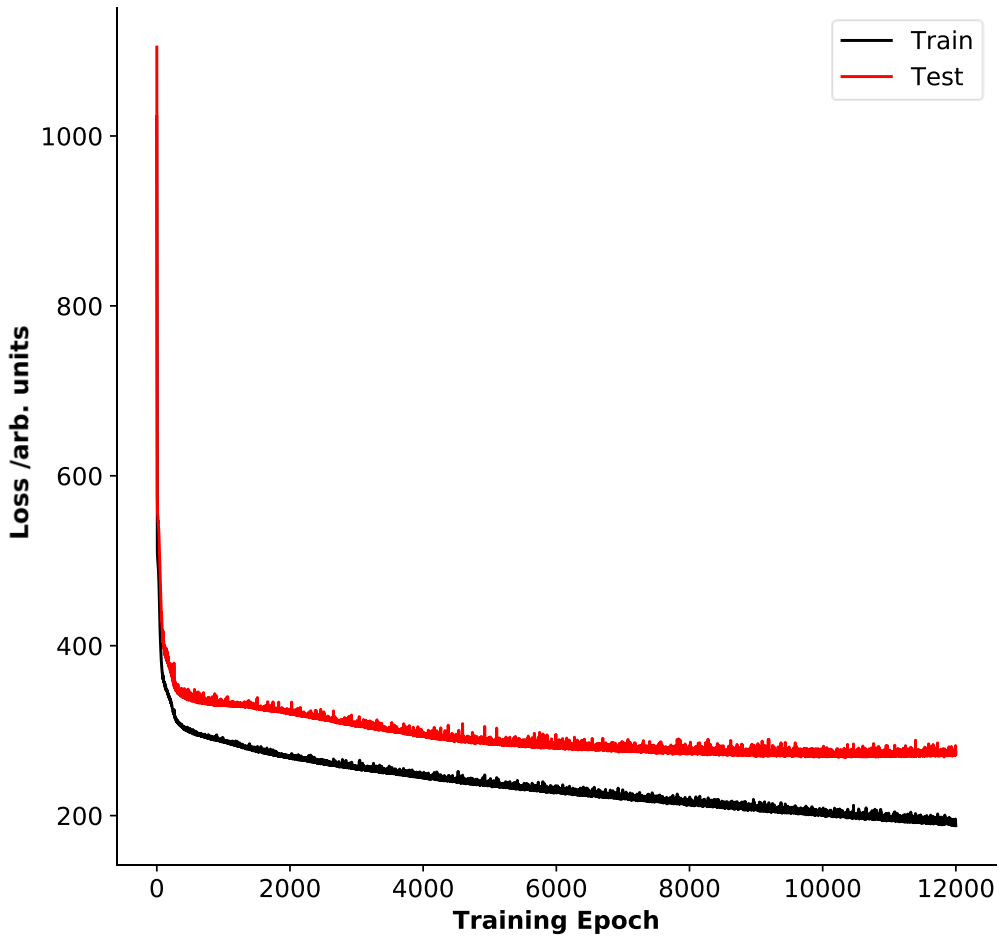

Figure 4-F: **Artificial neural network performance across training epochs on an incomplete dataset**. Dataset consists of a subset of stimulation parameters and resulting EMG parameters in the rat hindlimb (n = 7). One rat was removed from the dataset to allow prediction of a completely unseen set of EMG recordings. Loss is measured using the binary cross-entropy between the target value and network output. To detect overfitting network performance is measured using two datasets, the train dataset which consists of data the network has been trained on, and test which is data the network has not previously seen (black, red, split of 0.75/0.25 between train and test datasets). Overfitting occurs when the performance on train and test differs substantially or when test ceases to improve. In this case overfitting is apparent early in training due to the gap between train and test curves. Both curves continue to improve across training. The gap suggests that the train dataset has insufficient training data to fully learn the features in the test data.

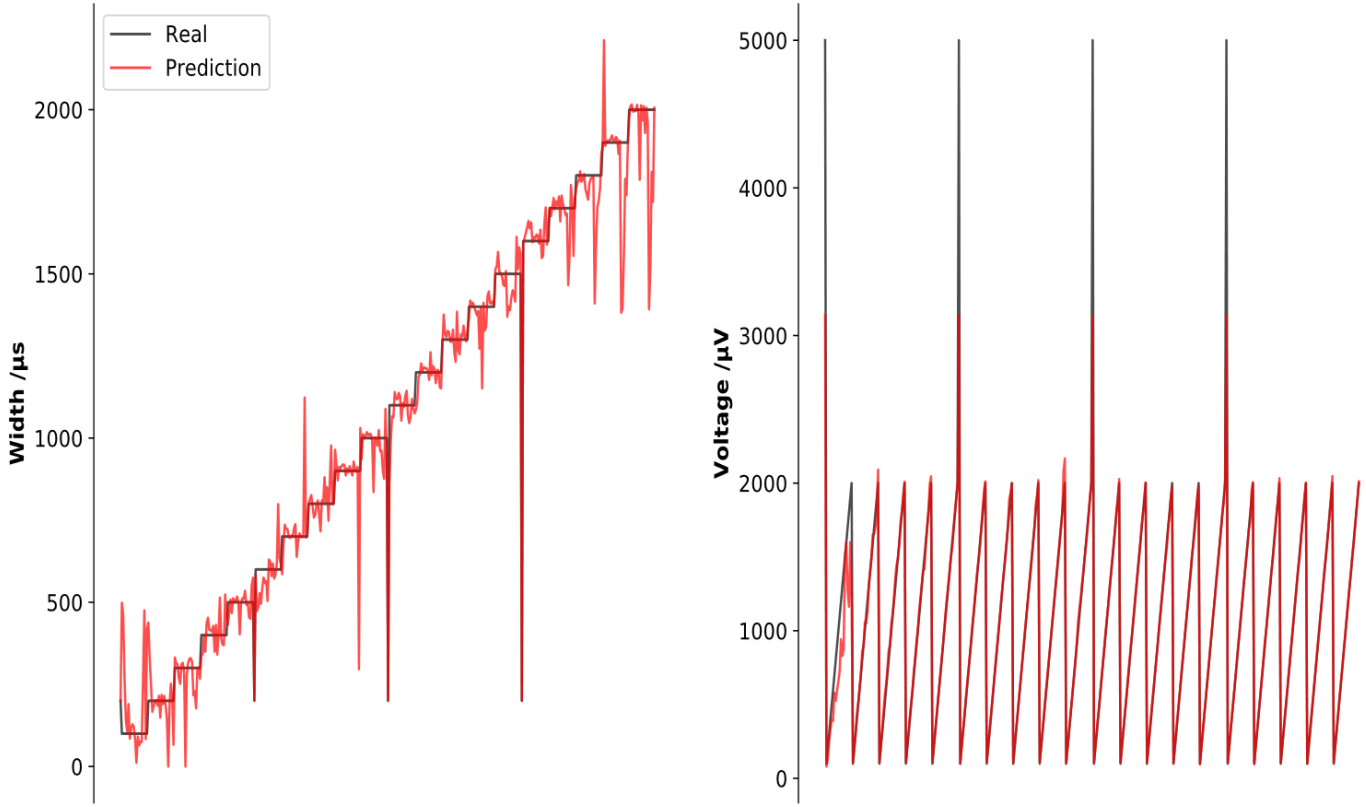

Figure 4-G: **Network prediction of pulse parameters on training dataset (n=8, variable contribution for each muscle).** (LEFT) Network prediction of pulse width versus actual pulse width (red, black). (RIGHT) Network prediction of pulse voltage versus actual pulse voltage (red, black). X-axis corresponds to stimulus pulse number (equivalent to order), not shown for clarity.

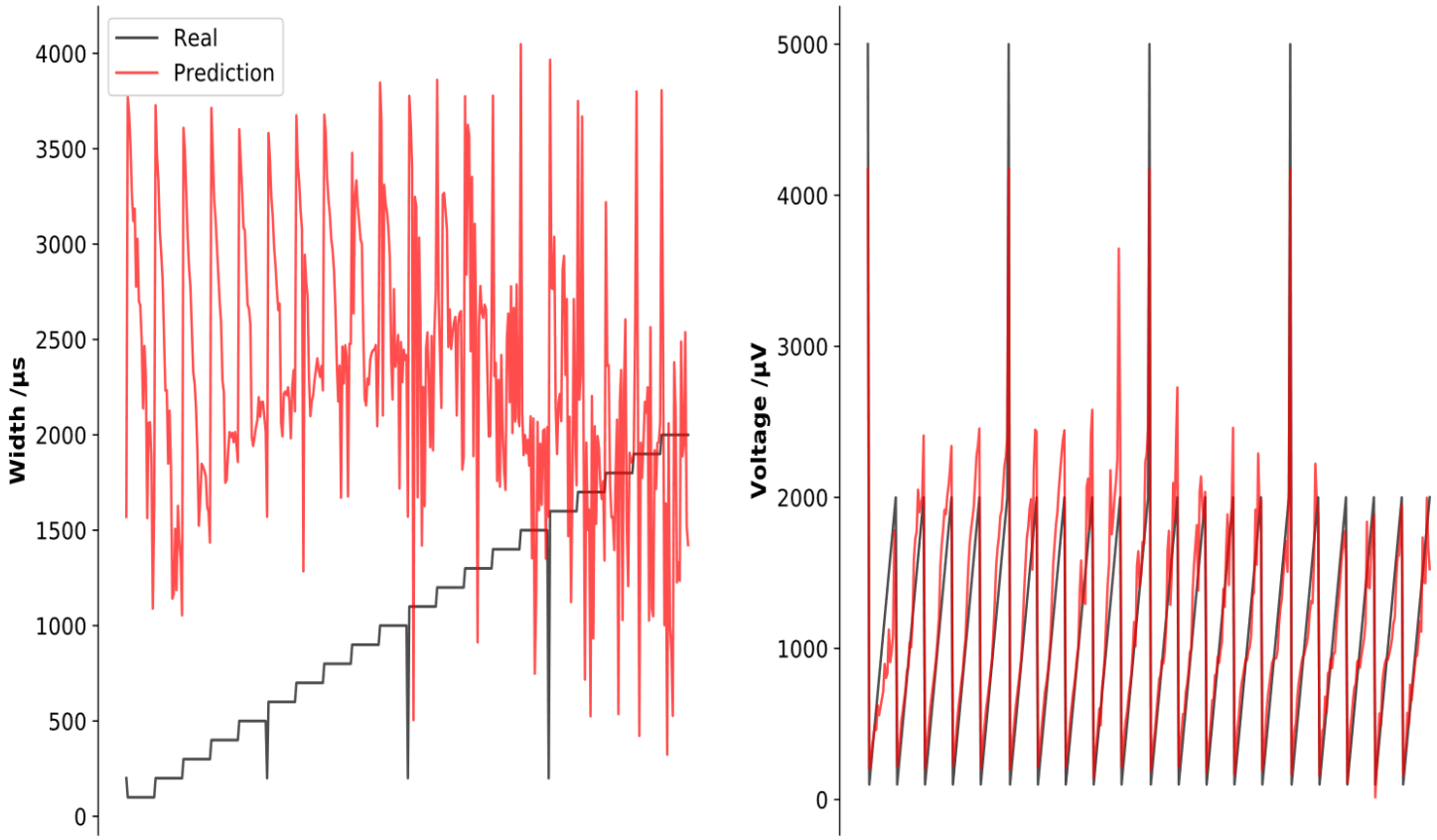

Figure 4-H: **Network prediction of pulse parameters on unseen dataset of one animal (training n=7, variable contribution for each muscle, prediction dataset n=1).** (LEFT) Network prediction of pulse width versus actual pulse width (red, black). (RIGHT) Network prediction of pulse voltage versus actual pulse voltage (red, black). X-axis corresponds to stimulus pulse number (equivalent to order), not shown for clarity.

4.4 Discussion

The success of the network in predicting the results of stimulation of the peripheral nerve demonstrates that an ANN can learn a representation of a generalized transfer function between electrical stimulation and motor output. This is in spite of the clear non-linearity and variability present in the recorded EMG parameters across muscles and animals. This performance is capable of impressive results both in the “known” representation and when tasked with predicting unseen data. This method provides several improvements over current methods for stimulation control, such as pre-defined stimulation thresholds or threshold tracking, as it provides precise control over the EMG waveforms generated in an automated fashion. Compared to control by a predefined stimulus paradigm this method has greater generalizability and can fit into an entirely online process with very little adjustment. Furthermore, compared to a method using predefined parameters, this method has greater specificity and adaptability as it allows fine tuning of stimulation parameters as conditions change.

In the unknown condition the network is still capable of predicting the voltage of the stimulation pulse, but accuracy drops sharply on width prediction. This drop-in performance could simply be due to insufficient data as the dataset used for these experiments was already very small by traditional machine learning standards (datasets for complex language processing tasks can easily number in the millions and even billions). However, this could also reflect a greater importance for pulse voltage in determining EMG output in this circumstance. This is reflected in the lower summed variance of EMG parameters with equal pulse width compared to equal pulse voltage. This would suggest an overlap between EMG waveforms with equal pulse width. In combination with other points among these findings this suggests that the network has truly learnt a transfer function capable of generalizing between different conditions and subjects, as opposed to a more specific overfitted function.

4.4.1 EMG parameters demonstrate non-linearity across muscles

There has been extensive work done in the peripheral nervous system examining the motor response to electrical stimuli. (Fang and Mortimer, 1991; Singh et al., 2000; Lertmanorat and Durand, 2004; Sauermann et al., 2007; Raikova et al., 2016). However, the nervous system defies systematic treatment of the problem. The values shown in Figure 4-D demonstrate some of the problems faced by any motor BMI in the variable response of muscles to stimulation. Consider the differences in maximum amplitude between the pairs of muscles LG and MG and EDL and EHP. As expected, LG and MG closely mirror each other and as seen in table 2-B it was not possible to selectively recruit LG or MG, likely due to limitations in the resolution of the PulsePal stimulator. LG and MG show a high degree of sensitivity to stimulation at the point chosen and they saturate quickly as voltage increased. However, at a certain point (approximately starting at pulse widths greater than 900µs) this saturation point drops in RMS, waveform length and SampEN but not the max amplitude. This pattern is not apparent in EDL and EHP, but as can be seen in the max amplitude of these muscles, as well as in Table 2-B and the appendix figures, it was just possible to selectively recruit EHP before EDL within the resolution of the PulsePal stimulator. Indeed, EHP is the only muscle examined that did not consistently reach a saturation point in all animals, with clear triangular shape to its stimulus/response curve in maximum amplitude that is still increasing in response to the test pulses (200 µs – 5000mV). In comparison its partner EDL does appear to saturate in amplitude, demonstrates a greater RMS than EHP but then is a mirror image of it in terms of its waveform length. Finally, these patterns are inverted when examining the SampEn of each muscle. What can be ascertained from all of this variability in response? There is a linear section to the response of each parameter, but this section does not cover the entirety of the response in any muscle, except EHP's max amplitude. This is compounded by the variable response for each muscle, which means that when the dataset is considered as a whole the responses are highly non-linear. A traditional model may be able to account for some of these non-linearities, but machine learning has distinct advantages when modelling non-linear functions.

4.4.2 An ANN learnt a generalized transfer function for electrical stimulus in the peripheral nervous system and resultant EMG activity

The performance of the network on the full dataset of animals is remarkably good, demonstrating a nearly perfect prediction of voltage and width across the stimulation range, as seen in Figure 4-G. Width prediction falls in accuracy at the start and end of stimulation, whereas voltage predictions are almost universally accurate, with the exception of the test pulses of which only 4 examples are present in every dataset. If test pulses are removed as outliers voltage prediction is almost perfect. The ANN developed here is provides as a method for fine-tuned control of stimulation parameters with motor output as a target, a claim that will be demonstrated in later chapters. However, limiting the discussion to the results so far, the performance of the network must be further scrutinized to ensure it has utility beyond the specific circumstances described here.

In any machine learning task, it is important to ensure that the fit of the model is correct. Underfitting is easy to detect, the network's performance is simply deemed to be poor for whatever purpose it is required for. Overfitting is more difficult to define. An overfitted network may produce excellent predictions on the data it is trained on but then give nonsense answers when exposed to even slightly different data. This is a failure of the network to generalize in a way that largely invalidates its usefulness. A model is only usually useful if it can predict things about data that is unseen, as by definition this shows something new. Partitioning of datasets is one way to demonstrate that a network has not overfitted. In all cases during this study the dataset was split into training and test datasets at a 3:1 ratio. If the performance differs significantly between training and test datasets this can be an indicator that the network has overfitted. As seen in Figure 4-E the difference between test and training datasets has only begun to diverge at 6000 training epochs, and both training curves were continuing to improve gradually at this stage. On its own this would suggest that the network has learnt to generalize across the values it has observed. However, the performance on an unknown animal is even more promising in this regard. While partitioning of test and training datasets does remove some of the information from the model, it is likely that the overall "shape" of the relationship is maintained for each animal. As can be seen in Figure 4-F removing an animal from the dataset has introduced a certain degree of overfitting but this is still within acceptable levels.

The 82% test accuracy and 78% validation accuracy for an entirely unknown animal suggests that the generalizability of the relationship learnt is sufficient to be of predictive

use in new subjects. As can be seen in Figure 4-H the network is still able to successfully predict stimulus voltage, but not width. The “prioritization” of the voltage of the pulse is the same feature that a human would identify as important when attempting to model this relationship. This insight into the working of the model gives greater confidence to its predictive capabilities if it were given a dataset of a size more usual for machine learning tasks. Whilst it is a truism in machine learning that performance increases as dataset size increases, here it seems especially true that even a modest increase could provide useful improvements.

4.5 Conclusion

The network design shown here was intended to control the output portion of a BMI device for stimulating various areas of the CNS. To achieve this the network needed to learn a transfer function between stimulation at one point and motor output measured at another. The network was trained to predict the EMG parameters resulting from different pulse voltages and widths delivered to the sciatic nerve in the rat hindlimb. This prediction was made with a high degree of accuracy in the complete dataset. In the subset of the dataset network performance dropped but was still capable of accurately predicting the voltage parameter. The networks performance on an unseen animal suggests that the network can generalize its results from one environment to another. This idea will be further explored in the following chapter using an *in silico* simulation.

- Stimulation of the rat sciatic nerve produces a complex non-linear response in muscles of the rat hindlimb
- An ANN was able to learn the stimulus/response relationship for stimulation of the sciatic nerve
- The ANN was able to transfer learning from the group of animals it was trained on to an unseen animal, indicating successful generalization of the transfer function
- These results suggest that ANNs may be capable of learning a generalized transfer function for stimulus/response of a nerve. This presents great opportunity for more flexible and adaptable devices capable of treating a wider range of injury types.

Chapter 5: Closed-loop reconstruction of healthy muscle synergies using a population model of cortical and peripheral injuries

5.1 Abstract

Experiments investigating the effects of damage to the nervous system face technical and ethical difficulties. Using the MIIND network, demonstrated in Chapter 2.6, in this chapter, an *in silico* model of acute peripheral and cortical damage to the nervous system is presented. The synergies extracted from these injured networks demonstrate the same hallmarks of synergy "injury" that are typically observed in injured human subjects; fractionation and merging of existing synergy profiles. Having shown that the injury model reflects real world conditions it was then asked if the algorithms previously described in Chapters 3 and 4 could restore healthy synergy recruitment as had been suggested. The same ANN architecture that was used to learn a transfer function in the peripheral nervous system was similarly trained on data from the simulated model. Stimulation was provided at different points depending on the injury type. In cortical injury models only the damaged interneuron pool was stimulated, whereas for the peripheral injury models the motor neurons were also directly stimulated. Motor response was measured using motor neuron output as a correlate for EMG signals. In this case network training was able to converge to an accuracy of 98% as simulated datasets can be made arbitrarily large by repeated runs of the model. Following this training the network was asked to predict the EMG output that would result from healthy synergies. This prediction was then input into the simulated network and the response observed. In the case of cortical injury, the network was successfully able to restore healthy synergy recruitment profiles. This performance was not replicated for the peripheral injury, with the network being unable to restore healthy synergies in the absence of afferent feedback. This may be a failure of the ANN to address the increased complexity of the MIIND network or it may be further evidence for a special role of afferent signals in synergy recruitment as indicated in Chapter 3. This set of simulations and experiments demonstrate the combined utility of this thesis's work as the flexible basis of a BMI device for the treatment of nerve injury in a variety of conditions.

5.2 Introduction

When investigating damage to the nervous system, whether it be spinal cord injury or a peripheral injury, often the choice is limited to either human subjects or an animal model. A simulated model of various injury types would be a useful alternative to biological

models. Simulations have increased flexibility and ease of use compared to biological models and are better able to focus on specific areas of interest in greater detail. For example, in a model it is possible to examine very specific removal of certain pathways or tracts. In comparison to an impact injury model it is impossible to know with 100% certainty which pathways are affected by an injury and to what extent. The main advantage of models, such as the MIIND network used here, is that the precise extent, mechanics and behaviour of the model are all completely transparent and observable. For testing and development of a BMI device it is imperative that there is certainty in the model used as this allows precise testing of the device's capabilities, rather than its success or failure being reliant on a more or less complete injury condition.

There are also ethical and practical advantages to a simulated model compared to an animal model or human subject. Human subjects are difficult to recruit and present unique difficulties for experimental work often requiring specialized facilities. Animal models also require special care, especially in the case of upper spinal cord injury, requiring bladder expression and extensive follow up care. None of these limitations are to suggest that these models have no use, but in the case of the experimental algorithms developed during this thesis a simulated method is preferable.

The aim of this chapter was to develop and test the combination of the algorithms described in Chapters 3 and 4 as a simulated BMI device. This required a simulated model of damage to the nervous system that reflected changes to synergy recruitment observed previously in human subjects. The same MIIND model previously described in Chapter 2.6 was altered to replicate changes observed in synergy recruitment as reported within the literature. Together these results demonstrate closed loop re-construction of healthy synergies in an *in silico* model. This provides the basis for a BMI device that could provide benefit in a variety of implementations.

5.2.1 Synergy recruitment changes in set ways following injury

The changes in synergy recruitment post-injury due to trauma or stroke can be broadly grouped into three categories; fractionation, merging and emergence of novel synergy patterns. As synergy recruitment is the target motor output for our device it is important that the injury model recreates changes observed in human subjects. These alterations have been largely examined in stroke patients as it is hypothesized that the networks responsible for recruiting synergies will be largely intact. These studies have found that existing synergy profiles are altered in two ways that may reflect the extent of the injury,

or the time since the injury occurred (Cheung et al., 2012; Pan et al., 2018). Merging of synergies occurs in the most severe injuries wherein the previous set of healthy synergies are apparently combined. The degree of merging that occurs correlates with injury severity, with the most severely injured patients demonstrating the greatest degree of merging. The other alteration is known as fractionation. Fractionation represents an increase in synergy dimensions compared to healthy conditions. This is typically observed in patients in the latter stages of recovery and may be reflective of adaptive processes compensating for the injury. We may also consider the possibility of the emergence of entirely new synergies. Novel synergy recruitment has not been previously observed in humans following injury. If this is observed in the simulation it may reflect an artefact of the stimulation, or it may be because recordings are not usually made in patients immediately post-injury. As our network reflects an extreme acute case (with no recovery) it may be that more extreme changes are present in completely or recently disconnected networks.

5.2.2 True closed loop control requires integrating analysis of motor output with the provided stimulation

Many BMI devices seek to implement closed loop control. This is usually defined as a system or device wherein the response produced by the device goes on to affect the way that input is then provided to produce the next output. Most devices in the field rely on sensory feedback to close the loop via visual feedback. For true closed loop control error correction should come directly from the output produced rather than assume the error can be accounted for by the animal. In the example of Nishimura et al spinal stimulation was provided to a set of flexor and extensor neurons in the monkey hindlimb to facilitate walking (Nishimura et al., 2013). Error control is handled by the monkey visually observing the produced movement. The simplicity of the neural encoding meant that stimulation parameters did not have to be altered throughout the gait cycle and this was sufficient to achieve unaided locomotion. In the healthy animal, feedback is provided at the level of the spinal cord, at the point of “stimulation”, and certain types of afferent feedback e.g. proprioception, fatigue, muscle load, should be available as the movement is determined.

A BMI that incorporated the accounts for errors in the output might be capable of more complex movements or for error correction to occur during a movement. This BMI would much more closely mirror the way in which movements are produced during normal

conditions. The error correction used in the device developed in this chapter moves closer to this form of closed loop control by modelling output in terms of muscle synergies. In this case adjustments were not made during the movement, but by placing synergy restoration as the target output we account for the actual effect of stimulation. In principle, the BMI described here is more capable of adapting to changes or errors that would be present in a biological model.

5.3 Results

The stimulated network for control of the knee used in Chapter 3 was used as an injury model by reducing or removing connections. The injury types that were broadly modelled consisted of removing cortical drive (modelling stroke or incomplete spinal injury at a rostral point) and the removal of afferent feedback (modelling a peripheral injury). The location of these injuries within the network are shown in Figure 2-B. Injury type was further split into targeting of the flexor or extensor interneurons as well as a bilateral injury affecting both pools. The results of these injuries were examined using the synergy extraction algorithm also described in Chapter 3. The ANN described in Chapter 4 was then trained to stimulate and predict the resulting motor neuron output in a similar fashion to how it was used to predict EMG output. Finally, the predictions from this network were used to calculate the required stimulation to recreate healthy synergies. This stage was only performed in the extensor injury condition as in principal the ANN's performance should not differ between these conditions.

5.3.1 The injury model recreates changes to synergy recruitment in the same way as observed in humans

In the injury model the synergies extracted from the 8 different unilateral injury types were compared to the healthy model. These are shown in Figure 5-A for extensor injuries and Figure 5-B for flexor injuries. The effect of afferent feedback was also examined using the levels corresponding to 0 and 90 degrees as established in Chapter 3.

The rank factor for each condition was selected to account for >95% of the variance in the original data set. This resulted in different numbers of synergies across conditions. In the partial injury conditions one synergy was sufficient to account for the majority of variance, whereas in the total injury conditions two synergies were required as seen in 5-A and 5-B. The results for bilateral injuries are shown in Figure 5-C. As is expected a complete cortical injury abolishes synergy recruitment as motor neuron firing does not

rise above background levels, but nominally this results in just one synergy being “recruited”. In the bilateral peripheral injury, synergy recruitment is reduced to a single rank reflecting balanced recruitment of all muscles.

The composition of the synergies recruited also differs from healthy synergies. Interestingly the effect of afferent feedback is reduced across all conditions, unsurprisingly in the case of total peripheral injuries where it was removed, but also in cortical conditions where it was untouched. Across all injury conditions, partial injury results in a merging of synergies resulting in a single balanced recruitment of all muscles. The total injury conditions exhibit more drastic changes, and greater differences between flexor and extensor injuries. As seen in Figure 5-A, extensor injury in both cortical and peripheral conditions result in fractionated synergies. Synergy 1 appears to be a biased recruitment of the quadriceps muscles, whereas synergy 2 appears intact at first but has lost RF bias and recruitment of ST and BF are at levels closer to synergy 1. Taken together this suggests that this synergy pattern is actually a fractionation of healthy synergy 1 along the lines of flexor/extensor lines. Figure 5-B shows that the flexor injury conditions demonstrate more drastic departure from healthy synergies with the appearance of entirely novel recruitment patterns. Synergy 1 is common to both cortical and peripheral injuries and seems to be biased towards RF, ST and BF, with minor recruitment of VL and VM. In the cortical injury synergy 2 recruitment is entirely biased towards the quadriceps muscle grouping. In the peripheral injury there is also biasing towards the quadriceps muscles but curiously recruitment of RF is entirely absent.

For the most part the activation coefficients of the altered synergies are largely preserved. Merged synergies are recruited mirroring the contraction period with no major departure. In those conditions with two synergies recruited these recruitment curves are more directly opposed to one another, with a steeper negative relationship in their recruitment profiles.

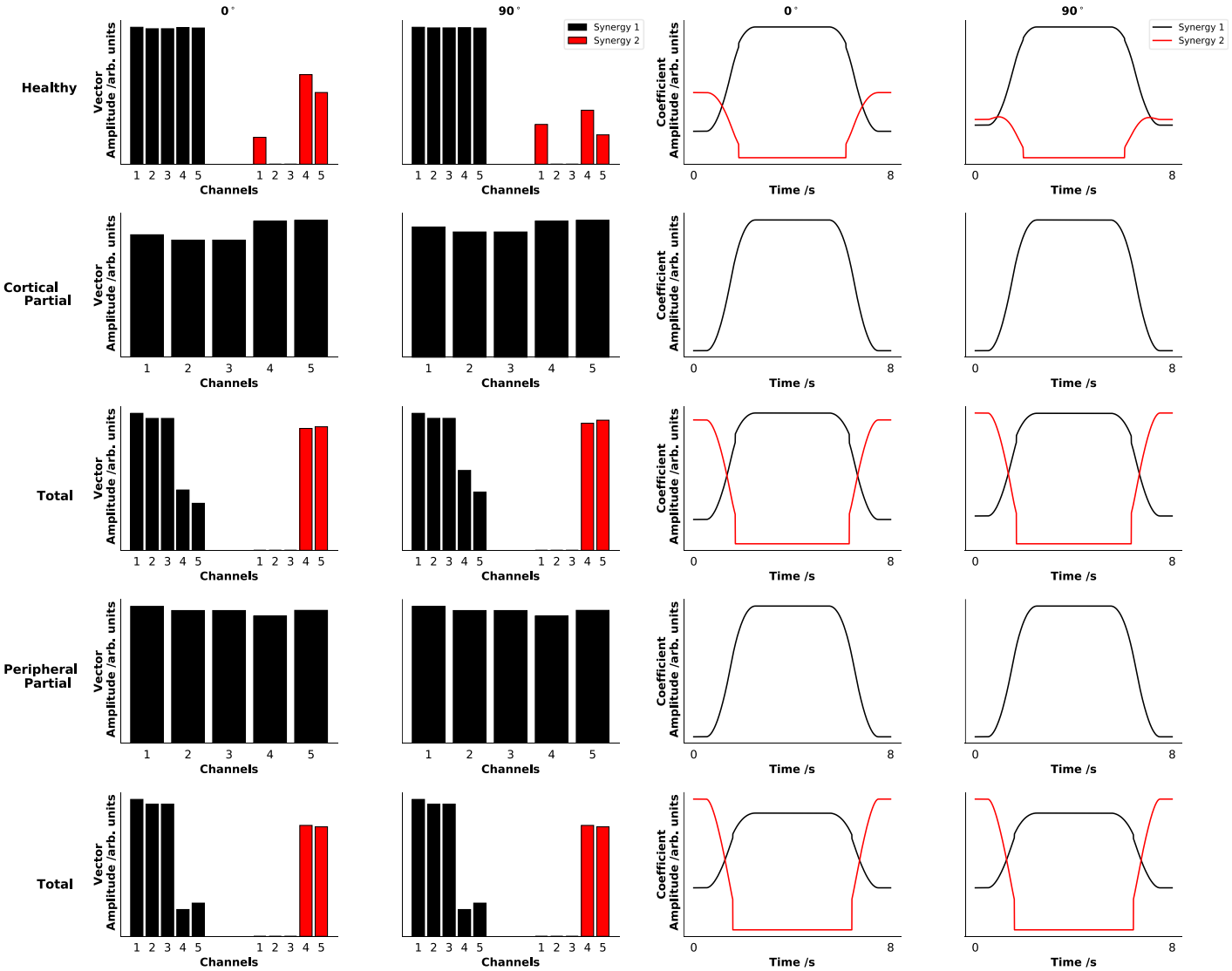

Figure 5-A: **Muscle synergies extracted from MIIND network modelling different injuries affecting extensor interneurons.** Bar charts represent synergy vectors, line charts are synergy coefficients for synergy 1 and 2 (black and red). Synergies were extracted using NMF such that variance accounted for exceeded 90% minimizing number of synergies. Two types of injury were compared to the healthy synergies previously modelled (Chapter 3) cortical injury and peripheral injury, and two subtypes, total and partial injuries, with partial defined as loss of half of connecting neurons. Cortical injury corresponds to removal of descending input to interneuron pools and peripheral injury as loss of interneuron connections to afferent and motor neuron pools.

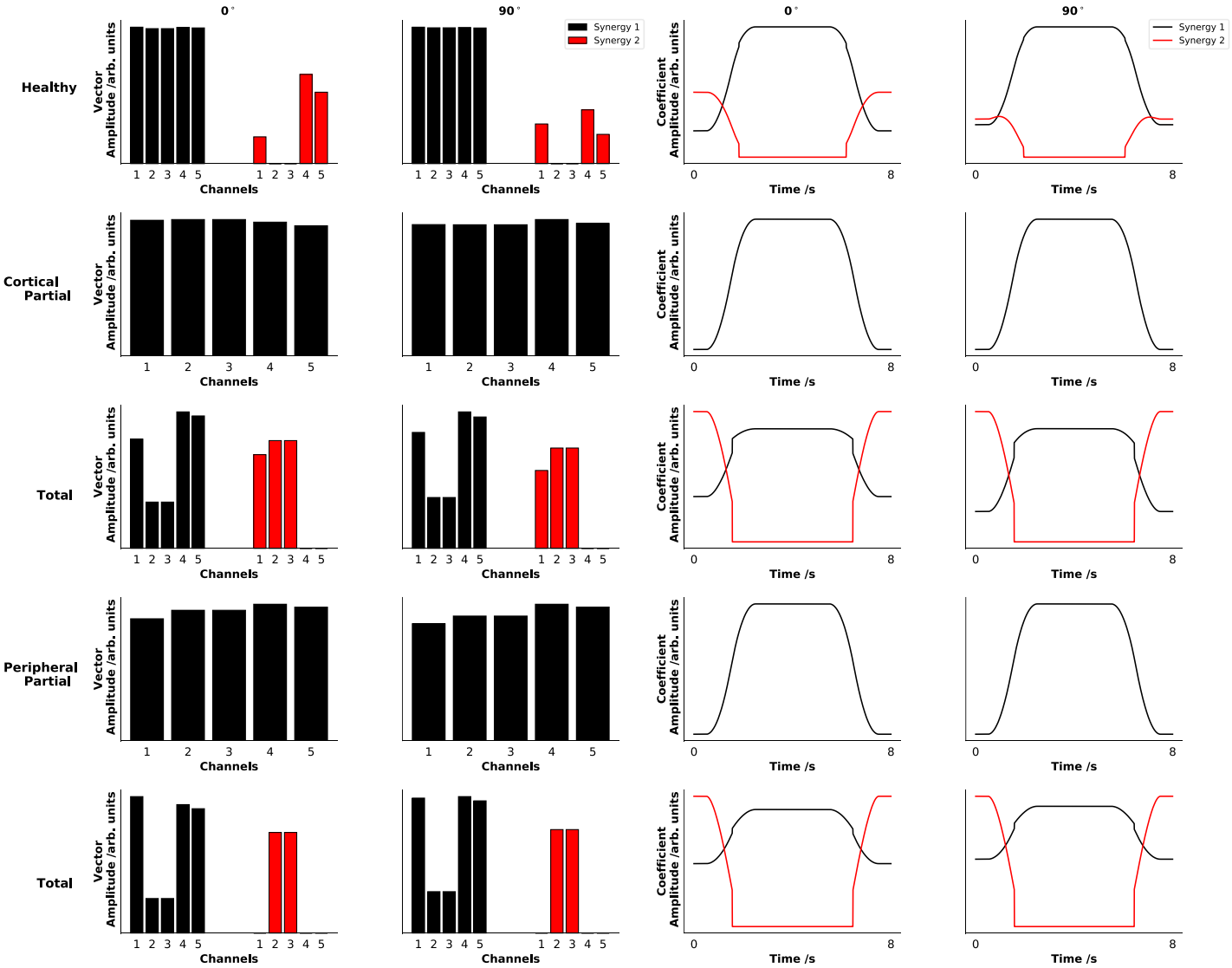

Figure 5-B: **Muscle synergies extracted from MIIND network modelling different injuries affecting flexor interneurons.** Bar charts represent synergy vectors, line charts are synergy coefficients for synergy 1 and 2 (black and red). Synergies were extracted using NMF such that variance accounted for exceeded 90% minimizing number of synergies. Two types of injury were compared to the healthy synergies previously modelled (Chapter 3) cortical injury and peripheral injury, and two subtypes, total and partial injuries, with partial defined as loss of half of connecting neurons. Cortical injury corresponds to removal of descending input to interneuron pools and peripheral injury as loss of interneuron connections to afferent and motor neuron pools.

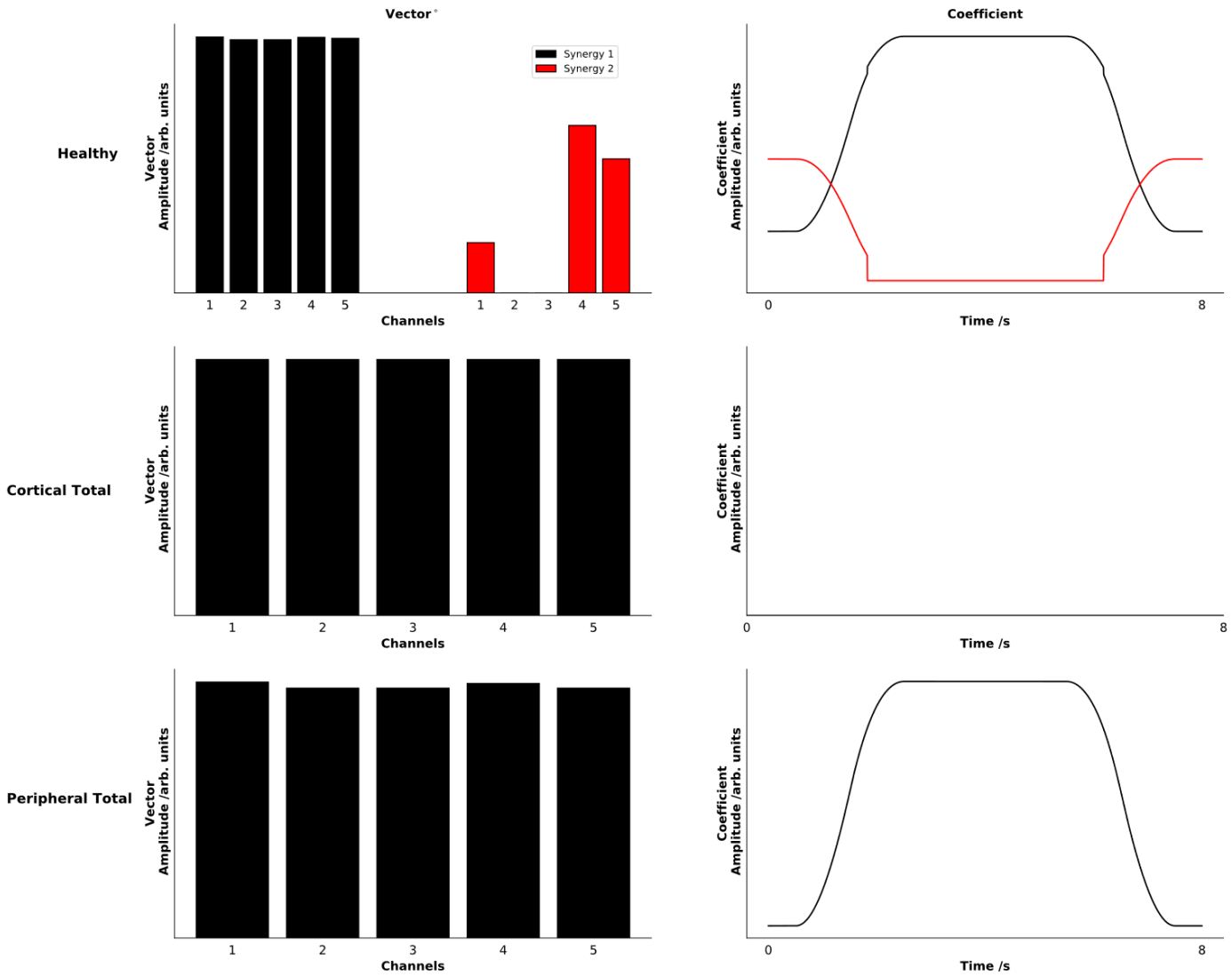

Figure 5-C: **Muscle synergies extracted from MIIND network with modelling a bilateral injury.** Bar charts represent synergy vectors, line charts are synergy coefficients for synergy 1 and 2 (black and red). Synergies were extracted using NMF such that variance accounted for exceeded 90% minimizing number of synergies. Two types of injury were compared to the healthy synergies previously modelled (Chapter 3) cortical injury and peripheral injury, both in the total injury subtypes, defined as loss of all connecting neurons. Cortical injury corresponds to removal of descending input to interneuron pools and peripheral injury as loss of interneuron connections to afferent and motor neuron pools.

5.3.2 An ANN trained in the rat peripheral nervous system was able to learn a transfer function for an *in silico* model of a complex interneuron network

Due to the simulated nature of the modelling process an arbitrarily large dataset could be generated for training purposes. For this dataset conditions were replicated 1000 times for each condition as this was determined experimentally to be large enough to remove dataset size as a determining factor in network performance. The network architecture was left largely unchanged from its presentation in Chapter 4. The only changes made were an increase from 20 to 25 EMG parameters, to account for the change from 4 to 5 muscles, and stimulation was represented by a single “charge injection” value which represents the combined effect of pulse width and voltage. Network training results for each injury show that each network reaches a local minimum without overfitting. The network accuracy results when the networks were trained on 75% of the data were all greater than 95% for both the test and validation data set.

5.3.3 NMF reconstruction of healthy synergy recruitment was successful in a subset of injury types

Following training, the network was asked to predict the stimulation required to generate healthy synergies in the cortical and peripheral injury conditions for extensor injuries. The effects of unilateral injury and the resulting reconstruction compared to healthy synergies are shown in Figure 5-D. For cortical injuries healthy synergies were restored by stimulation of the interneuron pools. In peripheral injuries healthy synergies were not restored, instead the previously observed bias was switched to favour the extensor muscle group. The effect of stimulation on bilateral injuries is shown in Figure 5-E. Again, the cortical injury model was successfully restored to normal synergy recruitment and peripheral injury was not. Stimulation resulted in recruitment of a novel secondary synergy.

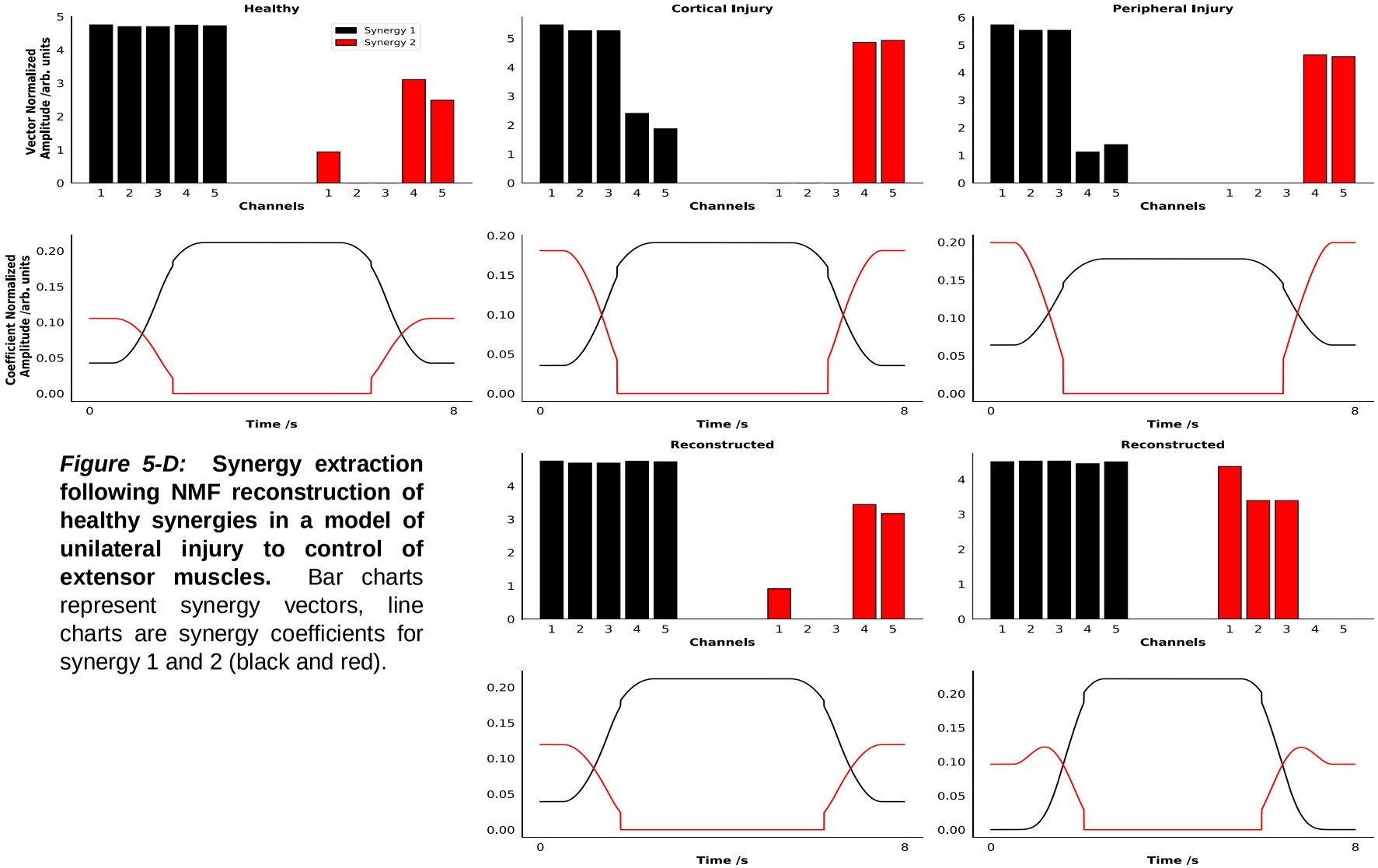

Figure 5-D: **Synergy extraction following NMF reconstruction of healthy synergies in a model of unilateral injury to control of extensor muscles.** Bar charts represent synergy vectors, line charts are synergy coefficients for synergy 1 and 2 (black and red).

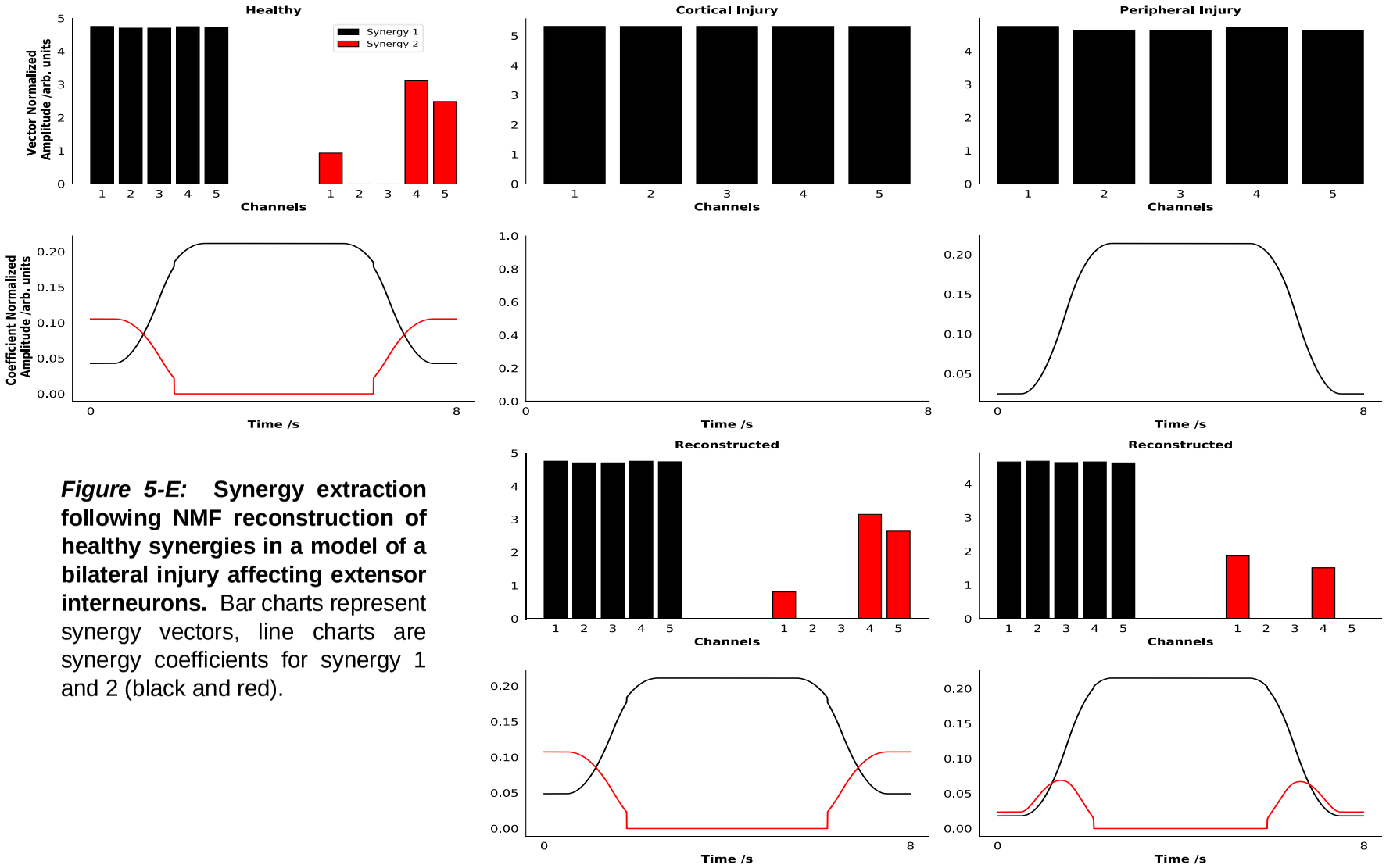

Figure 5-E: **Synergy extraction following NMF reconstruction of healthy synergies in a model of a bilateral injury affecting extensor interneurons.** Bar charts represent synergy vectors, line charts are synergy coefficients for synergy 1 and 2 (black and red).

5.4 Discussion

In this chapter an *in silico* model of different injuries to the nervous that reflects changes in muscle synergy recruitment observed in stroke patients was investigated. The ANN designed for the peripheral nervous system can flexibly be transferred to a model of the spinal cord, despite the associated increase in network complexity. Finally, in combination with online synergy analysis, these systems are capable of restoration of healthy synergy recruitment in certain injury types but not others. This finding further proves the importance of afferent feedback for normal synergy recruitment. The success of the BMI algorithms demonstrated here are built on the previous findings of this thesis. These successes improve on the state of the art by moving closer to “true” closed loop motor control and the flexibility inherent to machine learning approaches allows for fine-tuned control over stimulation.

5.4.1 The MIIND neuronal model can accurately simulate the effects of nervous system injury

The injury types modelled here were selected to broadly reflect injuries affecting interneurons recruiting extensor and flexor muscles. The model was a simple adjustment to the same MIIND network that had previously helped elucidate the role of afferent feedback in recruitment of muscle synergies during an isometric task. This architecture was selected for three reasons. Firstly, this particular group of muscles has been used as a model of synergistic recruitment as far back as Sherrington (Sherrington, 1910; Duysens et al., 2013). Secondly the lower limb has been frequently neglected in the field of BMI, despite its importance for a variety of tasks in normal life. Finally, a network demonstrated in the upper leg may well work well in the lower leg as well and therefore translate well to improvements aimed at treatment of foot drop, a relatively accessible disease case for trial of experimental devices.

As mentioned MIIND has been used previously, including in this thesis, for modelling of neuronal networks. However, the results shown here demonstrates an increased utility in its ability to model injured networks equally well. Removing or reducing connections between pools is a simplification of real-world injuries but despite this, complex and realistic alterations result. This work naturally suggests further additions to the model could be made, including introducing recovery and more dynamic Hebbian style connection pruning.

5.4.2 The ANN learns a general transfer function that is transferable from animal data to human data

The success of the network is more impressive considering it was originally designed to work in rodents, controlling a different set of muscles. This speaks further to the generalizability of the ANN architecture described. It indicates that the system is capable of adaptively learning representations between stimulation and motor output in a more general sense. This presents opportunities for further investigation, both within the *in silico* model and in other biological models.

5.4.3 Closed loop BMI control can restore healthy muscle synergies in some injury states

Stimulation at the level of the spinal cord has the major advantage of removing "unnatural" connections from a BMI device. In theory this allows for recruitment of intact networks the body uses for motor coordination. Compared with stimulation in the periphery, spinal stimulation often results in a diffuse response and it is difficult to recruit a single desired muscle. This is partly the desired response, as this diffuse response is due to recruitment of whole networks of neurons. However, it also comes with the disadvantage of decreasing specificity. Recruiting a specific neuronal network, or sub network, to produce a desired movement requires more specific stimulation to avoid widespread recruitment of unnecessary muscles. The specificity problem increases the further the source of the neural activity used is separated from the point of stimulation. A device stimulating the cortex directly would require an extremely complex and precise stimulation device coupled with a hitherto unprecedented understanding of the cortical networks (at this stage, it would in principle be possible to model the working of the cortex entirely within a computer, suggesting a level of understanding that remains firmly science fiction). The experiments previously described in Chapter 4 describe stimulation of the peripheral nervous system. This may be seen as the simplest condition to solve but, as seen in the variable responses of the hindlimb muscles, stimulation swiftly spreads to a variety of endpoints. In the cortical injury the system successfully restores healthy synergy recruitment. This is despite the additional layer of separation posed by the interneuron layer and the balancing required for the excitatory and inhibitory connections. This suggests that the specificity problem may be tractable for machine learning methods in a biological scenario.

The failure to restore healthy synergies in the peripheral injury condition is more enlightening than it may at first appear. In combination with the modelling work performed in Chapter 3 it is clear that afferent feedback is a vital component for healthy synergy recruitment. The stimulation sites in this chapter were purely excitatory and were limited to either the interneuron pools solely or in combination with direct stimulation of the motor neurons. It is interesting that even with direct, perfect access to motor neuron firing, the network was unable to replicate the fine balancing between agonist/antagonist. It is not the case that the network has failed at an impossible task, due to the nature of the MIIND simulation there is a theoretical value of stimulation that would replicate the synergies observed in the healthy state. That the network is unable to find this value in one condition, yet succeeds perfectly in another, is indicative of a change in complexity between these conditions. If the stimulation paradigm had included access to afferent nodes then perhaps the model would have successfully restored synergies in the peripheral injury as well. These nodes were not included within the accessible sites as it is difficult in vivo to easily differentiate afferent nerves with sufficient specificity but this represents a promising avenue for further investigation.

5.4.4 Model limitations

The results of this model simulation must be carefully considered with the assumptions and limitations present in the model as well as the way in which stimulation was targeted within it. Due to the way that stimulation is provided in the model, the simulation is capable of perfectly mimicking natural signals, which is not true in vivo. Electrical stimulation has limitations that prevent normal recruitment curves and completely isolated charge injection. The selectivity of the stimulation sites is also not reflective of current capabilities. As previously mentioned, the specificity problem results in widespread recruitment of motor neurons. The precise targeting of individual motor neurons provided here is possible in principle through high density array electrodes but is difficult in practice. Similarly, even and balanced recruitment of a specific interneuron pool would be near impossible in real world conditions, due to charge spreading to other networks in physical proximity.

5.5 Conclusion

The work in this chapter brings together the algorithms described in Chapters 3 and 4 to demonstrate restoration of healthy synergy recruitment using an *in silico* BMI in different models of nervous system injury. An injury model of interneuron-controlled synergy

recruitment was able to recreate the same alterations to synergy recruitment observed in human injury conditions. The ANN used previously in Chapter 4 in the peripheral nervous system was able to transfer to a new stimulation environment supporting the idea that the network is capable of representing a generalized transfer function. Finally, within this environment higher order motor control was used as a target for control of stimulation paradigms, moving towards true closed loop BMI control.

- The MIIND network previously used to model upper leg muscles was able to various types of injury and the resulting alterations in muscle synergy recruitment
- The ANN previously trained in the rat peripheral nerve successfully learnt the stimulus/response relationship in an *in silico* model of spinal interneurons
- An *in silico* BMI device made by combining these algorithms was able to restore healthy synergy recruitment in some injury conditions
- The BMI failed to restore synergy recruitment when afferent feedback was abolished. This supports our previous findings that afferent feedback plays an important role in synergy recruitment
- These algorithms together represent a BMI device capable of general restoration of muscle synergy recruitment. This could be implemented in a variety of settings for treatment of muscle weakness or paralysis.

Chapter 6: Discussion

6.1 Summary of key findings

The field of BMIs is experiencing a surge in new devices, approaches and algorithms that attempt to advance the cutting edge of what is possible. With this new drive it is important to question common place assumptions in device design; challenging these assumptions can sometimes provide significant improvements compared to the resources invested. All the algorithms presented within this thesis attempt to address the problems faced at different stages of a BMI device in novel ways. This thesis has explored advances in the understanding of muscle synergies, stimulation control using machine learning, population modelling of spinal circuits and how these can all be integrated together in one device. Algorithm development within this thesis has strived for a firm biological basis. This was done in an attempt to avoid falling into innovation for innovations sake and to instead focus on integrating biological understanding into device development. The algorithms developed represent a device capable of general signal transfer between areas of the nervous system and moves towards closed loop control of the paralyzed limb.

Initially the performance of an online implementation of various onset/offset detection and synergy extraction algorithms was investigated, in terms of their accuracy and speed in different settings and in combination with one another. Findings regarding the utility of SampEn in data contaminated with aberrant spiking was challenged. It was also shown for the first time the performance loss that occurs when these algorithms are combined. The best performing algorithm, NMF, was then used to investigate the role of proprioception in synergy recruitment during an isometric task. Contrary to some findings in the field, changes were observed in the profile of synergy 2 in accordance with changes in limb position reflecting the change in balancing of agonist/antagonist activation due changes in muscle stretch. A mechanistic explanation for this was proposed by modelling parts of the CPG spinal interneuron network and changing levels of afferent feedback. This model successfully reproduced the synergies and their changes in response to afferent feedback observed in human subjects. For the first time in humans' elements of the CPG were shown to be used for a non-locomotor task. A clear role for afferent feedback in recruitment of muscle synergies was also demonstrated. This set of algorithms represent the proposed "output" measure of the device, with muscle synergies as the target. Next a method for control of stimulation of

the nerve was developed using automated machine learning methods, which represents the “input” control. An ANN was trained to predict with a high degree of accuracy the EMG parameters recorded from muscles of the rat hind limb following stimulation of the sciatic nerve. Furthermore, this network learnt a generalized transfer function capable of translating the learnt relationship from a subset of animals to unknown conditions. This network was also able to be repurposed and used in an entirely different *in silico* environment further supporting the idea that the network can represent a generalized transfer function. Finally, in this new *in silico* environment a novel method of modelling injury to the nervous system was demonstrated in a way that replicates the major changes in synergy recruitment observed in humans. Within this environment, output-input algorithms were combined from previous chapters to demonstrate successful restoration of healthy muscle synergy recruitment in cases of cortical injury.

6.2 Discussion of key findings

Through discussion of the findings of each chapter, an attempt will be made to provide further understanding of the significance of these results when considered as a whole, as well as to reflect on their limitations. In particular consideration for how these experiments could be expanded upon as part of future work will be addressed.

6.2.1 Methodological assumptions affecting muscle synergy extraction

Before implementation of synergy extraction algorithms for the purposes of further analysis or integration into a BMI, assumptions were first examined regarding the performance of these algorithms in different conditions. Findings were compared in onset detection using the gold standard of visual inspection, but for dimensionality reduction we first had to implement a method of synthetic synergy generation. The findings in terms of synergy extraction are in line with previous studies, however the difference between ICA and NMF was limited in the conditions examined here which may explain the disagreement between certain studies that have argued in favour of either approach (Tresch and Cheung, 2006). In contrast the advantages of SampEn in avoiding aberrant spiking activity can be replicated through careful selection of hyperparameters in a sliding window using a simple average amplitude (Zhang and Zhou, 2012). This comes with a significant decrease in calculation speed and was a superior measure for our purposes. These methodological considerations reflect the need to consider carefully the data these algorithms are applied to for maximal performance.

6.2.2 Proprioceptive feedback into the recruiting interneuron network is vital for healthy synergy output

Taking the results from the previous work into consideration a method for online synergy extraction was developed and applied to an isometric task to explore the role of proprioceptive feedback in synergy recruitment. By limiting the task to an isometric task repeated at various internal angles of the knee it was hypothesised that afferent feedback would be limited to proprioceptive sources. Therefore, any changes to synergy profiles would reflect a change due to afferent feedback. Although the first synergy identified was invariant to joint angle, the second synergy reflected a change in recruitment that matched biomechanical expectations due to changes in muscle stretch. Whilst it seems certain that sensory feedback must play a role in motor control at this level, previous studies have shown surprisingly fixed synergy recruitment in conditions one might expect afferent feedback to play a large role (Torres-Oviedo et al., 2006; Roh et al., 2012). This is likely is due to the adaptability of the synergy recruitment process, where in more dynamic conditions other changes may be made to recruit a preferred synergy pattern, in the fixed state of an isometric task the synergy itself must be altered to produce the movement.

This finding is interesting by itself, however it was further supported with a model of how afferent feedback could be incorporated into synergy recruitment. Therefore, using the lower levels of the CPG model developed by Rybak a model was created within the MIIND framework that reflected the proposed interneuron network that recruits the muscles under investigation (McCrea and Rybak, 2008). This model was created specifically to have balanced cortical recruitment across all conditions, so that any change observed would similarly be restricted in cause to the level of afferent feedback. The replication of the experimental findings by the model supports the role of proprioceptive feedback in synergy recruitment. This model suggests a great deal about both the muscle synergy hypothesis as well as the current understanding of the CPG. It suggests that muscle synergies are recruited flexibly from networks of spinal interneurons that may have a variety of other purposes, and similarly it suggests that the CPG is a flexible control system for tasks that require balancing of flexion/extension within the lower limbs beyond locomotion.

6.2.3 ANNs are capable of learning generalized transfer functions in the nervous system

Determining the relationship between stimulation at one point and the motor output at another is a key step in a BMI for restoring motor control to the paralyzed limb. The algorithm shown here attempts to leverage the advantages of machine learning in an environment well suited to (and in spirit modelled on) them. Acquiring the large datasets required for successful network training was a challenge in and of itself and required specialized stimulator construction and more customised Python code. Despite this the dataset described here is still small in scale compared to normal datasets for machine learning. The network architecture described was capable of a very high degree of accuracy in prediction of the stimulation parameters that generated a given set of EMG parameters. This in and of itself may be relatively unimportant if the network has overfitted to the training dataset. The performance on unknown data is the true test of the network's utility, as this describes its ability to generalize to new conditions. Restricting the already small dataset for unknown conditions will certainly affect the performance of the network. In spite of this the network adapted very well when asked to predict an entirely unseen animal's EMG's, predicting voltage with similar levels of accuracy and still providing an attempt at width prediction. This in itself may reflect the network has learnt the relationship at a more general level as it has prioritized the more "important" voltage parameter, as this describes a greater amount of variance within the signals. It is entirely possible that with more data performance on width may increase further.

This finding is only further supported by demonstration within a new setting. Implementing this network within the *in silico* MIIND simulation involved insignificant changes to the overall network architecture (input and output layers). Although previous work demonstrated the MIIND model represents experimental muscle synergy response it remained to be seen if it would also respond in a predictable way to stimulation. The advantages of a simulated environment are clear here as it is possible to generate a dataset of sufficient size that dataset size can be eliminated as a variable affecting network performance. The networks performance is even better than in the animal model, capable of predicting with almost perfect accuracy the resulting EMG parameters. However, discussed below in Section 6.2.5, this increase in performance does not result in an increased utility in all conditions.

6.2.4 The MIIND network is capable of modelling damage to the nervous system

Simulated models of injury conditions have both ethical and practical advantages as we have already indicated with training of our ANN. The MIIND network allows flexible and accurate modelling of neuronal networks in a variety of configurations, with an ease of use that encourages rapid prototyping or adjustment to new conditions. The demonstration of healthy synergy recruitment and the alterations that can occur with both upstream and downstream damage suggests a platform for further motor control research.

6.2.5 Restoration of healthy muscle synergies by an *in silico* BMI

The previous chapters algorithms were designed to have significance on their own, but also as part of a larger device. In the final chapter these algorithms combined to produce an *in-silico* representation of a BMI capable of restoration of healthy muscle synergies. Motor output was measured using the online synergy extraction algorithm from Chapter 3, and these synergies were set as the target for this device. This is another advantage to simulated environments as it allows our device to have access to pre-injury conditions, which is an obvious caveat to the performance shown here. The ANN was used for stimulus control and asked to predict the required stimulation to generate healthy synergies in the injured network. For cortical injuries, reflecting a loss of descending drive, this worked excellently for both the unilateral extensor injury as well as for a bilateral injury reflecting a more widespread loss of function. However, for no condition was the network able to restore synergy recruitment with the loss of afferent feedback in peripheral injury conditions. This was true even when the network was given access to a greater number of stimulation sites. As mentioned, the network learnt the representation between stimulation and output exceedingly well in the simulated conditions, so how was the network unable to produce healthy synergies? It is proposed that this is due to the special and complex role that afferent feedback plays within this network to balance agonist and antagonist recruitment. Compared to cortical drive, afferent feedback influences a more specific subset of interneurons. Examining the mistakes made by the network in the peripheral condition reveals that it switches bias in this condition from the extensor muscles to the flexors, unable to provide the fine-tuned balancing that normal afferent feedback provides. This demonstrates that whilst our algorithms move closer to closed loop control it is vital that future devices take greater account of afferent signals to more naturally restore motor control.

6.3 Utility to the field

All scripts described herein are available at https://github.com/gareth-york/neural-bridge and MIIND is available from http://miind.sourceforge.net/. These scripts were written with the intention that they be easily implemented within different environments.

6.3.1 Synergy detection algorithms, comparison and online implementation

The system of synergy detection algorithms and the comparison of performance are available in two separate implementations. The system of tests shown in this thesis are designed in a modular fashion such that if new measures or methods of onset/detection or synergy extraction were developed it would be simple to compare them to previous findings. It is also simple to re-reset these algorithms for a different set of data conditions, this is particularly useful in the case of synergy extraction algorithms where ICA and NMF have variable performance between authors and implementations. The second section provides the online synergy extraction using NMF and an average onset detection with visual feedback of updated synergies in near real time. Participants are usually asked to maximally recruit a given muscle or set of muscles within motor control studies, with or without visual feedback on the EMG signal. It may be that providing synergy feedback may allow more specific synergy recruitment and reduce variability between subjects.

6.3.2 Algorithms for automated stimulus control

The algorithms for producing the dataset for ANN training have more specific utility but are an expansion on the algorithms provided by SanWorks for the PulsePal device. In comparison to other isolated stimulators these algorithms allow for fine-tuned control of stimulus parameters from up to four channels while outputting a standard TTL pulse for triggered recording. This has the immediate advantage of freeing attention for the operator but more so it allows for much greater complexity of stimulus paradigm as shown in the experiments here. When combined with the ANN described here it provides a powerful platform for stimulus/response measurement for a variety of devices or recording scenarios.

6.3.3 Simulation of neural networks

The current capabilities of MIIND are significant, however the model is still undergoing active development and new features are planned in the near future. Flexible modelling of whole populations of neurons can be a useful tool in any number of settings, both for

informing and being informed by experimental data. The simple addition of injury modelling described here is only the beginning of what can be achieved with careful thought. By running multiple simulations with incrementally increasing or decreasing connection strength it would be feasible to model Hebbian plasticity amongst neurons or recovery post injury. Analysing deficits in patient's synergy recruitment profiles could identify potential injury sites and suggest more personalized treatment plans. Lastly the network described here is a single modular block but there is nothing to prevent the network from being arranged in concert with further networks. This could allow for models of greater scope that can include more dynamic cortical control networks.

6.4 Clinical significance

6.4.1 Muscle synergies analysis for assessing physiotherapy in the elderly

Muscle weakness in the elderly is an incredibly common cause of falls and subsequent hospitalizations. Preventative physiotherapy is often recommended for frail or elderly patients (De Labra et al., 2015; Soukkio et al., 2018). Current methods for assessing muscle weakness do not take into account the changes in synergy recruitment observed due to change in limb position. This knowledge by itself may introduce new avenues for improvement, but by using synergy analysis during standard testing may allow for better understanding of a patient's specific deficit. When this is understood it may be possible to introduce movements or exercises that better target that deficit. This is particularly relevant for patients with limited mobility or energy as they may only be capable of a limited number of exercises and therefore, treatment efficiency must be maximized.

6.4.2 BMI for treatment of foot drop

The direct applicability of the combined algorithms shown here to a clinical setting can only be considered in terms of currently available devices, as the hardware implementation shown here is obviously not applicable to human subjects. As previously mentioned, FES has been used previously for the treatment of foot drop via stimulation of the peroneal nerve to recruit the unaffected motor neurons (Barbeau et al., 1999; Embrey et al., 2010; Kesar et al., 2011; Melo et al., 2015; Ferrante et al., 2016). Electrical stimulus is usually predefined and controlled either using a handheld remote or increasingly are automatically triggered based off sensors in the shoe or by measuring electromyography (EMG) signals from the muscles of the foot. FES is particularly promising for treatment as it offers a curative solution to the aetiology of the condition,

potentially to a stage where a prosthetic device is no longer required. However, despite this potential, current devices are extremely limited in the methods by which stimulation is delivered. Stimulus parameters are predefined at device fitting and rarely updated in check-up sessions that may be months apart. This once again demonstrates the same problems described previously; it relies on the expertise of the operator to select the correct parameters; it does not update in line with changes in performance and the choice of stimulation parameters is usually limited to a single variable. This may be why current studies are mixed on the effectiveness of AFO versus FES devices. FES devices show great promise for a subset of patients, but often the performance is much more variable. If this is a failure of the device or due to differences in patient potential is unknown, but one way to investigate this would be an algorithm similar to the one described here.

It has been previously demonstrated that FES incorporating muscle synergies into the stimulation control could restore healthy synergy patterns in patients with foot drop (Ferrante et al., 2016). The ANN designed in Chapter 4, in combination with the previously described online synergy analysis program could form a closed loop stimulation device. This device would combine real time analysis of motor output with an adaptable and more specific control of stimulation parameters to improve further on this result. Furthermore, the collection of stimulation datasets for training would give clinicians a much greater understanding of the precise patient deficit, in terms of muscle weakness in concrete terms. This in turn may give greater understanding of why some patients respond better to FES than others. Furthermore, the device training allows for comparatively easy updating of stimulus control network compared to requiring a follow up appointment. It would be feasible for updating to occur regularly on a home computer allowing for the treatment provided to keep pace with a patient's recovery or decline during use.

6.5 Future directions

6.5.1 ICA-PCA and autoencoders for synergy extraction

The correct method for synergy extraction is not a settled issue. Indeed, although the methods examined here represent the most commonly used methods suitable for online analysis, there are other methods that bear further investigation. One such method is PCA-ICA, wherein ICA is used to explore the new feature space defined by PCA. This method has previously been shown to be more accurate than either ICA or NMF (Tresch

and Cheung, 2006). This method was not explored here due to its exceedingly large computational time precluding online use, but this was likely due to algorithm implementation rather than inherent complexity. Another interesting method of synergy extraction are autoencoders. Autoencoders are a special type of ANN wherein the target output of the network is its input. Instead of using large hidden layers, an autoencoder can reduce the number of nodes in the hidden layer compared to its inputs. The activity of this hidden layer can be used to represent the synergy structure. This method has also been shown to be more effective than ICA and NMF (Spüler et al., 2016). Autoencoders also have the advantage of being easy to integrate into a larger deep neural network, potentially directly into the ANN used for stimulation control. Comparing these methods with the more commonly used ICA and NMF may have provided further insight into why these methods are more effective, or if their performance is also dataset dependent.

6.5.2 Expanded stimulus/response experiments at greater degrees of separation

Following the success of the ANN architecture at learning at generalized transfer function in the periphery and in a simulation of spinal networks, the next obvious step is to attempt to increase the separation a step further in the biological model. As argued previously, stimulation at the level of the spinal cord reflects the optimal point for recruitment of surviving neural networks in spinal cord injury. Attempts were made during the recording of the peripheral dataset to collect spinal recordings; however, this was only possible in a fraction of animals, and never with complete datasets. Increased focus at this level could be achieved with off the shelf components and with existing surgical setups used for stimulation during recovery. This study would fully test the limits of the architecture to generalize at the level required for a spinal BMI to overcome the specificity problem.

On a less ambitious level, the control of stimulation was defined here by just two parameters, although these were examined with more resolution than is usually performed. Due to the ease with which the PulsePal can deliver precise patterns of stimulation a variety of different parameters could also be examined for their effects on motor output. A problem this may be of particular relevance to is the reversal of motor curve recruitment. When the body recruits motor neurons it does it in order of smallest to largest (as required for the task). However, when FES is used this order is reversed with largest fibres recruited first. This has been suggested to be the cause of excessive fatigue and the painful sensation that can accompany FES. Potentially this is due to how

stimulation is delivered, perhaps a different pulse shape may result in normal recruitment curves in certain combinations.

6.5.3 Isolating the role of afferent feedback for synergy recruitment in dynamic tasks

The data presented in Chapter 3 demonstrates that afferent feedback has a role in synergy recruitment during an isometric task. This is in direct contrast to some findings in the hand and is at odds with findings of preserved synergies in dynamic conditions. Clearly afferent feedback is required for healthy synergy generation as shown by their abolition in conditions of complete removal of afferent signals. However as shown in certain cases of rhizotomy of the dorsal root, synergies can be largely preserved in cases where afferent feedback is significantly altered. Further investigation is required using synergy analysis in a spectrum of tasks, with further modelling work. Tasks to investigate further include non-isometric knee extension and flexion and locomotion, potentially including the effects of perturbations under different states of afferent feedback. All of these scenarios may bridge the gap between dynamic and static tasks and identify where exactly afferent feedback enters the synergy recruitment pathway, and why it is sometimes ignored.

6.5.4 Locomotion synergies and the CPG within the MIIND framework

In line with this thinking is the use of MIIND to further investigate the ways that interneuron networks can be flexibly recruited to different tasks. This work demonstrated that the lower levels of the CPG are implicated in synergy recruitment for isometric extension of the knee. Synergy recruitment during locomotion has been extensively studied previously and therefore the expected profiles are already known. Extending the current MIIND network to include all layers of the CPG and to induce cyclical excitation/inhibition would be a relatively simple addition. This would provide the same justification for those findings as used here and would also extend the model to another environment. More importantly it could also be attempted to try and elucidate further what feedback or descending signals are required to cause one or the other to occur. Is it entirely a cortically controlled process, or is the switch mostly accomplished via afferent feedback? Developing the framework to answer these questions and others would provide powerful evidence for the Rybak model of the CPG and potentially give a much greater understanding of the fluidity of synergy recruitment networks.

6.6 Concluding remarks

This project initially aimed to develop the algorithms required to drive a BMI to facilitate communication across a region of nerve damage to provide novel new avenues of treatment for spinal cord injury. Algorithms were designed from a top down perspective considering the output and input sections of the end device. For output analysis it was determined that muscle synergies are an ideal end target as the same solution used by the CNS to simplify the problem of motor control. To achieve this an online synergy analysis algorithm was developed based on tests determining the performance of the most commonly used methods for synergy extraction and EMG activity detection. The best of these algorithms was used to demonstrate that afferent feedback played a role in synergy recruitment during an isometric knee extension to balance agonist/antagonist activity between the hamstrings and quadriceps. The integration of sensory feedback was further examined using a model of the CPG interneuron network in the MIIND simulation framework. This model explained the experimental findings using only changes in afferent feedback, further solidifying a role for proprioception in synergy recruitment. The next stage of device development focused on determining input to the system provided by the device in the form of electrical stimulation. An advanced isolated stimulator was used to collect large datasets for training of an ANN for modelling the relationship between peripheral nerve stimulation and resultant EMG parameters. The response for each muscle was calibrated using excitation curves calculated using set test pulses delivered throughout stimulation, and by establishing the optimal muscle stretch through the use of an ergometer in response to the same test pulse. This network successfully predicted the stimulation parameters required to generate a given EMG waveform with a high degree of accuracy in a dataset of known animals. It was also successful in predicting the voltage required when tested on a subset of unknown animals. Prioritization of the voltage parameter is indicative of the learning process of the network as it was determined by the variability accounted for by each parameter that voltage is the more important of the two. Finally, having proven the effectiveness of each algorithm individually, they were combined within an *in silico* models of different nerve injuries. The combined algorithms were able to restore healthy synergy recruitment in cases of cortical injury but not peripheral injury. This argues further for the importance of normal afferent feedback in synergy recruitment. The system described here could be readily adapted to available systems for treatment of certain types of nerve injury. Furthermore, the individual algorithms have further application within the field of

physiotherapy for the elderly. This work described here informs and could provide tools for further investigation of the problems faced by BMI devices today.

Appendices

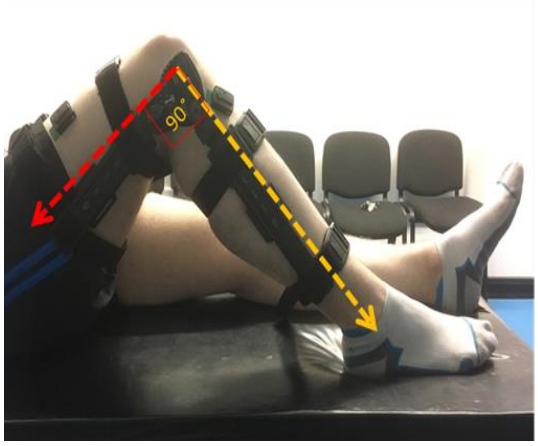

Position 1

Position 2

Appendix 1-A: **Experimental set up.** The effect of afferent feedback on muscle recruitment was examined in two different positions of the contralateral hip to maximize or minimize passive insufficiency due to contralateral hip position. Subjects were asked to lay on a standard medical examination bed. They were then shown how to perform an isometric knee extension with the leg brace attached to their dominant leg. Subjects were shown the resulting EMG output recorded using a Delsys Trigno system. Subjects were asked to perform an isometric knee extension at maximal voluntary effort for five seconds, attempting to maximise RF activity. The dominant knee was fixed at one of four angles using a Donjoy TROM locking knee brace at 0°, 20°, 60° and 90°. In these pictures the knee is at 90°. The angle of the knee was always measured against the hip joint and the bony prominence on the outside of the ankle. Data was collected in both positions for each subject. In position one the participant is supine with both legs flat against the bed. In position two the contralateral leg was kept bent such that the foot is flat against the bed so that both the knee and hip are fully flexed.

Synergy extraction 1	Onset detection 1	Synergy extraction 2	Onset detection 2	Standard Error	Degrees of freedom	P value
PCA	Raw	ICA	Raw	0.0123	1593	<.0001
PCA	Raw	FA	Raw	0.0123	1593	1
PCA	Raw	NMF	Raw	0.0123	1593	<.0001
PCA	Raw	PCA	Average	0.0123	1593	<.0001
PCA	Raw	ICA	Average	0.0173	1593	<.0001
PCA	Raw	FA	Average	0.0173	1593	0.0145
PCA	Raw	NMF	Average	0.0173	1593	<.0001
PCA	Raw	PCA	RMS	0.0123	1593	<.0001
PCA	Raw	ICA	RMS	0.0173	1593	0.0016
PCA	Raw	FA	RMS	0.0173	1593	0.0003
PCA	Raw	NMF	RMS	0.0173	1593	<.0001
PCA	Raw	PCA	SampEn	0.0123	1593	<.0001
PCA	Raw	ICA	SampEn	0.0173	1593	<.0001
PCA	Raw	FA	SampEn	0.0173	1593	<.0001
PCA	Raw	NMF	SampEn	0.0173	1593	0.0001
ICA	Raw	FA	Raw	0.0123	1593	<.0001
ICA	Raw	NMF	Raw	0.0123	1593	<.0001
ICA	Raw	PCA	Average	0.0173	1593	<.0001
ICA	Raw	ICA	Average	0.0123	1593	<.0001
ICA	Raw	FA	Average	0.0173	1593	<.0001
ICA	Raw	NMF	Average	0.0173	1593	0.0066
ICA	Raw	PCA	RMS	0.0173	1593	<.0001
ICA	Raw	ICA	RMS	0.0123	1593	<.0001
ICA	Raw	FA	RMS	0.0173	1593	<.0001
ICA	Raw	NMF	RMS	0.0173	1593	0.1523
ICA	Raw	PCA	SampEn	0.0173	1593	<.0001
ICA	Raw	ICA	SampEn	0.0123	1593	<.0001
ICA	Raw	FA	SampEn	0.0173	1593	<.0001
ICA	Raw	NMF	SampEn	0.0173	1593	<.0001
FA	Raw	NMF	Raw	0.0123	1593	<.0001
FA	Raw	PCA	Average	0.0173	1593	0.0288
FA	Raw	ICA	Average	0.0173	1593	<.0001
FA	Raw	FA	Average	0.0123	1593	<.0001
FA	Raw	NMF	Average	0.0173	1593	<.0001
FA	Raw	PCA	RMS	0.0173	1593	0.0006
FA	Raw	ICA	RMS	0.0173	1593	0.001
FA	Raw	FA	RMS	0.0123	1593	<.0001
FA	Raw	NMF	RMS	0.0173	1593	<.0001
FA	Raw	PCA	SampEn	0.0173	1593	<.0001
FA	Raw	ICA	SampEn	0.0173	1593	<.0001
FA	Raw	FA	SampEn	0.0123	1593	<.0001
FA	Raw	NMF	SampEn	0.0173	1593	0.0002
NMF	Raw	PCA	Average	0.0173	1593	<.0001
NMF	Raw	ICA	Average	0.0173	1593	<.0001
NMF	Raw	FA	Average	0.0173	1593	<.0001
NMF	Raw	NMF	Average	0.0123	1593	<.0001
NMF	Raw	PCA	RMS	0.0173	1593	<.0001
NMF	Raw	ICA	RMS	0.0173	1593	<.0001
NMF	Raw	FA	RMS	0.0173	1593	<.0001
NMF	Raw	NMF	RMS	0.0123	1593	<.0001
NMF	Raw	PCA	SampEn	0.0173	1593	<.0001
NMF	Raw	ICA	SampEn	0.0173	1593	<.0001
NMF	Raw	FA	SampEn	0.0173	1593	<.0001
NMF	Raw	NMF	SampEn	0.0123	1593	<.0001
PCA	Average	ICA	Average	0.0123	1593	<.0001
PCA	Average	FA	Average	0.0123	1593	1
PCA	Average	NMF	Average	0.0123	1593	<.0001
PCA	Average	PCA	RMS	0.0123	1593	0.9939
PCA	Average	ICA	RMS	0.0173	1593	<.0001
PCA	Average	FA	RMS	0.0173	1593	0.9996
PCA	Average	NMF	RMS	0.0173	1593	<.0001
PCA	Average	PCA	SampEn	0.0123	1593	<.0001
PCA	Average	ICA	SampEn	0.0173	1593	<.0001
PCA	Average	FA	SampEn	0.0173	1593	<.0001
PCA	Average	NMF	SampEn	0.0173	1593	0.9981
ICA	Average	FA	Average	0.0123	1593	<.0001
ICA	Average	NMF	Average	0.0123	1593	<.0001
ICA	Average	PCA	RMS	0.0173	1593	<.0001
ICA	Average	ICA	RMS	0.0123	1593	0.9939
ICA	Average	FA	RMS	0.0173	1593	<.0001
ICA	Average	NMF	RMS	0.0173	1593	<.0001
ICA	Average	PCA	SampEn	0.0173	1593	<.0001
ICA	Average	ICA	SampEn	0.0123	1593	<.0001

ICA	Average	FA	SampEn	0.0173	1593	<.0001
ICA	Average	NMF	SampEn	0.0173	1593	<.0001
FA	Average	NMF	Average	0.0123	1593	<.0001
FA	Average	PCA	RMS	0.0173	1593	1
FA	Average	ICA	RMS	0.0173	1593	<.0001
FA	Average	FA	RMS	0.0123	1593	0.9939
FA	Average	NMF	RMS	0.0173	1593	<.0001
FA	Average	PCA	SampEn	0.0173	1593	<.0001
FA	Average	ICA	SampEn	0.0173	1593	<.0001
FA	Average	FA	SampEn	0.0123	1593	<.0001
FA	Average	NMF	SampEn	0.0173	1593	0.9993
NMF	Average	PCA	RMS	0.0173	1593	<.0001
NMF	Average	ICA	RMS	0.0173	1593	<.0001
NMF	Average	FA	RMS	0.0173	1593	<.0001
NMF	Average	NMF	RMS	0.0123	1593	0.9939
NMF	Average	PCA	SampEn	0.0173	1593	<.0001
NMF	Average	ICA	SampEn	0.0173	1593	<.0001
NMF	Average	FA	SampEn	0.0173	1593	<.0001
NMF	Average	NMF	SampEn	0.0123	1593	<.0001
PCA	RMS	ICA	RMS	0.0123	1593	<.0001
PCA	RMS	FA	RMS	0.0123	1593	1
PCA	RMS	NMF	RMS	0.0123	1593	<.0001
PCA	RMS	PCA	SampEn	0.0123	1593	<.0001
PCA	RMS	ICA	SampEn	0.0173	1593	<.0001
PCA	RMS	FA	SampEn	0.0173	1593	<.0001
PCA	RMS	NMF	SampEn	0.0173	1593	1
ICA	RMS	FA	RMS	0.0123	1593	<.0001
ICA	RMS	NMF	RMS	0.0123	1593	<.0001
ICA	RMS	PCA	SampEn	0.0173	1593	<.0001
ICA	RMS	ICA	SampEn	0.0123	1593	<.0001
ICA	RMS	FA	SampEn	0.0173	1593	<.0001
ICA	RMS	NMF	SampEn	0.0173	1593	<.0001
FA	RMS	NMF	RMS	0.0123	1593	<.0001
FA	RMS	PCA	SampEn	0.0173	1593	<.0001
FA	RMS	ICA	SampEn	0.0173	1593	<.0001
FA	RMS	FA	SampEn	0.0123	1593	<.0001
FA	RMS	NMF	SampEn	0.0173	1593	1
NMF	RMS	PCA	SampEn	0.0173	1593	<.0001
NMF	RMS	ICA	SampEn	0.0173	1593	<.0001
NMF	RMS	FA	SampEn	0.0173	1593	<.0001
NMF	RMS	NMF	SampEn	0.0123	1593	<.0001
PCA	SampEn	ICA	SampEn	0.0123	1593	<.0001
PCA	SampEn	FA	SampEn	0.0123	1593	1
PCA	SampEn	NMF	SampEn	0.0123	1593	<.0001
ICA	SampEn	FA	SampEn	0.0123	1593	<.0001
ICA	SampEn	NMF	SampEn	0.0123	1593	<.0001
FA	SampEn	NMF	SampEn	0.0123	1593	<.0001

Appendix 1-B: **Pair wise comparisons following two-way ANOVA for mean cosine similarity values for synergy activation coefficients between synthetic synergies and extracted synergies for different synergy extraction algorithms and onset detection algorithms.** A two-way ANOVA was required to identify the effect of onset detection method and synergy extraction method on cosine similarity for synergy activation coefficients. Residuals were tested for normality using a histogram and a Levene's test for equal variance. There were statistically significant interactions between cosine similarity for both onset detection and between synergy extraction methods (F = 327.63, $p < 0.005$ and F = 276.45, $p < 0.005$ respectively). There was also a significant between group interaction for onset detection and synergy extraction (F = 25.31, $p <$ 0.005). This was followed by multiple within group comparisons to identify the simple main affects shown above.

Synergy extraction 1	Onset detection 1	Synergy extraction 2	Onset detection 2	Standard Error	Degrees of freedom	P value
PCA	Raw	ICA	Raw	0.017497	1593	1
PCA	Raw	FA	Raw	-0.04354	1593	0.828
PCA	Raw	NMF	Raw	-0.07526	1593	0.0473
PCA	Raw	PCA	Average	0.007083	1593	1
PCA	Raw	ICA	Average	0.02458	1593	1
PCA	Raw	FA	Average	-0.03646	1593	0.9986
PCA	Raw	NMF	Average	-0.06818	1593	0.6907
PCA	Raw	PCA	RMS	0.022594	1593	0.9997
PCA	Raw	ICA	RMS	0.040091	1593	0.996
PCA	Raw	FA	RMS	-0.02095	1593	1
PCA	Raw	NMF	RMS	-0.05267	1593	0.9453
PCA	Raw	PCA	SampEn	0.097099	1593	0.001
PCA	Raw	ICA	SampEn	0.114596	1593	0.0194
PCA	Raw	FA	SampEn	0.053559	1593	0.9373
PCA	Raw	NMF	SampEn	0.021836	1593	1
ICA	Raw	FA	Raw	-0.06104	1593	0.2716
ICA	Raw	NMF	Raw	-0.09276	1593	0.0024
ICA	Raw	PCA	Average	-0.01041	1593	1
ICA	Raw	ICA	Average	0.007083	1593	1
ICA	Raw	FA	Average	-0.05395	1593	0.9335
ICA	Raw	NMF	Average	-0.08568	1593	0.2839
ICA	Raw	PCA	RMS	0.005097	1593	1
ICA	Raw	ICA	RMS	0.022594	1593	0.9997
ICA	Raw	FA	RMS	-0.03844	1593	0.9974
ICA	Raw	NMF	RMS	-0.07017	1593	0.6436
ICA	Raw	PCA	SampEn	0.079602	1593	0.4139
ICA	Raw	ICA	SampEn	0.097099	1593	0.001
ICA	Raw	FA	SampEn	0.036062	1593	0.9988
ICA	Raw	NMF	SampEn	0.00434	1593	1
FA	Raw	NMF	Raw	-0.03172	1593	0.9871
FA	Raw	PCA	Average	0.050624	1593	0.9608
FA	Raw	ICA	Average	0.06812	1593	0.692
FA	Raw	FA	Average	0.007083	1593	1
FA	Raw	NMF	Average	-0.02464	1593	1
FA	Raw	PCA	RMS	0.066134	1593	0.7368
FA	Raw	ICA	RMS	0.083631	1593	0.3249
FA	Raw	FA	RMS	0.022594	1593	0.9997
FA	Raw	NMF	RMS	-0.00913	1593	1
FA	Raw	PCA	SampEn	0.140639	1593	0.0006
FA	Raw	ICA	SampEn	0.158136	1593	<.0001
FA	Raw	FA	SampEn	0.097099	1593	0.001
FA	Raw	NMF	SampEn	0.065377	1593	0.7532
NMF	Raw	PCA	Average	0.082346	1593	0.3522
NMF	Raw	ICA	Average	0.099843	1593	0.0905
NMF	Raw	FA	Average	0.038805	1593	0.9972
NMF	Raw	NMF	Average	0.007083	1593	1
NMF	Raw	PCA	RMS	0.097856	1593	0.1084
NMF	Raw	ICA	RMS	0.115353	1593	0.0178
NMF	Raw	FA	RMS	0.054316	1593	0.9299
NMF	Raw	NMF	RMS	0.022594	1593	0.9997
NMF	Raw	PCA	SampEn	0.172361	1593	<.0001
NMF	Raw	ICA	SampEn	0.189858	1593	<.0001
NMF	Raw	FA	SampEn	0.128821	1593	0.0033
NMF	Raw	NMF	SampEn	0.097099	1593	0.001
PCA	Average	ICA	Average	0.017497	1593	1
PCA	Average	FA	Average	-0.04354	1593	0.828
PCA	Average	NMF	Average	-0.07526	1593	0.0473
PCA	Average	PCA	RMS	0.015511	1593	1
PCA	Average	ICA	RMS	0.033007	1593	0.9996
PCA	Average	FA	RMS	-0.02803	1593	0.9999
PCA	Average	NMF	RMS	-0.05975	1593	0.8589
PCA	Average	PCA	SampEn	0.090015	1593	0.004
PCA	Average	ICA	SampEn	0.107512	1593	0.0423
PCA	Average	FA	SampEn	0.046475	1593	0.9819
PCA	Average	NMF	SampEn	0.014753	1593	1
ICA	Average	FA	Average	-0.06104	1593	0.2716
ICA	Average	NMF	Average	-0.09276	1593	0.0024
ICA	Average	PCA	RMS	-0.00199	1593	1
ICA	Average	ICA	RMS	0.015511	1593	1
ICA	Average	FA	RMS	-0.04553	1593	0.9852
ICA	Average	NMF	RMS	-0.07725	1593	0.4698
ICA	Average	PCA	SampEn	0.072519	1593	0.5861
ICA	Average	ICA	SampEn	0.090015	1593	0.004

ICA	Average	FA	SampEn	0.028978	1593	0.9999
ICA	Average	NMF	SampEn	-0.00274	1593	1
FA	Average	NMF	Average	-0.03172	1593	0.9871
FA	Average	PCA	RMS	0.059051	1593	0.8698
FA	Average	ICA	RMS	0.076548	1593	0.4868
FA	Average	FA	RMS	0.015511	1593	1
FA	Average	NMF	RMS	-0.01621	1593	1
FA	Average	PCA	SampEn	0.133556	1593	0.0017
FA	Average	ICA	SampEn	0.151052	1593	0.0001
FA	Average	FA	SampEn	0.090015	1593	0.004
FA	Average	NMF	SampEn	0.058293	1593	0.881
NMF	Average	PCA	RMS	0.090773	1593	0.196
NMF	Average	ICA	RMS	0.10827	1593	0.0391
NMF	Average	FA	RMS	0.047233	1593	0.979
NMF	Average	NMF	RMS	0.015511	1593	1
NMF	Average	PCA	SampEn	0.165278	1593	<.0001
NMF	Average	ICA	SampEn	0.182775	1593	<.0001
NMF	Average	FA	SampEn	0.121738	1593	0.0082
NMF	Average	NMF	SampEn	0.090015	1593	0.004
PCA	RMS	ICA	RMS	0.017497	1593	1
PCA	RMS	FA	RMS	-0.04354	1593	0.828
PCA	RMS	NMF	RMS	-0.07526	1593	0.0473
PCA	RMS	PCA	SampEn	0.074505	1593	0.0528
PCA	RMS	ICA	SampEn	0.092002	1593	0.178
PCA	RMS	FA	SampEn	0.030965	1593	0.9998
PCA	RMS	NMF	SampEn	-0.00076	1593	1
ICA	RMS	FA	RMS	-0.06104	1593	0.2716
ICA	RMS	NMF	RMS	-0.09276	1593	0.0024
ICA	RMS	PCA	SampEn	0.057008	1593	0.8987
ICA	RMS	ICA	SampEn	0.074505	1593	0.0528
ICA	RMS	FA	SampEn	0.013468	1593	1
ICA	RMS	NMF	SampEn	-0.01825	1593	1
FA	RMS	NMF	RMS	-0.03172	1593	0.9871
FA	RMS	PCA	SampEn	0.118045	1593	0.0129
FA	RMS	ICA	SampEn	0.135542	1593	0.0013
FA	RMS	FA	SampEn	0.074505	1593	0.0528
FA	RMS	NMF	SampEn	0.042783	1593	0.992
NMF	RMS	PCA	SampEn	0.149767	1593	0.0002
NMF	RMS	ICA	SampEn	0.167264	1593	<.0001
NMF	RMS	FA	SampEn	0.106227	1593	0.0484
NMF	RMS	NMF	SampEn	0.074505	1593	0.0528
PCA	SampEn	ICA	SampEn	0.017497	1593	1
PCA	SampEn	FA	SampEn	-0.04354	1593	0.828
PCA	SampEn	NMF	SampEn	-0.07526	1593	0.0473
ICA	SampEn	FA	SampEn	-0.06104	1593	0.2716
ICA	SampEn	NMF	SampEn	-0.09276	1593	0.0024
FA	SampEn	NMF	SampEn	-0.03172	1593	0.9871

Appendix 1-C: **Pair wise comparisons following two-way ANOVA for mean cosine similarity values for synergy vectors between synthetic synergies and extracted synergies for different synergy extraction algorithms and onset detection algorithms.** A two-way ANOVA was required to identify the effect of onset detection method and synergy extraction method on cosine similarity for synergy vector. Residuals were tested for normality using a histogram and a Levene's test for equal variance. There were statistically significant interactions between cosine similarity for both onset detection and between synergy extraction methods (). There was also a significant between group interaction for onset detection and synergy extraction (). This was followed by multiple within group comparisons to identify the simple main affects shown above.

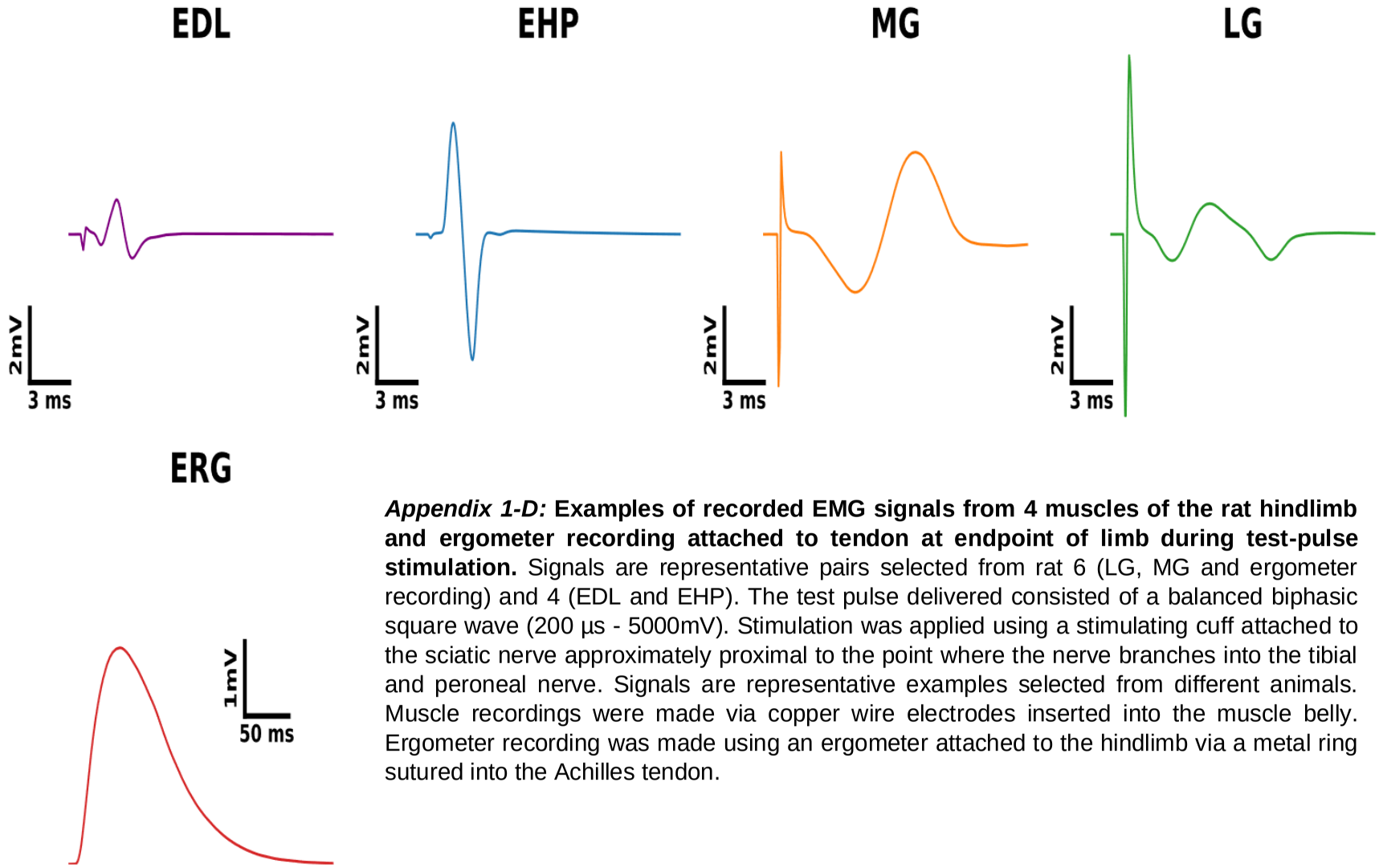

Appendix 1-D: **Examples of recorded EMG signals from 4 muscles of the rat hindlimb and ergometer recording attached to tendon at endpoint of limb during test-pulse stimulation.** Signals are representative pairs selected from rat 6 (LG, MG and ergometer recording) and 4 (EDL and EHP). The test pulse delivered consisted of a balanced biphasic square wave (200 µs - 5000mV). Stimulation was applied using a stimulating cuff attached to the sciatic nerve approximately proximal to the point where the nerve branches into the tibial and peroneal nerve. Signals are representative examples selected from different animals. Muscle recordings were made via copper wire electrodes inserted into the muscle belly. Ergometer recording was made using an ergometer attached to the hindlimb via a metal ring sutured into the Achilles tendon.

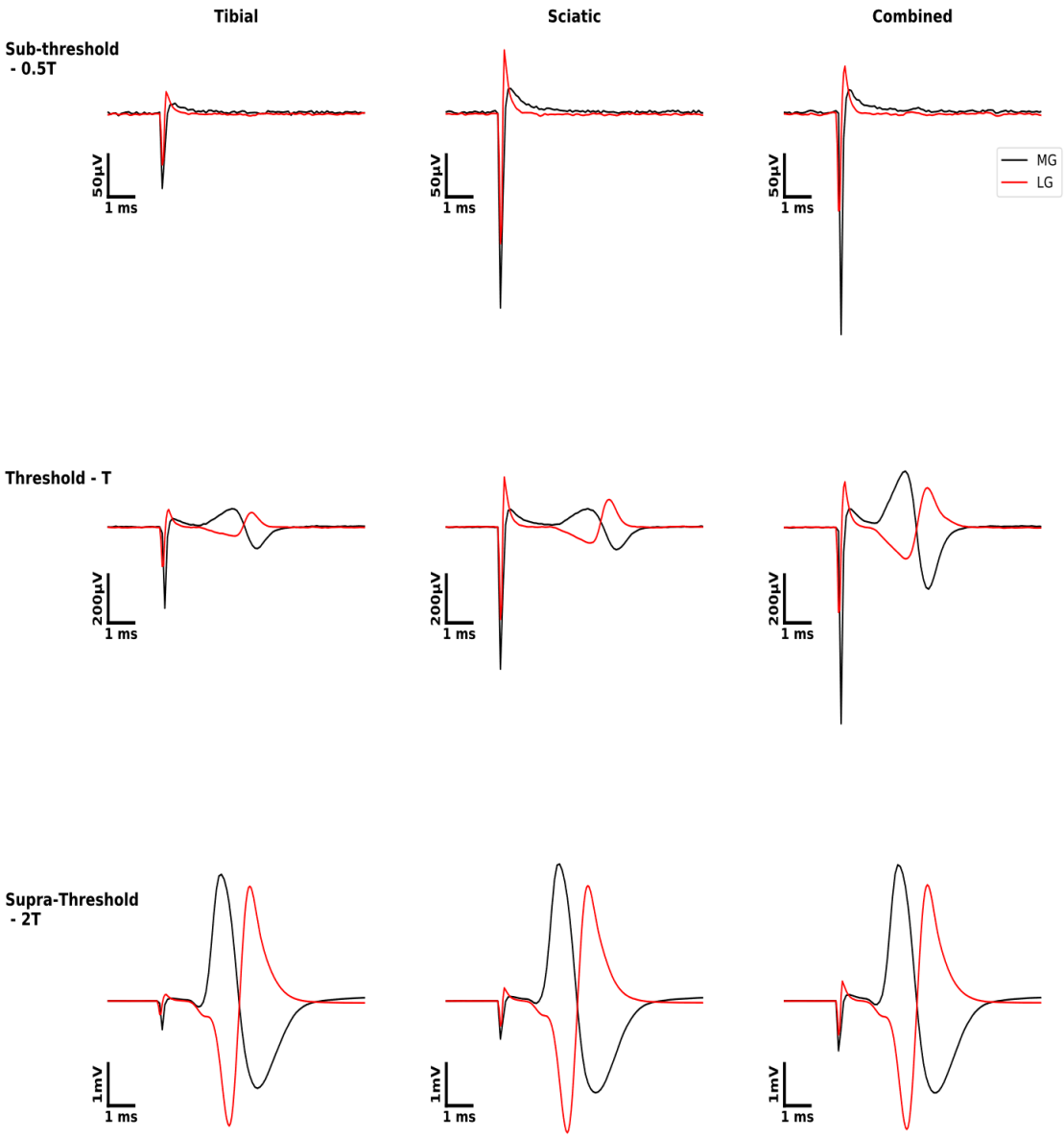

Appendix 1-E: **Subthreshold, threshold and supra-threshold stimulation of the rat peripheral nerve at two sites.** The rat peripheral nerve (rat 2) was stimulated using cuff electrodes attached to either the tibial or sciatic nerve. Stimulation was delivered to either the tibial cuff, sciatic cuff or to both cuffs combined. The stimulus delivered to either cuff in the combined condition was always equal. Threshold is defined as the shortest, smallest pulse that elicited a response. The threshold value differed depending on the cuff stimulated and are as follows; Sciatic 100 µs - 800mV, Tibial and Combined 100 µs - 600mV. Muscle activity was measured via copper wire electrodes inserted into MG and LG. Sub threshold signals are stimulus pulses that failed to elicit a response, the pulse shown here is 100 µs – 400mV and 100 µs – 300mV respectively, or half the threshold value. Supra-threshold values were defined as double the threshold value and are therefore 100 µs - 1600mV and 100 µs – 1200mV respectively.

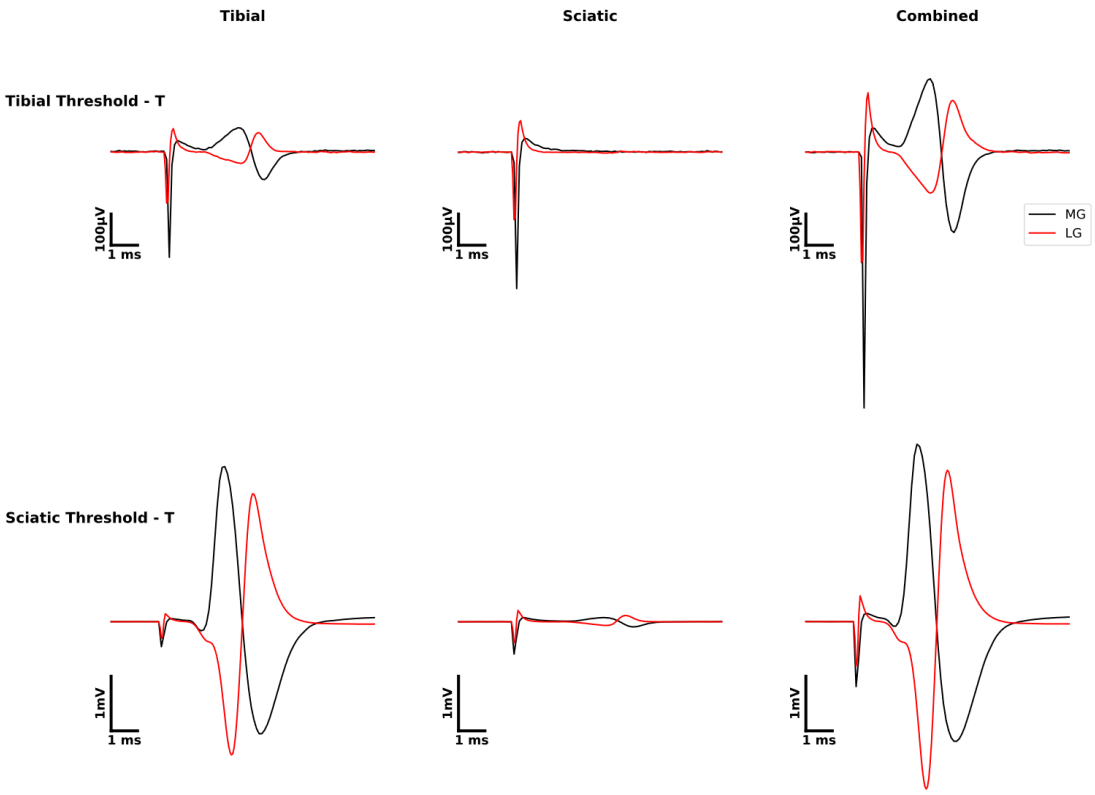

Appendix 1-F: **Comparison of stimulus at threshold value for different stimulating cuffs.** This graph compares the response of LG and MG at the determined threshold values for each cuff in rat 2. The sciatic and combined cuffs were determined to have the same minimum threshold activation (100 µs - 600mV). Note that this stimulus pulse elicits no response when delivered to the sciatic nerve (TOP MIDDLE). The tibial nerve threshold was higher (100 µs - 800mV) but it can be seen that stimulation at the sciatic or combined cuffs results in a significantly larger response. This demonstrates the greater selectivity of the tibial cuff for LG/MG recruitment. It is also possible to observe the additive effect on recruitment in the combined trace at Tibial threshold value. Stimulation was delivered either to the tibial cuff, sciatic cuff or to both cuffs combined. The stimulus delivered to either cuff in the combined condition was always equal. Muscle activity was measured via copper wire electrodes inserted into MG and LG.

References

Alam, M., Rodrigues, W., Pham, B.N. and Thakor, N. V 2016. Brain Machine Interface-facilitated Neurorehabilitation via Spinal Stimulation after Spinal Cord Injury: Recent Progress and Future Perspectives. *Brain Research*. **1646**, pp.25–33.

Alwosheel, A., van Cranenburgh, S. and Chorus, C.G. 2018. Is your dataset big enough? Sample size requirements when using artificial neural networks for discrete choice analysis. *Journal of Choice Modelling*.

Antuvan, C.W., Bisio, F., Marini, F., Yen, S.-C., Cambria, E. and Masia, L. 2016. Role of Muscle Synergies in Real-Time Classification of Upper Limb Motions using Extreme Learning Machines. *Journal of NeuroEngineering and Rehabilitation*. **13**(1), p.76.

Asghari Oskoei, M. and Hu, H. 2007. Myoelectric control systems-A survey. *Biomedical Signal Processing and Control*. **2**(4), pp.275–294.

Atzori, M., Gijsberts, A., Castellini, C., Caputo, B., Hager, A.-G.M., Elsig, S., Giatsidis, G., Bassetto, F. and Müller, H. 2014. Electromyography data for non-invasive naturally-controlled robotic hand prostheses. *Scientific data*. **1**, p.140053.

Avendaño-Coy, J., Gómez-Soriano, J., Goicoechea-García, C., Basco-López, J.A. and Taylor, J. 2017. Effect of Unmodulated 5-kHz Alternating Currents Versus Transcutaneous Electrical Nerve Stimulation on Mechanical and Thermal Pain, Tactile Threshold, and Peripheral Nerve Conduction: A Double-Blind, Placebo-Controlled Crossover Trial. *Archives of Physical Medicine and Rehabilitation*.

Baranauskas, G. 2014. What limits the performance of current invasive brain machine interfaces? *Frontiers in systems neuroscience*. **8**(APR), p.68.

Barbeau, H., McCrea, D.A., O'Donovan, M.J., Rossignol, S., Grill, W.M. and Lemay, M.A. 1999. Tapping into spinal circuits to restore motor function. *Brain Research Reviews*. **30**(1), pp.27–51.

Bartholomew, D.J., Steele, F., Galbraith, J. and Moustaki, I. 2008. *Analysis of multivariate social science data, second edition*.

Baum, E.B. and Haussler, D. 1989. What Size Net Gives Valid Generalization? *Neural Computation*.

Benabid, A.L. 2003. Deep brain stimulation for Parkinson's disease. *Current Opinion in*

Neurobiology.

Bernstein, N. 1968. *The co-ordination and regulation of movements* [Online]. Oxford. [Accessed 22 March 2019]. Available from: http://linkinghub.elsevier.com/retrieve/pii/0022510X68901664.

Berry, M.W., Browne, M., Langville, A.N., Pauca, V.P. and Plemmons, R.J. 2007. Algorithms and applications for approximate nonnegative matrix factorization. *Computational Statistics and Data Analysis*.

Bigland-Ritchie, B. 1981. EMG/force relations and fatigue of human voluntary contractions. *Exercise and Sport Sciences Reviews*.

Bizzi, E. and Cheung, V.C.K. 2013. The neural origin of muscle synergies. *Frontiers in computational neuroscience*. **7**(April), p.51.

Bizzi, E., Mussa-Ivaldi, F.A. and Giszter, S. 1991. Computations underlying the execution of movement: a biological perspective. *Science*. **253**(5017), 287 LP – 291.

Blair, E.A. and Erlanger, J. 1933. A COMPARISON OF THE CHARACTERISTICS OF AXONS THROUGH THEIR INDIVIDUAL ELECTRICAL RESPONSES. *American Journal of Physiology-Legacy Content*.

Bostock, H. 1983. The strength-duration relationship for excitation of myelinated nerve: computed dependence on membrane parameters. *The Journal of Physiology*.

Bostock, H. and Bergmans, J. 1994. Post-tetanic excitability changes and ectopic discharges in a human motor axon. *Brain*.

Bostock, H., Cikurel, K. and Burke, D. 1998. Threshold tracking techniques in the study of human peripheral nerve. *Muscle & nerve*. **21**(2), pp.137–158.

Bouton, C.E., Shaikhouni, A., Annetta, N. V., Bockbrader, M.A., Friedenberg, D.A., Nielson, D.M., Sharma, G., Sederberg, P.B., Glenn, B.C., Mysiw, W.J., Morgan, A.G., Deogaonkar, M. and Rezai, A.R. 2016. Restoring cortical control of functional movement in a human with quadriplegia. *Nature*. **000**(7602), pp.1–13.

Boutsidis, C. and Gallopoulos, E. 2008. SVD based initialization: A head start for nonnegative matrix factorization. *Pattern Recognition*. **41**(4), pp.1350–1362.

Branner, A. and Normann, R.A. 2000. A multielectrode array for intrafascicular

recording and stimulation in sciatic nerve of cats. *Brain Research Bulletin*.

Brezina, V., Orekhova, I. V and Weiss, K.R. 2000. The neuromuscular transform: the dynamic, nonlinear link between motor neuron firing patterns and muscle contraction in rhythmic behaviors. *Journal of neurophysiology*. **83**(1), pp.207–231.

Brismar, T. 1981. Electrical properties of isolated demyelinated rat nerve fibres. *Acta Physiologica Scandinavica*.

Brus-Ramer, M., Carmel, J.B., Chakrabarty, S. and Martin, J.H. 2007. Electrical Stimulation of Spared Corticospinal Axons Augments Connections with Ipsilateral Spinal Motor Circuits after Injury. *Journal of Neuroscience*. **27**(50), pp.13793–13801.

Buchanan, T.S., Almdale, D.P.J., Lewis, J.L. and Rymer, W.Z. 1986. Characteristics of synergic relations during isometric contractions of human elbow muscles. *Journal of Neurophysiology*.

Campos, L.W., Chakrabarty, S., Haque, R. and Martin, J.H. 2008. Regenerating Motor Bridge Axons Refine Connections and Synapse on Lumbar Motoneurons to Bypass Chronic Spinal Cord Injury. *The Journal of comparative neurology*. **506**, pp.838–850.

Capogrosso, M., Milekovic, T., Borton, D., Wagner, F., Martin Moraud, E., Mignardot, J.-B., Buse, N., Gandar, J., Barraud, Q., Xing, D., Rey, E., Duis, S., Jianzhong, Y., Li, W.K.D.K.Q., Detemple, P., Denison, T., Micera, S., Bezard, E., Bloch, J. and Courtine, G. 2016. A brain-spinal interface alleviating gait deficits after spinal cord injury in primates. *Nature*. **In Press**(7628), pp.284–288.

Chang, B.S. 2018. Deep brain stimulation works for drug-resistant epilepsy, but how? *Epilepsy Currents*.

Cheung, V.C.K., Turolla, A., Agostini, M., Silvoni, S., Bennis, C., Kasi, P., Paganoni, S., Bonato, P. and Bizzi, E. 2012. Muscle synergy patterns as physiological markers of motor cortical damage. *Proceedings of the National Academy of Sciences of the United States of America*.

Comon, P. 1994. Independent component analysis, A new concept? *Signal Processing*.

Daly, J.J. and Huggins, J.E. 2015. Brain-computer interface: Current and emerging

rehabilitation applications. *Archives of Physical Medicine and Rehabilitation*.

Damiano, D.L., Prosser, L.A., Curatalo, L.A. and Alter, K.E. 2013. Muscle plasticity and ankle control after repetitive use of a functional electrical stimulation device for foot drop in cerebral palsy. *Neurorehabilitation and Neural Repair*.

Darby, S.A. and Frysztak, R.J. 2013. Neuroanatomy of the Spinal Cord *In*: *Clinical Anatomy of the Spine, Spinal Cord, and ANS*.

Davis, T.S., Wark, H.A.C., Hutchinson, D.T., Warren, D.J., O'Neill, K., Scheinblum, T., Clark, G.A., Normann, R.A. and Greger, B. 2016. Restoring motor control and sensory feedback in people with upper extremity amputations using arrays of 96 microelectrodes implanted in the median and ulnar nerves. *Journal of Neural Engineering*.

Dimitrov, G. V. and Dimitrova, N.A. 1998. Precise and fast calculation of the motor unit potentials detected by a point and rectangular plate electrode. *Medical Engineering and Physics*.

Dominici, N., Ivanenko, Y.P., Cappellini, G., d'Avella, A., Mondi, V., Cicchese, M., Fabiano, A., Silei, T., Di Paolo, A., Giannini, C., Poppele, R.E. and Lacquaniti, F. 2011. Locomotor Primitives in Newborn Babies and Their Development. *Science*. **334**(6058), pp.997–999.

Donoho, D. and Stodden, V. 2004. When does non-negative matrix factorization give a correct decomposition into parts? *In*: *Advances in Neural Information Processing Systems*.

Dorn, J.D., Ahuja, A.K., Caspi, A., da Cruz, L., Dagnelie, G., Sahel, J.-A., Greenberg, R.J. and McMahon, M.J. 2012. The Detection of Motion by Blind Subjects With the Epiretinal 60-Electrode (Argus II) Retinal Prosthesis. *Archives of ophthalmology*. (Argus II), pp.1–7.

Doss, W.S. and Karpovich, P. V. 1965. A comparison of concentric, eccentric, and isometric strength of elbow flexors. *Journal of Applied Physiology*.

Dubin, A.E. and Patapoutian, A. 2010. Nociceptors: The sensors of the pain pathway. *Journal of Clinical Investigation*.

Dura-Bernal, S., Li, K., Neymotin, S.A., Francis, J.T., Principe, J.C. and Lytton, W.W. 2016. Restoring Behavior via Inverse Neurocontroller in a Lesioned Cortical

Spiking Model Driving a Virtual Arm. *Frontiers in Neuroscience*. **10**(February), pp.1–17.

von Düring, M. and Andres, K.H. 1990. Topography and Ultrastructure of Group III and IV Nerve Terminals of the Cat's Gastrocnemius-Soleus Muscle *In*: *The Primary Afferent Neuron*.

Duysens, J., De Groote, F. and Jonkers, I. 2013. The flexion synergy, mother of all synergies and father of new models of gait. *Frontiers in Computational Neuroscience*.

Ebied, A., Kinney-Lang, E., Spyrou, L. and Escudero, J. 2018. Evaluation of matrix factorisation approaches for muscle synergy extraction. *Medical Engineering and Physics*.

Eccles, J.C., Eccles, R.M. and Lundberg, A. 1957. The convergence of monosynaptic excitatory afferents on to many different species of alpha motoneurones. *The Journal of physiology*.

Eftekhar, A., Paraskevopoulou, S.E. and Constandinou, T.G. 2010. Towards a next generation neural interface: Optimizing power, bandwidth and data quality *In*: *2010 IEEE Biomedical Circuits and Systems Conference, BioCAS 2010*., pp.122–125.

Elbasiouny, S.M., Moroz, D., Bakr, M.M. and Mushahwar, V.K. 2010. Management of Spasticity After Spinal Cord Injury: Current Techniques and Future Directions. *Neurorehabilitation and Neural Repair*.

Embrey, D.G., Holtz, S.L., Alon, G., Brandsma, B.A. and McCoy, S.W. 2010. Functional Electrical Stimulation to Dorsiflexors and Plantar Flexors During Gait to Improve Walking in Adults With Chronic Hemiplegia. *Archives of Physical Medicine and Rehabilitation*. **91**(5), pp.687–696.

Estigoni, E.H., Fornusek, C., Hamzaid, N.A., Hasnan, N., Smith, R.M. and Davis, G.M. 2014. Evoked EMG versus muscle torque during fatiguing functional electrical stimulation-evoked muscle contractions and short-term recovery in individuals with spinal cord injury. *Sensors (Switzerland)*.

Fang, Z.P. and Mortimer, J.T. 1991. Selective Activation of Small Motor Axons by Quasitrapezoidal Current Pulses. *IEEE Transactions on Biomedical Engineering*.

Ferrante, S., Chia Bejarano, N., Ambrosini, E., Nardone, A., Turcato, A.M., Monticone, M., Ferrigno, G. and Pedrocchi, A. 2016. A Personalized Multi-Channel FES Controller Based on Muscle Synergies to Support Gait Rehabilitation after Stroke. *Frontiers in Neuroscience*. **10**, p.425.

Field-Fote, E.C. 2001. Combined use of body weight support, functional electric stimulation, and treadmill training to improve walking ability in individuals with chronic incomplete spinal cord injury. *Archives of Physical Medicine and Rehabilitation*.

Fitts, P.M. 1954. The information capacity of the human motor system in controlling the amplitude of movement. *Journal of Experimental Psychology*. **47**(6), pp.381–391.

Flint, R.D., Wright, Z.A., Scheid, M.R. and Slutzky, M.W. 2013. Long term, stable brain machine interface performance using local field potentials and multiunit spikes. *Journal of Neural Engineering*.

Frère, J. and Hug, F. 2012. Between-subject variability of muscle synergies during a complex motor skill. *Frontiers in Computational Neuroscience*.

Furui, A., Eto, S., Nakagaki, K., Shimada, K., Nakamura, G., Masuda, A., Chin, T. and Tsuji, T. 2019. A myoelectric prosthetic hand with muscle synergy–based motion determination and impedance model–based biomimetic control. *Science Robotics*.

Gandevia, S.C., Macefield, G., Burke, D. and Mckenzie, D.K. 1990. Voluntary activation of human motor axons in the absence of muscle afferent feedback: The control of the deafferented hand. *Brain*.

Gesslbauer, B., Hruby, L.A., Roche, A.D., Farina, D., Blumer, R. and Aszmann, O.C. 2017. Axonal components of nerves innervating the human arm. *Annals of Neurology*.

Giagka, V., Eder, C., Valente, V., Vanhoestenberghe, A., Donaldson, N. and Demosthenous, A. 2013. A dedicated electrode driving ASIC for epidural spinal cord stimulation in rats. *Proceedings of the IEEE International Conference on Electronics, Circuits, and Systems*., pp.469–472.

Gilja, V., Nuyujukian, P., Chestek, C.A., Cunningham, J.P., Yu, B.M., Fan, J.M., Churchland, M.M., Kaufman, M.T., Kao, J.C., Ryu, S.I. and Shenoy, K. V 2012. A high-performance neural prosthesis enabled by control algorithm design. *Nature*

Neuroscience. **15**(12), pp.1752–7.

Giuffrida, J.P. and Crago, P.E. 2005. Functional restoration of elbow extension after spinal-cord injury using a neural network-based synergistic FES controller. *IEEE Transactions on Neural Systems and Rehabilitation Engineering*.

Grahn, P.J., Mallory, G.W., Michael Berry, B., Hachmann, J.T., Lobel, D.A. and Luis Lujan, J. 2014. Restoration of motor function following spinal cord injury via optimal control of intraspinal microstimulation: Toward a next generation closed-loop neural prosthesis. *Frontiers in Neuroscience*. **8**(SEP), pp.1–12.

Griep, P.A.M., Boon, K.L. and Stegeman, D.F. 1978. A study of the motor unit action potential by means of computer simulation. *Biological Cybernetics*.

Grillner, S. 2011. Control of Locomotion in Bipeds, Tetrapods, and Fish *In*: *Comprehensive Physiology*.

Grillner, S. 1985. Neurobiological bases of rhythmic motor acts in vertebrates. *Science (New York, N.Y.)*. **228**(4696), pp.143–9.

Groote, F. De, Jonkers, I. and Duysens, J. 2014. Task constraints and minimization of muscle effort result in a small number of muscle synergies during gait. *Frontiers in Computational Neuroscience*.

Guertin, P.A. 2013. Central pattern generator for locomotion: Anatomical, physiological, and pathophysiological considerations. *Frontiers in Neurology*.

Halevy, A., Norvig, P. and Pereira, F. 2009. The unreasonable effectiveness of data. *IEEE Intelligent Systems*.

Hart, Corey B and Giszter, S.F. 2010. A neural basis for motor primitives in the spinal cord. *The Journal of neuroscience : the official journal of the Society for Neuroscience*. **30**(4), pp.1322–1336.

Hart, Corey B. and Giszter, S.F. 2010. A neural basis for motor primitives in the spinal cord. *Journal of Neuroscience*.

Haykin, S. 2008. *Neural Networks and Learning Machines*.

Henneman, E., Somjen, G. and Carpenter, D.O. 1965. Excitability and inhibitability of motoneurons of different sizes. *Journal of neurophysiology*.

Hincapié, J.G., Blana, D., Chadwick, E. and Kirsch, R.F. 2005. Neural network

controller for an upper extremity neuroprosthesis *In*: *2nd International IEEE EMBS Conference on Neural Engineering*.

Hincapie, J.G. and Kirsch, R.F. 2009. Feasibility of EMG-based neural network controller for an upper extremity neuroprosthesis *In*: *IEEE Transactions on Neural Systems and Rehabilitation Engineering*.

Hirashima, M. and Oya, T. 2016. How does the brain solve muscle redundancy? Filling the gap between optimization and muscle synergy hypotheses. *Neuroscience Research*.

Ho, C.H., Triolo, R.J., Elias, A.L., Kilgore, K.L., DiMarco, A.F., Bogie, K., Vette, A.H., Audu, M.L., Kobetic, R., Chang, S.R., Chan, K.M., Dukelow, S., Bourbeau, D.J., Brose, S.W., Gustafson, K.J., Kiss, Z.H.T. and Mushahwar, V.K. 2014. Functional electrical stimulation and Spinal Cord Injury. *Physical Medicine and Rehabilitation Clinics of North America*.

Hotelling, H. 1933. Analysis of a complex of statistical variables into principal components. *Journal of Educational Psychology*.

Hultborn, H., Meunier, S., Pierrot-Deseilligny, E. and Shindo, M. 1987. Changes in presynaptic inhibition of Ia fibres at the onset of voluntary contraction in man. *The Journal of Physiology*.

Hyvärinen, A. and Oja, E. 2000. Independent component analysis: Algorithms and applications. *Neural Networks*.

Israely, S., Leisman, G., Machluf, C.C. and Carmeli, E. 2018. Muscle synergies control during hand-reaching tasks in multiple directions post-stroke. *Frontiers in Computational Neuroscience*.

Jackson, A. and Fetz, E.E. 2011. Interfacing with the Computational Brain. *IEEE Transactions on Neural Systems and Rehabilitation Engineering*. **19**(5), pp.534–541.

Jackson, A., Moritz, C.T., Mavoori, J., Lucas, T.H. and Fetz, E.E. 2006. The neurochip BCI: Towards a neural prosthesis for upper limb function. *IEEE Transactions on Neural Systems and Rehabilitation Engineering*. **14**(2), pp.187–190.

Jankowska, E., Jukes, M.G.M., Lund, S. and Lundberg, A. 1967. The Effect of DOPA on the Spinal Cord 5. Reciprocal organization of pathways transmitting excitatory

action to alpha motoneurones of flexors and extensors. *Acta Physiologica Scandinavica*.

Jankowski, M.P., Rau, K.K., Ekmann, K.M., Anderson, C.E. and Koerber, H.R. 2013. Comprehensive phenotyping of group III and IV muscle afferents in mouse. *Journal of Neurophysiology*.

Jones, D.A., Bigland-Ritchie, B. and Edwards, R.H.T. 1979. Excitation frequency and muscle fatigue: Mechanical responses during voluntary and stimulated contractions. *Experimental Neurology*.

de Kamps, M., Baier, V., Drever, J., Dietz, M., Mösenlechner, L. and van der Velde, F. 2008. The state of MIIND. *Neural Networks*.

de Kamps, M., Lepperød, M. and Lai, Y.M. 2019. Computational geometry for modeling neural populations: From visualization to simulation B. S. Gutkin, ed. *PLOS Computational Biology*. **15**(3), p.e1006729.

Kapadia, N., Masani, K., Craven, B.C., Giangregorio, L.M., Hitzig, S.L., Richards, K. and Popovic, M.R. 2014. A randomized trial of functional electrical stimulation for walking in incomplete spinal cord injury: Effects on walking competency. *Journal of Spinal Cord Medicine*.

Kesar, T.M., Reisman, D.S., Perumal, R., Jancosko, A.M., Higginson, J.S., Rudolph, K.S. and Binder-Macleod, S.A. 2011. Combined effects of fast treadmill walking and functional electrical stimulation on post-stroke gait. *Gait & Posture*. **33**(2), pp.309–313.

Kim, Y., Cho, H.J. and Park, H.S. 2018. Technical development of transcutaneous electrical nerve inhibition using medium-frequency alternating current. *Journal of NeuroEngineering and Rehabilitation*.

Kindermans, P.J., Schreuder, M., Schrauwen, B., Müller, K.R. and Tangermann, M. 2014. True zero-training brain-computer interfacing - An online study. *PLoS ONE*.

Knikou, M. and Rymer, W. 2002. Effects of changes in hip joint angle on H-reflex excitability in humans. *Experimental Brain Research*.

Krauledat, M., Tangermann, M., Blankertz, B. and Müller, K.R. 2008. Towards zero training for brain-computer interfacing. *PLoS ONE*.

Kuramoto, Y. 1991. Collective synchronization of pulse-coupled oscillators and

excitable units. *Physica D: Nonlinear Phenomena*.

Kutch, J.J. and Valero-Cuevas, F.J. 2012. Challenges and new approaches to proving the existence of muscle synergies of neural origin. *PLoS Computational Biology*.

Kuypers, H.G.J.M. 1981. Anatomy of the Descending Pathways *In*: *Handbook of Physiology—The Nervous System II*.

De Labra, C., Guimaraes-Pinheiro, C., Maseda, A., Lorenzo, T. and Millán-Calenti, J.C. 2015. Effects of physical exercise interventions in frail older adults: A systematic review of randomized controlled trials Physical functioning, physical health and activity. *BMC Geriatrics*.

Lacquaniti, F., Ivanenko, Y.P. and Zago, M. 2012. Patterned control of human locomotion. *J Physiol*. **590**(Pt 10), pp.2189–2199.

Laforet, J., Guiraud, D. and Clerc, M. 2009. A toolchain to simulate and investigate selective stimulation strategies for FES *In*: *Proceedings of the 31st Annual International Conference of the IEEE Engineering in Medicine and Biology Society: Engineering the Future of Biomedicine, EMBC 2009*.

Lan, N., Feng, H.Q. and Crago, P.E. 1994. Neural Network Generation of Muscle Stimulation Patterns for Control of Arm Movements. *IEEE Transactions on Rehabilitation Engineering*.

Lee, D.D. and Seung, H.S. 2000. Algorithms for Non-negative Matrix Factorization *In*: *Proceedings of the 13th International Conference on Neural Information Processing Systems* [Online]. NIPS'00. Cambridge, MA, USA: MIT Press, pp.535–541. Available from: http://dl.acm.org/citation.cfm?id=3008751.3008829.

Lemon, R.N. 2008. Descending Pathways in Motor Control. *Annual Review of Neuroscience*.

Lertmanorat, Z. and Durand, D.M. 2004. Extracellular voltage profile for reversing the recruitment order of peripheral nerve stimulation: A simulation study. *Journal of Neural Engineering*.

Levine, A.J., Hinckley, C.A., Hilde, K.L., Driscoll, S.P., Poon, T.H., Montgomery, J.M. and Pfaff, S.L. 2014. Identification of a cellular node for motor control pathways. *Nature Neuroscience*. **17**(4), pp.586–593.

Liberson, W.T., Holmquest, H.J., Scot, D. and Dow, M. 1961. Functional

electrotherapy: stimulation of the peroneal nerve synchronized with the swing phase of the gait of hemiplegic patients. *Archives of physical medicine and rehabilitation*.

Lloyd, D.P.C. 1943. NEURON PATTERNS CONTROLLING TRANSMISSION OF IPSILATERAL HIND LIMB REFLEXES IN CAT. *Journal of Neurophysiology*.

Macefield, G., Gandevia, S.C. and Burke, D. 1989. Conduction velocities of muscle and cutaneous afferents in the upper and lower limbs of human subjects. *Brain*.

Marc, D.K. 2011. A New State of MIIND. *Frontiers in Neuroinformatics*.

Markin, S.N., Klishko, A.N., Shevtsova, N.A., Lemay, M.A., Prilutsky, B.I. and Rybak, I.A. 2012. A neuromechanical computational model of spinal control of locomotion. *BMC Neuroscience*.

Martin, J.H., Friel, K.M., Salimi, I. and Chakrabarty, S. 2007. Activity- and use-dependent plasticity of the developing corticospinal system. *Neuroscience and Biobehavioral Reviews*.

Maynard, E.M., Nordhausen, C.T. and Normann, R.A. 1997. The Utah Intracortical Electrode Array: A recording structure for potential brain-computer interfaces. *Electroencephalography and Clinical Neurophysiology*.

McCrea, D.A. and Rybak, I.A. 2008. Organization of mammalian locomotor rhythm and pattern generation. *Brain Research Reviews*.

McDermott, J.H. 2009. The cocktail party problem. *Current Biology*.

Mehryar, P. 2014. Neural Connectivity for Future Generation of Prosthetic Devices.

Melo, P.L., Silva, M.T., Martins, J.M. and Newman, D.J. 2015. Technical developments of functional electrical stimulation to correct drop foot: Sensing, actuation and control strategies. *Clinical Biomechanics*. **30**(2), pp.101–113.

Moe, J.H. and Post, H.W. 1962. Functional electrical stimulation for ambulation in hemiplegia. *The Journal-lancet*.

Mogyoros, I., Kiernan, M.C. and Burke, D. 1996. Strength-duration properties of human peripheral nerve. *Brain*.

Mori, S., Nishimura, H., Kurakami, C., Yamamura, T. and Aoki, M. 1978. Controlled locomotion in the mesencephalic cat: Distribution of facilitatory and inhibitory

regions within pontine tegmentum. *Journal of Neurophysiology*.

Nagi, S.S., Marshall, A.G., Makdani, A., Jarocka, E., Liljencrantz, J., Ridderström, M., Shaikh, S., O'Neill, F., Saade, D., Donkervoort, S., Reghan Foley, A., Minde, J., Trulsson, M., Cole, J., Bönnemann, C.G., Chesler, A.T., Catherine Bushnell, M., McGlone, F. and Olausson, H. 2019. An ultrafast system for signaling mechanical pain in human skin. *Science Advances*.

Nas, K., Yazmalar, L., Şah, V., Aydın, A. and Öneş, K. 2015. Rehabilitation of spinal cord injuries. *World journal of orthopedics*. **6**(1), pp.8–16.

Nielsen, J.B. and Sinkjaer, T. 2002. Afferent feedback in the control of human gait. *Journal of Electromyography and Kinesiology*.

Nishimura, Y., Perlmutter, S.I. and Fetz, E.E. 2013. Restoration of upper limb movement via artificial corticospinal and musculospinal connections in a monkey with spinal cord injury. *Frontiers in neural circuits*. **7**(April), p.57.

Nordhausen, C.T., Rousche, P.J. and Normann, R.A. 1994. Optimizing recording capabilities of the Utah Intracortical Electrode Array. *Brain Research*.

Otsu, N. 1979. THRESHOLD SELECTION METHOD FROM GRAY-LEVEL HISTOGRAMS. *IEEE Trans Syst Man Cybern*.

Pan, B., Sun, Y., Xie, B., Huang, Zhipei, Wu, J., Hou, J., Liu, Y., Huang, Zhen and Zhang, Z. 2018. Alterations of muscle synergies during voluntary arm reaching movement in subacute stroke survivors at different levels of impairment. *Frontiers in Computational Neuroscience*.

Pani, D., Barabino, G., Citi, L., Meloni, P., Raspopovich, S., Micera, S. and Raffo, L. 2016. Real-time neural signals decoding onto off-the-shelf DSP processors for neuroprosthetic applications. *IEEE Transactions on Neural Systems and Rehabilitation Engineering*. **XX**(XX), pp.1–1.

Panzeri, S., Macke, J.H., Gross, J. and Kayser, C. 2015. Neural population coding: combining insights from microscopic and mass signals. *Trends in cognitive sciences*. **19**(3), pp.162–72.

Pascual-Leone, A. 2013. Neuromotor recovery from stroke: computational models at central, functional, and muscle synergy level. *Frontiers in computational neuroscience*. **7**(August), p.97.

Pearson, K. 1901. LIII. On lines and planes of closest fit to systems of points in space . *The London, Edinburgh, and Dublin Philosophical Magazine and Journal of Science*.

Phinyomark, A., Quaine, F., Charbonnier, S., Serviere, C., Tarpin-bernard, F. and Laurillau, Y. 2013. EMG feature evaluation for improving myoelectric pattern recognition robustness. *Expert Systems With Applications*. **40**(12), pp.4832–4840.

Pierrot-Deseilligny, E. and Burke, D. 2005. *The circuitry of the human spinal cord: Its role in motor control and movement disorders*.

Pratt, C.A. and Jordan, L.M. 1987. Ia inhibitory interneurons and Renshaw cells as contributors to the spinal mechanisms of fictive locomotion. *Journal of Neurophysiology*.

Prentice, S.D., Patla, A.E. and Stacey, D.A. 2001. Artificial neural network model for the generation of muscle activation patterns for human locomotion. *Journal of Electromyography and Kinesiology*.

Rabischong, E. and Ohanna, F. 1992. Effects of functional electrical stimulation (FES) on evoked muscular output in paraplegic quadriceps muscle. *Paraplegia*.

Raikova, R., Krutki, P. and Celichowski, J. 2016. A general mathematical algorithm for predicting the course of unfused tetanic contractions of motor units in rat muscle. *PLoS ONE*.

Rainoldi, A., Melchiorri, G. and Caruso, I. 2004. A method for positioning electrodes during surface EMG recordings in lower limb muscles. *Journal of Neuroscience Methods*.

Raspopovic, S., Capogrosso, M., Petrini, F.M., Bonizzato, M., Rigosa, J., Di Pino, G., Carpaneto, J., Controzzi, M., Boretius, T., Fernandez, E., Granata, G., Oddo, C.M., Citi, L., Ciancio, A.L., Cipriani, C., Carrozza, M.C., Jensen, W., Guglielmelli, E., Stieglitz, T., Rossini, P.M. and Micera, S. 2014. Restoring natural sensory feedback in real-time bidirectional hand prostheses. *Science translational medicine*. **6**(222), p.222ra19.

Richman, J.S. and Moorman, J.R. 2000. Physiological time-series analysis using approximate and sample entropy. *American Journal of Physiology - Heart and Circulatory Physiology*.

Riess, J.A. and Abbas, J.J. 2000. Adaptive neural network control of cyclic movements using functional neuromuscular stimulation. *IEEE Transactions on Rehabilitation Engineering*.

Rimini, D., Agostini, V. and Knaflitz, M. 2017. Intra-subject consistency during locomotion: Similarity in shared and subject-specific muscle synergies. *Frontiers in Human Neuroscience*.

Rodriguez-Falces, J., Navallas, J. and Mal, A. 2012. EMG Modeling *In*: *Computational Intelligence in Electromyography Analysis - A Perspective on Current Applications and Future Challenges*.

Roh, J., Rymer, W.Z. and Beer, R.F. 2012. Robustness of muscle synergies underlying three-dimensional force generation at the hand in healthy humans. *Journal of neurophysiology*. **107**(8), pp.2123–42.

Rybak, I.A., Dougherty, K.J. and Shevtsova, N.A. 2015. Organization of the mammalian locomotor CPG: Review of computational model and circuit architectures based on genetically identified spinal interneurons. *eNeuro*.

Safavynia, S., Torres-Oviedo, G. and Ting, L. 2011. Muscle Synergies: Implications for Clinical Evaluation and Rehabilitation of Movement. *Topics in Spinal Cord Injury Rehabilitation*. **17**(1), pp.16–24.

Saltiel, P., Tresch, M.C. and Bizzi, E. 1998. Spinal cord modular organization and rhythm generation: An NMDA iontophoretic study in the frog. *Journal of Neurophysiology*.

Saltiel, P., Wyler-Duda, K., D'Avella, A., Tresch, M.C. and Bizzi, E. 2001. Muscle synergies encoded within the spinal cord: Evidence from focal intraspinal NMDA iontophoresis in the frog. *Journal of Neurophysiology*.

Sauermann, S., Rafolt, D., Bijak, M., Unger, E., Lanmueller, H., Weigel, G., Girsch, W. and Mayr, W. 2007. Objective assessment of the fusion frequency in functional electrical stimulation using the fast Fourier transform. *Biomedizinische Technik*.

Shanechi, M.M., Hu, R.C. and Williams, Z.M. 2014. A cortical-spinal prosthesis for targeted limb movement in paralyzed primate avatars Maryam. *Nat Commun*., pp.37–54.

Sherrington, C.S. 1910. Flexion-reflex of the limb, crossed extension-reflex, and reflex

stepping and standing. *The Journal of Physiology*.

Sherrington, C.S. 1909. ON PLASTIC TONUS AND PROPRIOCEPTIVE REFLEXES. *Quarterly Journal of Experimental Physiology*.

Shevtsova, N.A., Hamade, K., Chakrabarty, S., Markin, S.N., Prilutsky, B.I. and Rybak, I.A. 2016. Modeling the Organization of Spinal Cord Neural Circuits Controlling Two-Joint Muscles *In*: Springer, New York, NY, pp.121–162. [Accessed 22 March 2019]. Available from: http://link.springer.com/10.1007/978-1-4939-3267-2_5.

Shik, M.L. and Orlovsky, G.N. 1976. Neurophysiology of locomotor automatism. *Physiological Reviews*.

Singh, K., Richmond, F.J.R. and Loeb, G.E. 2000. Recruitment properties of intramuscular and nerve-trunk stimulating electrodes. *IEEE Transactions on Rehabilitation Engineering*.

Smith, C.C., Kissane, R.W.P. and Chakrabarty, S. 2018. Simultaneous assessment of homonymous and heteronymous monosynaptic reflex excitability in the adult rat. *eNeuro*.

So, K., Dangi, S., Orsborn, A.L., Gastpar, M.C. and Carmena, J.M. 2014. Subject-specific modulation of local field potential spectral power during brain-machine interface control in primates. *Journal of Neural Engineering*.

Sohn, M.H. and Ting, L.H. 2016. Suboptimal Muscle Synergy Activation Patterns Generalize their Motor Function across Postures. *Frontiers in computational neuroscience*. **10**, p.7.

Soukkio, P., Suikkanen, S., Kääriä, S., Kautiainen, H., Sipilä, S., Kukkonen-Harjula, K. and Hupli, M. 2018. Effects of 12-month home-based physiotherapy on duration of living at home and functional capacity among older persons with signs of frailty or with a recent hip fracture - Protocol of a randomized controlled trial (HIPFRA study). *BMC Geriatrics*.

Spüler, M., Irastorza-Landa, N., Sarasola-Sanz, A. and Ramos-Murguialday, A. 2016. Extracting muscle synergy patterns from EMG data using autoencoders *In*: *Lecture Notes in Computer Science (including subseries Lecture Notes in Artificial Intelligence and Lecture Notes in Bioinformatics)*.

Staude, G., Flachenecker, C., Daumer, M. and Wolf, W. 2001. Onset detection in

surface electromyographic signals: A systematic comparison of methods. *Eurasip Journal on Applied Signal Processing*.

Stavisky, S.D., Kao, J.C., Nuyujukian, P., Ryu, S.I. and Shenoy, K. V. 2015. A high performing brain-machine interface driven by low-frequency local field potentials alone and together with spikes. *Journal of Neural Engineering*.

Takei, T., Confais, J., Tomatsu, S., Oya, T. and Seki, K. 2017. Neural basis for hand muscle synergies in the primate spinal cord. *Proceedings of the National Academy of Sciences of the United States of America*.

Takei, T. and Seki, K. 2010. Spinal interneurons facilitate coactivation of hand muscles during a precision grip task in monkeys. *The Journal of neuroscience : the official journal of the Society for Neuroscience*. **30**(50), pp.17041–50.

Thomas, C.K., Griffin, L., Godfrey, S., Ribot-Ciscar, E. and Butler, J.E. 2003. Fatigue of paralyzed and control thenar muscles induced by variable or constant frequency stimulation. *Journal of Neurophysiology*.

Torres-Oviedo, G., Macpherson, J.M. and Ting, L.H. 2006. Muscle Synergy Organization Is Robust Across a Variety of Postural Perturbations. *Journal of Neurophysiology*. **96**(3), pp.1530–1546.

Torres-Oviedo, G. and Ting, L.H. 2007. Muscle synergies characterizing human postural responses. *Journal of Neurophysiology*.

Tresch, M.C. and Bizzi, E. 1999. Responses to spinal microstimulation in the chronically spinalized rat and their relationship to spinal systems activated by low threshold cutaneous stimulation. *Experimental brain research*. **129**(3), pp.401–416.

Tresch, M.C. and Cheung, V.C.K. 2006. Matrix Factorization Algorithms for the Identification of Muscle Synergies : Evaluation on Simulated and Experimental Data Sets Matrix Factorization Algorithms for the Identification of Muscle Synergies : Evaluation on Simulated and Experimental Data Sets. *Journal of Neurophysiology*. **95**(January 2006), pp.2199–2212.

Tresch, M.C., Cheung, V.C.K. and d'Avella, A. 2006. Matrix Factorization Algorithms for the Identification of Muscle Synergies: Evaluation on Simulated and Experimental Data Sets. *Journal of Neurophysiology*. **95**(4), pp.2199–2212.

Tresch, M.C., Saltiel, P., d'Avella, A. and Bizzi, E. 2002. Coordination and localization in spinal motor systems. *Brain research. Brain research reviews*. **40**(1–3), pp.66–79.

Valero-Cuevas, F.J., Venkadesan, M. and Todorov, E. 2009. Structured variability of muscle activations supports the minimal intervention principle of motor control. *Journal of Neurophysiology*.

Valk, T.A., Mouton, L.J., Otten, E. and Bongers, R.M. 2019. Fixed muscle synergies and their potential to improve the intuitive control of myoelectric assistive technology for upper extremities. *Journal of NeuroEngineering and Rehabilitation*.

Vidal, J.J. 1977. Real-time detection of brain events in EEG. *Proceedings of the IEEE*. **65**(5), pp.633–641.

Vidal, J.J. 1973. Towards Direct Brain Computer Communication. *Annual review of biophysics and bioengineering*. **2**.

Vromans, M. and Faghri, P.D. 2018. Functional electrical stimulation-induced muscular fatigue: Effect of fiber composition and stimulation frequency on rate of fatigue development. *Journal of Electromyography and Kinesiology*.

Wilson, H.R. and Cowan, J.D. 1972. Excitatory and Inhibitory Interactions in Localized Populations of Model Neurons. *Biophysical Journal*.

Wojtara, T., Alnajjar, F., Shimoda, S. and Kimura, H. 2014. Muscle synergy stability and human balance maintenance. *Journal of NeuroEngineering and Rehabilitation*.

Yang, Q., Logan, D. and Giszter, S.F. 2019. Motor primitives are determined in early development and are then robustly conserved into adulthood. *Proceedings of the National Academy of Sciences of the United States of America*.

York, G. and Chakrabarty, S. 2019. A survey on foot drop and functional electrical stimulation. *International Journal of Intelligent Robotics and Applications*.

York, G., Osborne, H., Sriya, P., Astill, S., de Kamps, M. and Chakrabarty, S. 2019. Muscles Recruited During an Isometric Knee Extension Task is Defined by Proprioceptive Feedback. *bioRxiv*.

Zhang, X. and Zhou, P. 2012. Sample Entropy Analysis of Surface EMG for Improved Muscle Activity Onset Detection against Spurious Background Spikes. *J*

Electromyogr Kinesiol. **22**(6), pp.901–907.

Zimmermann, J.B., Seki, K. and Jackson, A. 2011. Reanimating the arm and hand with intraspinal microstimulation. *Journal of neural engineering*. **8**(5), p.054001.